Nanoscale Chemical Characterization of Polymers and Functional Surfaces

One Molecule at a Time

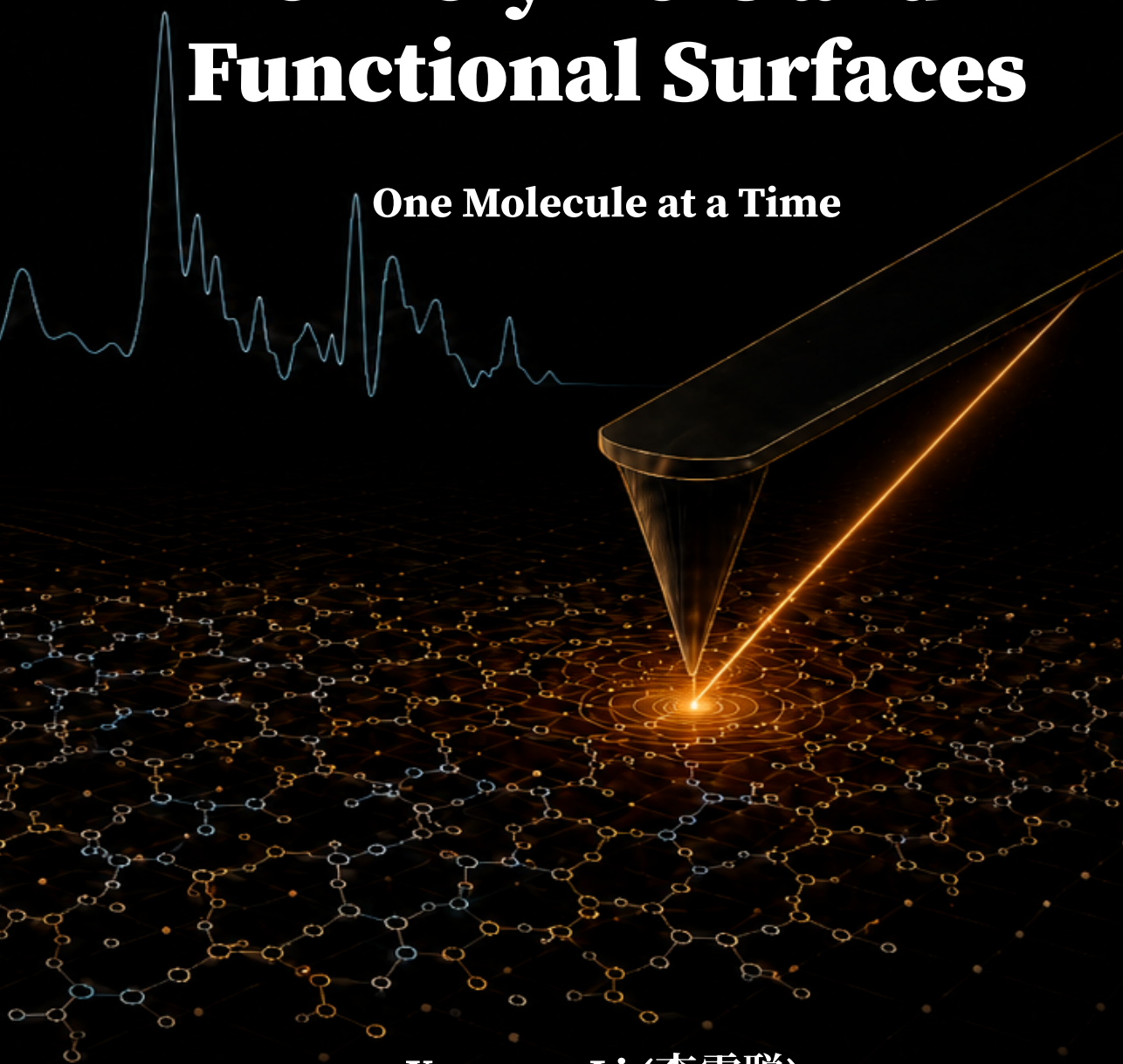

Xuecong Li (李雪聪)

Propositions

1. Local heterogeneity structures polymers and functional surfaces across different length scales. (this thesis)

2. Nanoscale chemical spectroscopy reveals how molecular interactions organize polymers and functional surfaces. (this thesis)

3. Compared with microscopy, spectroscopy is more prone to mistaking noise for signal.

4. A material property is a scale-specific description.

5. Scientific knowledge develops from material conditions.

6. Material scarcity sustains Social Darwinism.

7. War is structurally reproduced by a world divided into sovereign states.

Propositions belonging to the thesis, entitled

Nanoscale Chemical Characterization of Polymers and Functional Surfaces: One Molecule at a Time

Xuecong Li

Wageningen, 3 September, 2026

Nanoscale Chemical Characterization of Polymers and Functional Surfaces

One Molecule at a Time

Xuecong Li

李雪聪

Thesis Committee

Promotors

Prof. Dr Han Zuilhof
Professor of Organic Chemistry
Wageningen University & Research

Prof. Dr *ir.* Jasper van der Gucht
Professor of Physical Chemistry and Soft Matter
Wageningen University & Research

Co-promotor

Dr Francesco Simone Ruggeri
Associate Professor in Physical Chemistry and Soft Matter
Wageningen University & Research

Other members

Prof. Dr Johannes H. Bitter, Wageningen University & Research
Prof. Dr Jurriaan Huskens, University of Twente, Enschede
Dr Ghislaine Vantomme, Eindhoven University of Technology
Prof. Dr Ilja K. Voets, Eindhoven University of Technology

This research was conducted under the auspices of VLAG Graduate School (Biobased, Biomolecular, Chemical, Food, and Nutrition sciences).

Nanoscale Chemical Characterization of Polymers and Functional Surfaces

One Molecule at a Time

Xuecong Li

李雪聪

Thesis
submitted in fulfilment of the requirements of the degree of doctor
at Wageningen University
by the authority of the Rector Magnificus,
Prof. Dr C. Kroeze,
in the presence of the
Thesis Committee appointed by the Academic Board
to be defended in public
on Thursday 3 September 2026
at 10:30 a.m. in the Omnia Auditorium.

Xuecong Li

Nanoscale Chemical Characterization of Polymers and Functional Surfaces: One Molecule at a Time, 162 pages

PhD thesis, Wageningen University, Wageningen, the Netherlands (2026)
With references, with summary in English

DOI: 10.18174/681648

“There’s plenty of room at the bottom — but how do you know how much?”

-Dr Arden L. Bement Jr., Director, National Institute of Standards and Technology (NIST), keynote to the NEMI Road-Mapping Workshop, 2002

To who I was, and who I will become

Contents

Chapter 1	General Introduction	10
Chapter 2	Topography-Based AFM Analysis of Individual Polymer Chains for Molecular Weight Estimation	28
Chapter 3	Unravelling Emergence of Chirality in Click-Chemistry Polymers Down to the Single-Chain Level	50
Chapter 4	Nano-Chemical Analysis of Intermolecular Interactions in Self-assembled Monolayers	112
Chapter 5	General Discussion	140
Back Matter	Summary	150
	论文总结	152
	Acknowledgement	154
	About the Author	157
	List of Publications	158
	Overview of Completed Training Activities	159
	Authorship Statement	161

List of Abbreviations

ADF-STEM	annular dark-field scanning transmission electron microscopy
AFM	atomic force microscopy
AFM-IR	AFM-based photothermal infrared nanospectroscopy
ALS	autosampler
AMS AFM-IR	acoustical-mechanical suppressed AFM-IR
ATR-FTIR	attenuated total reflection Fourier transform infrared
CD	circular dichroism
CE	confidence ellipse
DAD	diode-array detector
DLS	dynamic light scattering
DOSY	diffusion-ordered spectroscopy
FFT	fast Fourier transform
FLIM	fluorescence lifetime imaging microscopy
FTIR	Fourier transform infrared
FWHM	full width at half maximum
GPC	gel permeation chromatography
HOPG	highly ordered pyrolytic graphite
HPLC	high-performance liquid chromatography
HR-MS	high-resolution mass spectrometry
IR	infrared
LB	Langmuir–Blodgett

LMS	least mean square
NMR	nuclear magnetic resonance
PCA	principal component analysis
PC1	principal component 1
PDI	polydispersity index
PLL	phase locked loop
QTOF	quadrupole time-of-flight
RID	refractive index detector
RMS	root mean square
SAM	self-assembled monolayer
SD	standard deviation
SEC	size-exclusion chromatography
SE	standard error
SNR	signal-to-noise ratio
SPIP	Scanning Probe Image Processor
SuFEx	sulfur fluoride exchange
UV-Vis	ultraviolet-visible spectroscopy
XPS	X-ray photoelectron spectroscopy

Chapter 1

General Introduction

1.1 Polymers and functional surfaces: why nanoscale characterization matters

Polymers are central to modern materials science and chemistry because they underpin a broad range of structural, interfacial, and functional systems.[1-3] Polymeric materials are widely used in coatings,[4] membranes,[5] electronic,[6] optoelectronic materials,[7] and biomedical interfaces.[8]

Functional surfaces are equally central to surface chemistry because many technologically and chemically relevant processes occur at interfaces rather than in the bulk.[4, 5, 9] Surface-confined molecular systems play key roles in molecular coatings,[10] biosensing,[11] catalysis,[12] and interfacial engineering,[2] where the structure and composition of the outermost molecular layers govern how a surface interacts with its environment.[4]

These two concepts converge in polymeric functional surfaces.[13] When polymers are placed on interfaces, they do not simply act as passive coatings, but can introduce conformational flexibility, multiple interaction sites, local heterogeneity, and cooperative organization into surface-confined systems.[14, 15] This broad interfacial versatility makes polymeric functional surfaces highly relevant in fields ranging from antifouling[16, 17] and lubrication[18] to biointerfaces,[19] controlled adhesion,[13] molecular recognition,[20] and responsive interfacial systems.[20]

However, the relevant properties of polymers, functional surfaces, and especially polymeric functional surfaces are not solely determined by their chemical identity or composition.[1, 14] Instead, their behavior is ultimately expressed through the molecular organization[21] and heterogeneity[22] across multiple length scales,[23] from molecular and repeating-unit levels to single-chains, few-chain assemblies, aggregates, and monolayers. In polymer systems, descriptors such as molecular weight, dispersity,[24] conformational organization,[25] aggregation state, and local packing[26] can strongly influence morphology,[27] intermolecular association, and resulting material behavior.[28] In functional surfaces and surface-confined molecular systems, the balance between substrate–adsorbate and adsorbate–adsorbate interactions can govern interfacial organization, molecular packing, thickness, and surface

physicochemical properties.[29] As a result, understanding these systems requires access not only to average composition, but also to local structure, local chemical environment, heterogeneity, and intermolecular interactions.[14]

A key challenge is that these properties are often governed by local chemical-structural variation distributed across hierarchical length scales, and are therefore not fully captured by bulk or ensemble-averaged methods.[15] Individual surface-supported polymer features, single chains,[30] few-chain assemblies,[31] and local monolayer domains[32] may differ substantially in morphology, organization, aggregation state, and local chemical environment from the average behavior inferred from macroscopic or bulk measurements.[30] Thus, while ensemble-averaged methods remain essential for defining overall composition and average material properties, they do not necessarily reveal how local heterogeneity gives rise to the overall behavior of polymers and functional surfaces.

For this reason, nanoscale characterization is not simply a matter of improved spatial resolution, but a necessary route to interrogate local chemical-structural variation beyond bulk averages. Methods capable of resolving local morphology together with local chemistry are therefore essential to understand how heterogeneity emerges, how hierarchical structural organization develops, and how intermolecular interactions govern polymers and functional surfaces across different length scales.

This thesis is positioned within this context and focuses on the nanoscale characterization of polymers and functional surfaces to move beyond ensemble-averaged methodology and towards a local, feature-resolved understanding of structure, chemistry, heterogeneity, hierarchical structural organization, and intermolecular interactions. It first examines how surface-supported polymer systems can be resolved as heterogeneous individual features beyond bulk-average descriptors. It then investigates how chirality emerges across molecular, single-chain, and supramolecular length scales as a form of hierarchical structural organization in polymer systems. Finally, it examines how intermolecular interactions govern the organization of self-assembled monolayers as model functional surfaces.

1.2 From ensemble averages to local heterogeneity

To characterize polymers and functional surfaces, a wide range of established analytical methods is available. Bulk and/or ensemble-averaged techniques such as gel permeation chromatography (GPC), [33] nuclear magnetic resonance (NMR) spectroscopy,[34] infrared (IR) spectroscopy,[35] ultraviolet-visible (UV-Vis) spectroscopy,[36] X-ray photoelectron spectroscopy (XPS), [37] ellipsometry,[38] contact angle analysis[39], and macroscopic thermal[40] or mechanical[41] measurements have been indispensable for defining average composition, molecular weight, chemical functionality, thickness, and global physicochemical properties of these systems.[42] These methods remain essential because they provide robust and often quantitative access to the overall characteristics of a material population or interface.

However, the key limitation of ensemble-averaged characterizations is that they report the collective response of many molecules, chains, domains, or surface sites at once.[30, 43] As a result, spatially localized variation among individual features is inherently compressed into a single output, even when that variation is structurally or functionally decisive.[44] In polymer systems, average molecular-weight descriptors and bulk spectroscopic signatures do not directly reveal how individual chains or few-chain assemblies differ in conformation, aggregation state, packing, or local chemical environment.[44] In functional surfaces, global readouts of composition, wettability, or thickness do not by themselves resolve whether the interface is molecularly homogeneous, heterogeneous, domain-structured, defect-rich, or governed by localized intermolecular interactions.[45-47]

The above mentioned limitations are especially important for surface-supported polymer systems, where the observed material is often not composed of equivalent repeating structural units, but of heterogeneous individual chains, few-chain assemblies, aggregates, and local domains that may differ substantially in morphology, organization, aggregation state, and local chemical environment, while still contributing to the same ensemble-averaged measurement.[30, 48, 49] In such systems, bulk-average characterization methods remain essential for defining overall composition and average material properties, but they do not necessarily reveal how local heterogeneity gives rise to the observed behavior of the system.[43, 44]

The central analytical requirement of this thesis is therefore not only to define average composition or average structure, but to resolve local morphology together with local chemistry from individual nanoscale features and interfacial regions.[50] This is necessary to determine how heterogeneity is distributed, how hierarchical structural organization develops, and how intermolecular interactions govern the behavior of polymers and functional surfaces across different length scales. Meeting this requirement calls for a characterization platform that can directly correlate nanoscale structure with local chemical information.[51] To address this requirement, the research described in this thesis uses atomic force microscope-based photothermal infrared nanospectroscopy (AFM-IR) as the central platform for directly correlating nanoscale structure with local chemical information.[52]

1.3 AFM-IR for direct correlation of nanoscale structure and local chemical information

For the systems addressed in this thesis, the central analytical challenge is not only to identify chemical functionality, but to determine how local chemistry is related to local morphology, organization, and intermolecular interactions within individual polymer features and surface-confined molecular regions. This is particularly important when the relevant structural units are not bulk phases, but single polymer chains, few-chain assemblies, aggregates, local domains, or confined interfacial regions with different organization and chemical environment. AFM-IR is used in this thesis because it provides localized infrared-based chemical information together with nanoscale-resolved morphology from the same region of the sample, thereby enabling direct correlation between local chemistry and local morphology.[53, 54]

Figure 1.1 illustrates the working principle of AFM-IR. In **Figure 1.1a** a tunable pulsed IR laser irradiates the sample region beneath the AFM tip, while the tip remains in contact with the sample surface. When the wavenumber of the laser is tuned to match the frequency of a vibrational mode of the sample molecules, a portion of the IR energy is absorbed and excites the molecular vibrational mode, as shown in **Figure 1.1b**.[55] When the vibrational mode returns to the ground state, the absorbed energy is dissipated as heat (**Figure 1.1c**).[56] The heat then results in a thermal expansion of the sample (**Figure 1.1d**), which increases the interaction

between the AFM tip and the sample and transduces a force on the cantilever, thereby exciting the cantilever oscillation (**Figure 1.1e**).[55] The position-sensitive photodiode (PSPD) is illuminated by the AFM laser reflected from the back of the cantilever and records the cantilever deflection as a function of time (**Figure 1.1f**).

As shown in **Figure 1.1g**, the computer extracts the amplitudes and frequencies of the cantilever oscillation by fast Fourier transform (FFT), and the oscillation amplitude at the contact resonance is used as the AFM-IR signal.[57] By recording this response as a function of the wavenumber of the IR laser, a localized IR absorption spectrum can be obtained from the nanoscale region underneath the tip, as illustrated in **Figure 1.1h**.[57] Alternatively, when the laser is fixed at a selected wavenumber corresponding to a specific vibrational mode, the same principle can be used to generate a chemically selective absorption map.[54] In this way, AFM-IR provides localized infrared-based chemical information together with nanoscale-resolved morphology from the same region of the sample.

In this thesis, AFM-IR is used as the key instrument for nanoscale chemical characterization of polymers and functional surfaces. In this way, it provides the analytical basis for relating local chemical information to morphology, organization, and intermolecular interactions across the systems examined in this thesis. This capability is central to the work presented here because it enables polymers and functional surfaces to be examined beyond bulk-average characterization methods, with particular emphasis on relating local chemistry to single-feature structure, supramolecular organization, and intermolecular interactions in the systems investigated in the following chapters.

1.4 Scope and organization of this thesis

This thesis is structured around three connected research objectives concerning the nanoscale characterization of polymers and functional surfaces. Its central scope is to investigate how local heterogeneity, hierarchical structural organization, and intermolecular interactions can be resolved beyond bulk-average characterization methods by directly correlating local morphology with local chemical information. The following sections define the aim and scope of the thesis and outline the organization of the chapters.

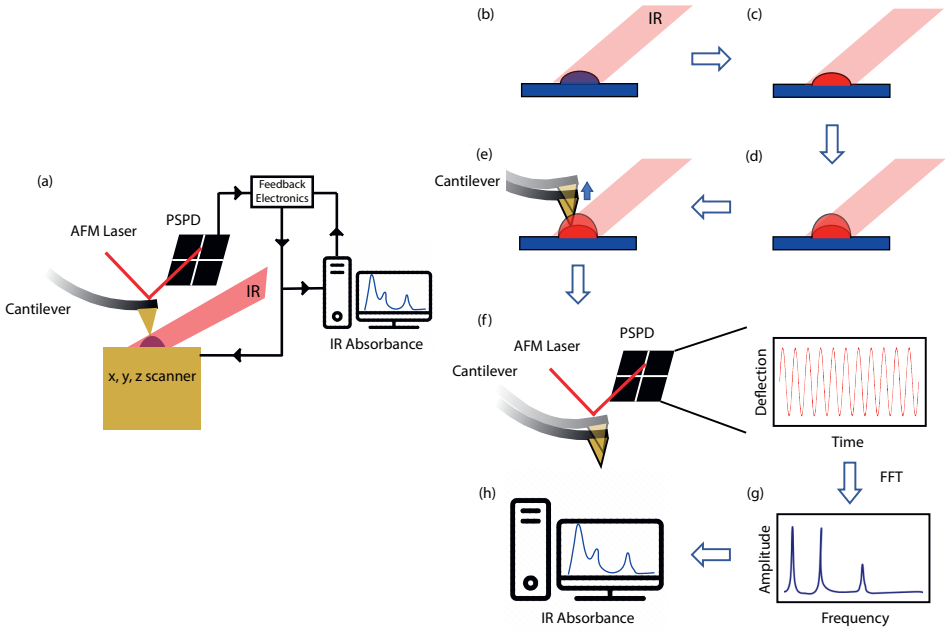

Figure 1.1. Working principle of AFM-IR. (a) Schematic illustration of AFM-IR setup. (b) Sample absorbs IR light. (c) Energy from IR absorption dissipates as heat. (d) Sample undergoes thermal expansion. (e) Thermal expansion transduces a force on the AFM tip and excites the cantilever. (f) PSPD records the deflection of the excited cantilever as a function of time. (g) Computer-based fast Fourier analysis extracts the amplitudes and frequency of the cantilever oscillation. (h) Computer records the amplitude as a function of the wavenumber of IR laser and generates the IR absorption spectrum.

1.4.1 Aim and scope of the thesis

The overall aim of this thesis is to develop and apply nanoscale characterization methodologies, with particular emphasis on AFM-IR, that integrate local morphological and chemical analysis to investigate polymers and functional surfaces beyond ensemble-averaged descriptions, by resolving nanoscale structure, chemistry, heterogeneity, and intermolecular interactions across different length scales.

This aim is addressed through three connected objectives that together define the internal logic of this thesis. The first is to extend the analysis of polymers beyond ensemble-averaged descriptions toward feature-resolved heterogeneity and physical quantification in surface-supported polymer systems at the nanoscale. The second is to determine how local heterogeneity develops into hierarchical structural organization across molecular, single-

chain, and supramolecular length scales in chiral polymer systems. The third is to reveal how intermolecular interactions govern monolayer organization in self-assembled monolayers as model functional surfaces. Together, these three objectives connect local heterogeneity, hierarchical structural organization, and intermolecular interactions as the central analytical and conceptual outcomes of this thesis.

1.4.2 Feature-resolved heterogeneity and molecular-weight-related analysis of surface-supported polymers

Chapter 2 addresses the first objective of this thesis: how nanoscale characterization can extend the analysis of polymers beyond ensemble-averaged descriptions toward feature-resolved heterogeneity and physical quantification. To do so, the chapter develops an AFM-based methodology for estimating mass-related and molecular-weight-related characteristics from nanoscale topographical information in surface-supported polymer systems. Individual polymer features are identified and analyzed as discrete units rather than only as part of an averaged population, and the resulting feature-resolved estimates are benchmarked against conventional GPC measurements in order to examine to what extent molecular-mass-related information, conventionally obtained from bulk-average characterization methods, can also be approached on a feature-resolved basis.

1.4.3 Hierarchical emergence of chirality across molecular, single-chain, and supramolecular length scales

Chapter 3 addresses the second objective of this thesis: how nanoscale characterization can resolve the hierarchical emergence of structure and chirality in polymers across the length scales of small molecules, single chains, and supramolecular assemblies. To do so, the chapter describes polymer systems in which chirality is expressed not only at the molecular level, but also through higher levels of structural organization. By relating localized structural organization to the emergence of chiral order in individual polymer features and assembled polymer systems, the chapter investigates how chirality develops from small molecules to single chains and further to supramolecular assemblies, and how this hierarchical structural development contributes to the observed

chiral organization of the polymer system.

1.4.4 Nano-chemical analysis of intermolecular interactions in self-assembled monolayers

Chapter 4 addresses the third objective of this thesis: how nanoscale chemical characterization can reveal the intermolecular interactions that govern the organization of self-assembled monolayers and related functional surfaces. To do so, the chapter combines nanoscale morphological analysis with AFM-IR-based chemical characterization to examine self-assembled monolayers as model functional surfaces. Local spectral signatures are analyzed together with monolayer structure and packing in order to determine how substrate–adsorbate and adsorbate–adsorbate interactions contribute to interfacial organization and resulting surface behavior, thereby providing direct nano-chemical insight into the molecular basis of organization in self-assembled monolayers and related functional surfaces.

Taken together, this thesis uses nanoscale characterization to relate local chemical information and nanoscale morphology to polymer organization, chiral structural development, and (inter-)molecular interactions. By doing so, the thesis moves the analysis of polymers and functional surfaces beyond bulk-average characterization methods toward direct examination of local structure, chemical composition, and intermolecular interactions. Thereby the work described in this thesis establishes nanoscale chemical characterization as a key analytical route for understanding how single-feature-level heterogeneity and hierarchical structural organization give rise to the behavior and properties of polymers and functional surfaces.

1.5 References

(1) Lutz, J.-F.; Lehn, J.-M.; Meijer, E. W.; Matyjaszewski, K. From precision polymers to complex materials and systems. *Nat. Rev. Mater.* **2016**, *1* (5), 16024. DOI: 10.1038/natrevmats.2016.24.

(2) Zoppe, J. O.; Ataman, N. C.; Mocny, P.; Wang, J.; Moraes, J.; Klok, H.-A. Surface-initiated controlled radical polymerization: state-of-the-art, opportunities, and challenges in surface and interface engineering with polymer brushes. *Chem. Rev.* **2017**, *117* (3), 1105–1318. DOI: 10.1021/acs.chemrev.6b00314.

(3) Stuart, M. A. C.; Huck, W. T. S.; Genzer, J.; Müller, M.; Ober, C.; Stamm, M.; Sukhorukov, G. B.; Szleifer, I.; Tsukruk, V. V.; Urban, M.; et al. Emerging applications of stimuli-responsive polymer Mater.. *Nat. Mater.* **2010**, *9* (2), 101–113. DOI: 10.1038/nmat2614.

(4) Hetemi, D.; Pinson, J. Surface functionalisation of polymers. *Chem. Soc. Rev.* **2017**, *46* (19), 5701–5713, 10.1039/C7CS00150A. DOI: 10.1039/C7CS00150A.

(5) Ma, Z.-Y.; Xue, Y.-R.; Yang, H.-C.; Wu, J.; Xu, Z.-K. Surface and interface engineering of polymer membranes: where we are and where to go. *Macromolecules* **2022**, *55* (9), 3363–3383. DOI: 10.1021/acs.macromol.1c02647.

(6) Sun, H.-S.; Chiu, Y.-C.; Chen, W.-C. Renewable polymeric materials for electronic applications. *Polym. J.* **2017**, *49* (1), 61–73. DOI: 10.1038/pj.2016.95.

(7) Ostroverkhova, O. Organic Optoelectronic Mater.: Mechanisms and Applications. *Chem. Rev.* **2016**, *116* (22), 13279–13412. DOI: 10.1021/acs.chemrev.6b00127.

(8) Pearce, A. K.; O'Reilly, R. K. Polymers for Biomedical Applications: The importance of hydrophobicity in directing biological interactions and application efficacy. *Biomacromolecules* **2021**, *22* (11), 4459–4469. DOI: 10.1021/acs.biomac.1c00434.

(9) Zhou, X.; Shen, Q.; Wang, Y.; Dai, Y.; Chen, Y.; Wu, K. Surface and interfacial

sciences for future technologies. *Nat. Sci. Rev.* **2024**, *11* (9). DOI: 10.1093/nsr/nwae272.

(10) Wang, W.; Mattoussi, H. Engineering the bio–nano interface using a multifunctional coordinating polymer coating. *Acc. Chem. Res.* **2020**, *53* (6), 1124–1138. DOI: 10.1021/acs.accounts.9b00641.

(11) Turner, A. P. F. Biosensors: sense and sensibility. *Chem. Soc. Rev.* **2013**, *42* (8), 3184–3196, 10.1039/C3CS35528D. DOI: 10.1039/C3CS35528D.

(12) Shifrina, Z. B.; Matveeva, V. G.; Bronstein, L. M. Role of polymer structures in catalysis by transition metal and metal oxide nanoparticle composites. *Chem. Rev.* **2020**, *120* (2), 1350–1396. DOI: 10.1021/acs.chemrev.9b00137.

(13) Fang, Y.; Yang, X.; Lin, Y.; Shi, J.; Prominski, A.; Clayton, C.; Ostroff, E.; Tian, B. Dissecting biological and synthetic soft–hard interf. for tissue-like systems. *Chem. Rev.* **2022**, *122* (5), 5233–5276. DOI: 10.1021/acs.chemrev.1c00365.

(14) Roth, C. B. Polymers under nanoconfinement: where are we now in understanding local property changes? *Chem. Soc. Rev.* **2021**, *50* (14), 8050–8066, 10.1039/D1CS00054C. DOI: 10.1039/D1CS00054C.

(15) Rest, C.; Kandanelli, R.; Fernández, G. Strategies to create hierarchical self-assembled structures via cooperative non-covalent interactions. *Chem. Soc. Rev.* **2015**, *44* (8), 2543–2572, 10.1039/C4CS00497C. DOI: 10.1039/C4CS00497C.

(16) Postma, E. J.; Scheres, L.; de Beer, S.; Kuzmyn, A. R.; Zuilhof, H. Functionalized antifouling polymer brushes for biospecific surfaces. *Adv. Mater. Interf.* **2025**, *12* (14), 2400955. DOI: 10.1002/admi.202400955.

(17) Laftah, W. A.; Wan Abdul Rahman, W. A. Polymers for anti-fouling applications: a Rev.. *Env. Sci. Adv.* **2025**, *4* (6), 824–841, 10.1039/D5VA00034C. DOI: 10.1039/D5VA00034C.

(18) Long, Z.; Meng, J.; Weddle, L. R.; Videla, P. E.; Menzel, J. P.; Cabral, D. G. A.; Liu, J.; Qiu, T.; Palasz, J. M.; Bhattacharyya, D.; et al. The impact of electric fields

on processes at electrode interface. *Chem. Rev.* **2025**, *125* (3), 1604–1628. DOI: 10.1021/acs.chemrev.4c00487.

(19) Park, Y.; Chung, T. S.; Lee, G.; Rogers, J. A. Material chemistry of neural interface technologies and recent advances in three-dimensional systems. *Chem. Rev.* **2022**, *122* (5), 5277–5316. DOI: 10.1021/acs.chemrev.1c00639.

(20) Browne, W. R.; Feringa, B. L. Light switching of molecules on surfaces. *Annu. Rev. Phys. Chem.* **2009**, *60* (Volume 60, 2009), 407–428. DOI: 10.1146/annurev.physchem.040808.090423.

(21) Khasbaatar, A.; Xu, Z.; Lee, J.-H.; Campillo-Alvarado, G.; Hwang, C.; Onusaitis, B. N.; Diao, Y. From solution to thin film: molecular assembly of π-conjugated systems and impact on (opto)electronic properties. *Chem. Rev.* **2023**, *123* (13), 8395–8487. DOI: 10.1021/acs.chemrev.2c00905.

(22) Danielsen, S. P. O.; Beech, H. K.; Wang, S.; El-Zaatari, B. M.; Wang, X.; Sapir, L.; Ouchi, T.; Wang, Z.; Johnson, P. N.; Hu, Y.; et al. Molecular characterization of polymer networks. *Chem. Rev.* **2021**, *121* (8), 5042–5092. DOI: 10.1021/acs.chemrev.0c01304.

(23) Shao, L.; Ma, J.; Prelesnik, J. L.; Zhou, Y.; Nguyen, M.; Zhao, M.; Jenekhe, S. A.; Kalinin, S. V.; Ferguson, A. L.; Pfaendtner, J.; et al. Hierarchical material from high information content macromolecular building blocks: construction, dynamic interventions, and prediction. *Chem. Rev.* **2022**, *122* (24), 17397–17478. DOI: 10.1021/acs.chemrev.2c00220.

(24) Liu, K.; Corrigan, N.; Postma, A.; Moad, G.; Boyer, C. A comprehensive platform for the design and synthesis of polymer molecular weight distributions. *Macromolecules* **2020**, *53* (20), 8867–8882. DOI: 10.1021/acs.macromol.0c01954.

(25) Wang, Z.-G. 50th anniversary perspective: polymer conformation—a pedagogical review. *Macromolecules* **2017**, *50* (23), 9073–9114. DOI: 10.1021/acs.macromol.7b01518.

(26) Yadav, H. O. S.; Kuo, A.-T.; Urata, S.; Shinoda, W. Effect of the packing density on the surface hydrophobicity of ω-functionalized (−CF3, −CH3, −OCH3, and −

OH) self-assembled monolayers: a molecular dynamics study. *J. Phys. Chem. C* **2020**, *124* (26), 14237–14244. DOI: 10.1021/acs.jpcc.0c03485.

(27) Liu, R.; Yang, W.; Xu, W.; Deng, J.; Ding, C.; Guo, Y.; Zheng, L.; Sun, J.; Li, M. Impact of chemical design on the molecular orientation of conjugated donor–acceptor polymers for field-effect transistors. *ACS Appl. Polym. Mater.* **2022**, *4* (4), 2233–2250. DOI: 10.1021/acsapm.1c01676.

(28) Huang, H.; Yang, L.; Facchetti, A.; Marks, T. J. Organic and polymeric semiconductors enhanced by noncovalent conformational locks. *Chem. Rev.* **2017**, *117* (15), 10291–10318. DOI: 10.1021/acs.chemrev.7b00084.

(29) Celik, U.; Lee, H. J.; Keel, T.; Swartz, L. A.; Van Zijll, M.; Chalker, C. J.; Lee, T. R.; Liu, G.-y. Molecular level structural characterization of self-assembled monolayers of functionalized bidentate aromatic thiols. *J. Phys. Chem. C* **2021**, *125* (43), 24162–24169. DOI: 10.1021/acs.jpcc.1c07171.

(30) Mai, D. J.; Schroeder, C. M. 100th anniversary of macromolecular science viewpoint: single-molecule studies of synthetic polymers. *ACS Macro Let.* **2020**, *9* (9), 1332–1341. DOI: 10.1021/acsmacrolett.0c00523.

(31) Cucinotta, A.; Davies, J. A.; Mali, K. S.; De Feyter, S. Scanning probe microscopy of metal–organic coordination systems: characterization of monolayers, single crystals, discrete architectures. *Chem. Soc. Rev.* **2025**, *54* (22), 10654–10689, 10.1039/D4CS01303D. DOI: 10.1039/D4CS01303D.

(32) Scheffold, F. Pathways and challenges towards a complete characterization of microgels. *Nat. Commun.* **2020**, *11* (1), 4315. DOI: 10.1038/s41467-020-17774-5.

(33) Matson, J. B.; Steele, A. Q.; Mase, J. D.; Schulz, M. D. Polymer characterization by size-exclusion chromatography with multi-angle light scattering (SEC-MALS): a tutorial review. *Polym. Chem.* **2024**, *15* (3), 127–142, 10.1039/D3PY01181J. DOI: 10.1039/D3PY01181J.

(34) Spiess, H. W. Structure and dynamics of solid polymers from 2D- and 3D-NMR. *Chem. Rev.* **1991**, *91* (7), 1321–1338. DOI: 10.1021/cr00007a002.

(35) Mangolini, F.; Rossi, A. 4. Attenuated total reflection-Fourier transform infrared spectroscopy: A powerful tool for investigating polymer surfaces and interface. In *Polymer Surface Characterization*, Luigia, S. Ed.; De Gruyter, 2014; pp 113–152.

(36) Begum, R.; Farooqi, Z. H.; Naseem, K.; Ali, F.; Batool, M.; Xiao, J.; Irfan, A. applications of uv/vis spectroscopy in characterization and catalytic activity of noble metal nanoparticles fabricated in responsive polymer microgels: a review. *Crit. Rev. Anal. Chem.* **2018**, *48* (6), 503–516. DOI: 10.1080/10408347.2018.1451299.

(37) Giglio, E. D.; Ditaranto, N.; Sabbatini, L. 3. Polymer surface chemistry: characterization by XPS. In *Polymer Surface Characterization*, Luigia, S. Ed.; De Gruyter, 2014; pp 73–112.

(38) Bittrich, E.; Eichhorn, K.-J. 8. Advances of spectroscopic ellipsometry in the analysis of thin polymer films-polymer interface. In *Polymer Surface Characterization*, Luigia, S. Ed.; De Gruyter, 2014; pp 247–286.

(39) Palumbo, F.; Mundo, R. D. 7. Wettability: Significance and measurement. In *Polymer Surface Characterization*, Luigia, S. Ed.; De Gruyter, 2014; pp 207–246.

(40) Koch, A.; Aro, R.; Wang, T.; Yeung, L. W. Y. Towards a comprehensive analytical workflow for the chemical characterisation of organofluorine in consumer products and environmental samples. *TrAC Trend. Anal. Chem.* **2020**, *123*, 115423. DOI: 10.1016/j.trac.2019.02.024.

(41) Jones, D. S. Dynamic mechanical analysis of polymeric systems of pharmaceutical and biomedical significance. *Int. J. Pharm.* **1999**, *179* (2), 167–178. DOI: 10.1016/S0378-5173(98)00337-8.

(42) Topham, P. D.; Boucher, R. J.; Chang, T.; Smrčková, M. D.; Farrell, W. S.; He, J.; Hess, M.; Hu, W.; Hutchins-Crawford, H. J.; Keddie, D. J.; et al. A brief guide to polymer characterization: structure (IUPAC Technical Report). *Pure Appl. Chem.* **2023**, *95* (10), 1121–1126. DOI: doi:10.1515/pac-2022-0602.

(43) Hemmer, J. V.; Joshi, P. B.; Kaur, A.; Wilson, A. J. Reducing ensemble averaging for mechanistic understanding of electrocatalysis in energy conversion

reactions. *J. Phys. Chem. C* **2024**, *128* (2), 697–709. DOI: 10.1021/acs.jpcc.3c06615.

(44) Vacha, M.; Habuchi, S. Conformation and physics of polymer chains: a single-molecule perspective. *NPG Asia Mater.* **2010**, *2* (4), 134–142. DOI: 10.1038/asiaMater.2010.135.

(45) Badia, A.; Lennox, R. B.; Reven, L. A dynamic view of self-assembled monolayers. *Acc. Chem. Res.* **2000**, *33* (7), 475–481. DOI: 10.1021/ar9702841.

(46) Gannon, G.; Greer, J. C.; Larsson, J. A.; Thompson, D. Molecular dynamics study of naturally occurring defects in self-assembled monolayer formation. *ACS Nano* **2010**, *4* (2), 921–932. DOI: 10.1021/nn901821h.

(47) Kung, C. H.; Sow, P. K.; Zahiri, B.; Mérida, W. Assessment and interpretation of surface wettability based on sessile droplet contact angle measurement: challenges and opportunities. *Adv. Mater. Interf.* **2019**, *6* (18), 1900839. DOI: 10.1002/admi.201900839.

(48) Korolkov, V. V.; Summerfield, A.; Murphy, A.; Amabilino, D. B.; Watanabe, K.; Taniguchi, T.; Beton, P. H. Ultra-high resolution imaging of thin films and single strands of polythiophene using atomic force microscopy. *Nat. Commun.* **2019**, *10* (1), 1537. DOI: 10.1038/s41467-019-09571-6.

(49) Murphy, J. G.; Raybin, J. G.; Sibener, S. J. Correlating polymer structure, dynamics, and function with atomic force microscopy. *J. Polym. Sci.* **2022**, *60* (7), 1042–1058. DOI: 10.1002/pol.20210321.

(50) Kurouski, D.; Dazzi, A.; Zenobi, R.; Centrone, A. Infrared and Raman chemical imaging and spectroscopy at the nanoscale. *Chem. Soc. Rev.* **2020**, *49* (11), 3315–3347. DOI: 10.1039/c8cs00916c.

(51) V. D. dos Santos, A. C.; Hondl, N.; Ramos-Garcia, V.; Kuligowski, J.; Lendl, B.; Ramer, G. AFM-IR for nanoscale chemical characterization in life sciences: recent developments and future directions. *ACS Meas. Sci. Au* **2023**, *3* (5), 301–314. DOI: 10.1021/acsmeasuresciau.3c00010.

(52) Li, X.; Pujari, S. P.; van der Gucht, J.; Zuilhof, H.; Ruggeri, F. S. Unravelling emergence of chirality in click-chemistry polymers down to the single-chain level. *Nat. Commun.* **2025**, *16* (1), 6761. DOI: 10.1038/s41467-025-62041-0.

(53) Ruggeri, F. S.; Habchi, J.; Chia, S.; Horne, R. I.; Vendruscolo, M.; Knowles, T. P. J. Infrared nanospectroscopy reveals the molecular interaction fingerprint of an aggregation inhibitor with single Aβ42 oligomers. *Nat. Commun.* **2021**, *12* (1), 688. DOI: 10.1038/s41467-020-20782-0.

(54) Ruggeri, F. S.; Mannini, B.; Schmid, R.; Vendruscolo, M.; Knowles, T. P. J. Single molecule secondary structure determination of proteins through infrared absorption nanospectroscopy. *Nat. Commun.* **2020**, *11* (1), 2945. DOI: 10.1038/s41467-020-16728-1.

(55) Mathurin, J.; Deniset-Besseau, A.; Bazin, D.; Dartois, E.; Wagner, M.; Dazzi, A. Photothermal AFM-IR spectroscopy and imaging: Status, challenges, and trends. *J. Appl. Physics* **2022**, *131* (1). DOI: 10.1063/5.0063902.

(56) Kurouski, D.; Dazzi, A.; Zenobi, R.; Centrone, A. Infrared and Raman chemical imaging and spectroscopy at the nanoscale. *Chem. Soc. Rev.* **2020**, *49* (11), 3315–3347, 10.1039/C8CS00916C. DOI: 10.1039/C8CS00916C.

(57) Dazzi, A.; Prater, C. B.; Hu, Q.; Chase, D. B.; Rabolt, J. F.; Marcott, C. AFM–IR: combining atomic force microscopy and infrared spectroscopy for nanoscale chemical characterization. *Appl. Spectrosc.* **2012**, *66* (12), 1365–1384. DOI: 10.1366/12-06804.

1

Chapter 2

Topography-based AFM Analysis of Individual Polymer Chains for Molecular Weight Estimation

This chapter is adapted from: Asadi, V.; **Li, Xuecong**; Ruggeri, F. S.; Zuilhof, H.; van der Gucht, J.; Kodger, T. E. Synthesis of well-defined linear–bottlebrush–linear triblock copolymer towards architecturally-tunable soft materials. *Polymer Chemistry* **2022**, *13* (32), 4666–4674, DOI: 10.1039/D2PY00841F. and **Li, Xuecong**; Pujari, S. P.; Gucht, J. V.; Zuilhof, H.; Ruggeri, F. S. AFM-Based Estimation of Single Polymer Chains Molecular Weight. *in preparation*

ABSTRACT

Polymer molecular weight and dispersity are conventionally defined by bulk measurements, which provide highly valuable sample-level descriptors but do not assign molecular-weight related information to individual surface-supported polymer features or preserve feature-to-feature heterogeneity. Such bulk measurements cannot determine their aggregation status. In this chapter, we use AFM to first directly resolve individual polymer features and provide quantitative topographic readout in a bottlebrush polymer system, establishing access to polymer dimensions at the level of individual features. Building on this topographic access, we establish an atomic force microscopy (AFM)-based methodology for single feature-resolved molecular-weight estimation from AFM topography. The workflow combines deconvoluted feature area, measured feature height, density-based conversion, and explicit uncertainty treatment to estimate the molecular weight of individual detected features. Applied to three SuFEx polymer samples differing in molecular weight, the AFM-derived output estimated the molecular weight of individual detected features within each nominal sample, thereby yielding feature-resolved molecular-weight distributions rather than one bulk-like value. Partitioning of these distributions revealed low, intermediate, and high molecular weight regimes, and representative AFM features showed that these regimes are physically interpretable in terms of single-chain-like and aggregate-like objects. Together, these results establish single feature-resolved AFM characterization as a route to quantify polymer topography, and from this estimate the molecular weight of individual polymeric chains, assess heterogeneity within polymer samples, and differentiate feature populations according to aggregate state beyond bulk-average readouts.

2.1 Introduction

Molecular weight and molecular weight distribution are fundamental descriptors of polymers because they directly influence shapes, polymer structures, properties, processability, and, ultimately, materials performance.[1-3] Reliable molecular weight analysis is therefore central not only to polymer synthesis and characterization, but also for the controlled design of polymer and material properties.

Routinely, polymer molecular weight and distribution are analyzed mainly by bulk solution methods. Size-exclusion chromatography (SEC)[4] remains the most widely used method for determining molecular weight distributions, while dynamic light scattering (DLS)[5] is a common complementary method for probing hydrodynamic size in solution. Under suitable conditions, static light scattering (SLS) can further provide weight-average molar mass and radius of gyration.[5] Nuclear magnetic resonance (NMR)-based approaches can also provide molecular weight information, for example through end-group analysis or diffusion-based calibration strategies, such as diffusion-ordered spectroscopy (DOSY).[6, 7] These methods are highly valuable for defining sample-level descriptors, including averaged molecular weight and distribution. However, they do not directly assign information related to molecular weight to individual surface-supported polymer features. In particular, SEC and DLS measure hydrodynamic sizes and are therefore sensitive to calibration strategies, the polymer architecture, and polymer–solvent interactions.[4] NMR-based end-group analysis requires identifiable terminal signals, while DOSY-based approaches rely on calibrated diffusion–molecular-weight relationships rather than direct mass measurement.[6] Thus, current molecular-weight analysis is highly effective at the bulk level, but it does not directly assign molecular-weight related information to individual polymeric features. This limitation becomes particularly important in surface-confined polymer systems like functional surfaces, where polymer organization is heterogeneous and includes individual chains, few-chain assemblies, and larger features that differ in size, morphology, and aggregation state. In such cases, bulk methods report molecular weight only as an average over these different feature populations, rather than resolving molecular-weight-related variation at the level of individual features.

Several nanoscale microscopy-based strategies have recently emerged for polymer molecular weight analysis. Annular dark-field scanning transmission electron microscopy (ADF-STEM) enables precision molecular-weight analysis by

detecting and counting metal(loid) atoms incorporated into polymer structures.[8] Fluorescence lifetime imaging microscopy (FLIM) enables rapid molecular-weight determination of growing polymers without removing them from the reaction mixture.[9] However, FLIM remains a liquid-phase measurement and requires fluorescent labeling, while ADF-STEM relies on built-in or introduced high-Z identifiers for atomic counting.[8, 9] By contrast, AFM offers direct topographic information on polymer features without labeling.[10, 11] An early study combined the Langmuir–Blodgett technique[12] with AFM-based molecular counting to determine the absolute molecular-weight distribution of cylindrical brush molecules, establishing a quantitative AFM route based on monolayer mass density and molecular density analysis.[13] However, this approach remains nanoscale area-averaged rather than feature-resolved. It therefore does not directly resolve heterogeneity among individual polymer chains.

A recent study showed that AFM can access single-chain and few-chain polymer features, and reveal their heterogeneity.[14] In this chapter, the single-feature resolution capability is used to establish that polymer molecular weight can be estimated from AFM topography at the level of individual detected features. Specifically, a topographic volume-based AFM workflow is established in which feature-level topographic parameters are converted into molecular-weight estimates with explicit error evaluation. As summarized in **Figure 2.1**, this workflow differs from conventional bulk methods because it does not reduce the sample to an ensemble-averaged descriptor, from label- or identifier-dependent nanoscale methods because it does not require added contrast elements, and from earlier AFM approaches because it is feature-resolved rather than area-averaged.

2.2 Results and Discussion

2.2.1 AFM directly resolves individual polymer features and enables dimensional estimation

AFM was first applied to a linear-bottlebrush-linear triblock co-polymer system, in which the middle block is a bottle brush segment, to establish direct single-feature resolved analysis of polymer 3D shape and volume (**Figure 2.2**).[15] High-resolution and phase-controlled AFM height maps were acquired on two independent substrates, namely highly oriented pyrolytic graphite (HOPG) and

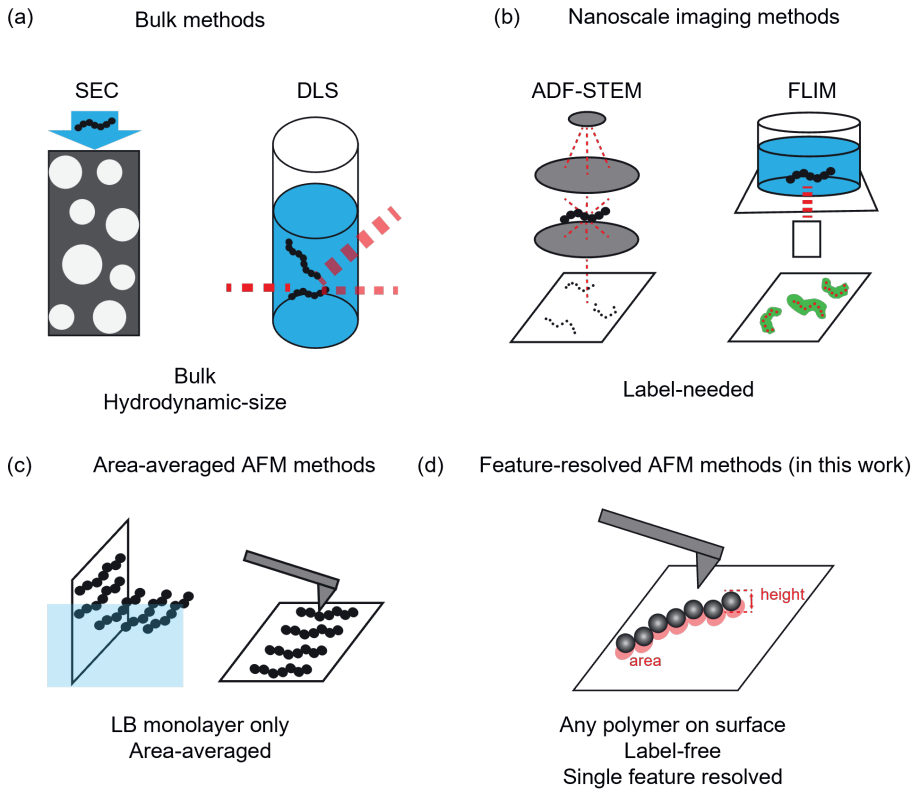

Figure 2.1. Schematic comparison of state-of-the-art polymer molecular-weight analysis methods and the presented AFM-based workflow. (a) Conventional bulk methods, provide sample level bulk, solution-state information related to hydrodynamic size, represented by Left: SEC; Right: DLS. (b) Nanoscale imaging methods, provide nanoscale information, through label- or identifier-dependent readouts, represented by Left: ADF-STEM; Right: FLIM. (c) Existing AFM area average methods provide area averaged molecular weight on LB monolayer samples based on surface density. (d) Single-molecule AFM (in this chapter) provide label-free topographic and molecular-weight-related information for individual polymer chains.

mica, as shown in **Figure 2.2a-b**. Individual bottlebrush polymer features could be directly visualized in these maps, including isolated elongated features as well as regions containing more than one deposited object. The bottlebrush middle block could be clearly observed, and the morphology of individual deposited features was directly accessible at the nanoscale. Cross-sectional analysis further showed that representative polymer features exhibited contour lengths of approximately 50–60 nm and measured heights of approximately 0.5–1 nm in **Figure 2.2c**. These measured dimensions were in good agreement with the expected dimensions (**Figure 2.2d**) based on the molecular design of the bottlebrush polymer. AFM

therefore provided not only direct visualization of individual surface-supported polymer features, but also quantitative dimensional readout at the single-feature level. In the context of this chapter, this single feature-resolved topographic access is important because it establishes that AFM can resolve and quantify discrete polymer features beyond bulk-average readouts.

AFM has been shown to resolve single-chain and few-chain polymer features and reveal their heterogeneity.[14] In this chapter, the bottlebrush-containing triblock system first establishes that AFM can resolve and quantify discrete polymer features. Building on this topographic access, the following workflow was applied to SuFEx polymer samples to estimate molecular weight at the level of individual detected features. The explicit use of measurable topographic observables also makes the associated uncertainty directly assessable, which contributes to the robustness of the method.

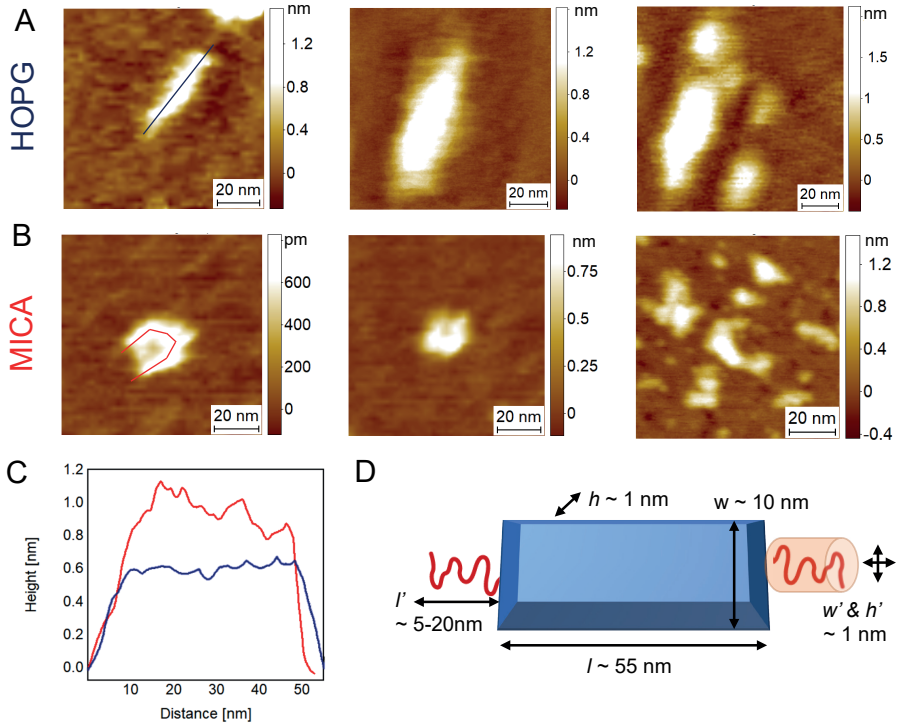

Figure 2.2. High-resolution AFM maps of linear-bottlebrush-linear triblock co-polymer (mixture of PS-b-bbPDMS and PS-b-bbPDMS-b-PS) on (a) highly ordered pyrolytic graphite (HOPG) and (b) mica. (c) Cross-sectional dimensions of some typical polymers on the surface with ca. 50–60 nm length and 0.5–1 nm height. The measured sizes well correspond with (d) the expected experimental design.

2.2.2 Workflow for AFM-based molecular weight estimation of individual SuFEx polymer features

We develop here a workflow for the molecular-weight estimation of individual SuFEx polymer chains, based on their topographic volume on high-resolution AFM maps (**Figure 2.3**). Starting from a representative AFM morphology map of the polymer sample on highly oriented pyrolytic graphite (HOPG), isolated polymer features were selected as individual analysis targets, while incomplete features at image borders and features crossing HOPG step edges were excluded from further analysis (**Figure 2.3a**). A representative selected feature is shown in zoomed form in **Figure 2.3b** after plane and line correction, providing the basis for extraction of the topographic observables used for molecular-weight estimation.

The first observable was the feature's height, h (nm). As illustrated in **Figure 2.3c**, the height was determined from two representative perpendicular line profiles across the selected feature, and defined as the average of the two measured profile heights. The second observable was the apparent area of the feature, A_{app} (nm^2). The same line-profile analysis was used to define the half-height threshold, which was then applied in threshold-based particle analysis to generate the segmented feature mask and determine A_{app} (**Figure 2.3d**). For each detected feature, the two directly measured topographic observables and were individually determined. Because A_{app} is affected by lateral broadening from tip convolution and therefore overestimates the lateral feature area,[16] the apparent area was first deconvoluted to obtain the corrected feature area,[17] A_{deconv} (nm^2):

$$A_{dconv} = \pi \left(\sqrt{\frac{A_{app}}{\pi}} - \sqrt{R_t h} \right)^2 \tag{2.1}$$

In this, R_t is the AFM tip radius. For the SSS-NCHR probe used here, the manufacturer-specified nominal tip radius is ~2 nm, which was used for the deconvolution. The feature volume V (nm^3) was then estimated considering each polymer as equivalent to a cylinder with deconvoluted area A_{deconv} (nm^2) and the measured height h (nm) according to:

$$V = A_{dconv} \times h \tag{2.2}$$

We then converted the volume into molecular weight using the density of the polymer, ρ :

$$MW \approx 0.602214 \times \rho \times V \tag{2.3}$$

where the prefactor 0.602214 is the unit conversion factor for obtaining molecular weight in kDa. In the present analysis, an estimated polymer density ρ = 1.1 g/cm^{-3} was used, consistent with reported computed mass densities of polysulfates in the range of 1.10-1.20 g/cm^{-3}.[18] The relative uncertainty in the topography-to-molecular-weight conversion, was estimated from two directly measurable sources (**Figure 2.3e**). First, by relative uncertainty in feature-height determination, ε_h,

$$\varepsilon_h = \frac{\delta h}{h} \tag{2.4}$$

where δh is the uncertainty in the measured height. Second, by the relative uncertainty introduced by the finite pixel size of the AFM image, ε_{pix} :[19]

$$\varepsilon_{pix} = \frac{2p}{\sqrt{\pi A_{dconv}}} \tag{2.5}$$

In this, p is the pixel size of the AFM image, which is 1 nm in the present measurements.

Because the molecular weight is obtained from feature volumes through a linear density-based conversion, the relative uncertainty in MW, ε_{tot}, was taken to be equal to the relative uncertainty in V, and was therefore estimated from the two directly measurable contributions defined above. To avoid underestimation, the two contributions were added directly, so that ε_{tot} represents a conservative upper-limit estimate for the propagated measurement uncertainty:

$$\varepsilon_{tot} = \varepsilon_h + \varepsilon_{pix} \tag{2.6}$$

This propagated uncertainty does not include systematic uncertainties associated with the assumed polymer density, cylinder-equivalent feature geometry, segmentation, or deconvolution. These factors may shift the absolute molecular weight estimates but do not affect the feature-by-feature application of the workflow. The measured AFM height should nevertheless be regarded as an experimentally accessible topographic readout that may be systematically underestimated.[20] This underestimation can arise because soft, subnanometre polymer features on a rigid substrate do not necessarily produce an apparent AFM height equal to their full geometric thickness, owing to tip–sample and tip–

substrate interactions, including van der Waals forces. Such underestimation would directly propagate to underestimation of volume and, consequently of the AFM-derived molecular weight. Following this workflow, for the representative feature in **Figure 2.3b**, the measured height was 0.40 ± 0.02 nm, and the deconvoluted feature area was 1336 ± 41 nm^2. These values yielded a feature volume of 524 ± 43 nm^3 and a corresponding molecular weight of 354 ± 29 kDa. This representative example shows how the molecular-weight estimate was obtained from the measured topographic observables.

Together, these steps establish a topography-based workflow for molecular-weight estimation at the level of individual detected polymer features. Because the workflow is applied to individual polymer features rather than to an ensemble-averaged signal, the same analysis can be repeated across many detected features within the sample. On this basis, the following section examines how single feature-resolved AFM analysis yields molecular-weight distributions and resolves the heterogeneity of the sample beyond bulk-average readouts.

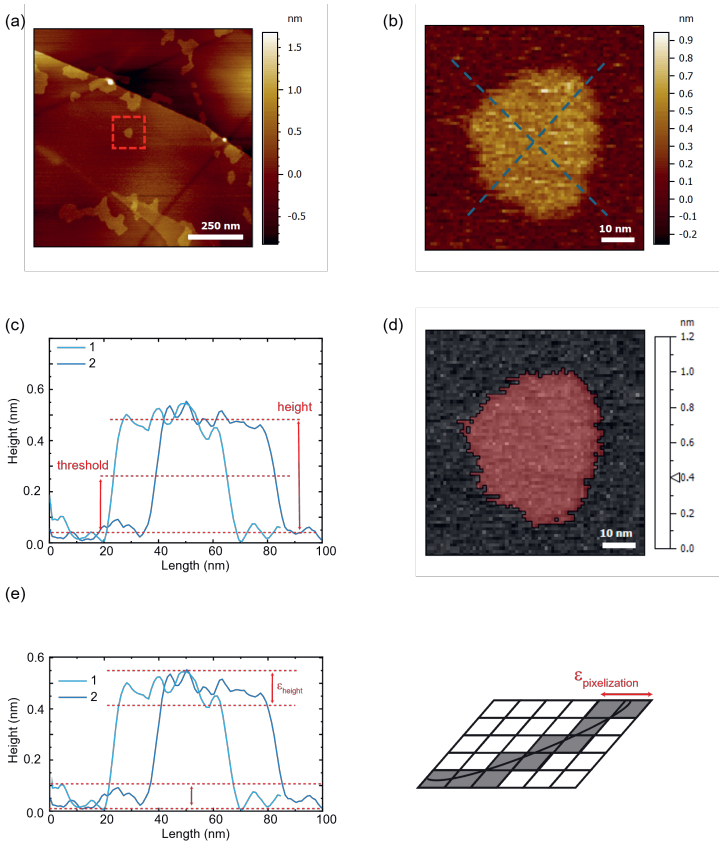

Figure 2.3. Workflow for feature-resolved molecular-weight estimation from AFM topography. (a) Representative AFM morphology map of a surface-supported polymer sample. (b) Zoomed view of the selected feature, highlighted in red box in (a). (c) Height determination and half-height threshold used for area analysis, representative height profiles highlighted by blue lines in (b). (d) Threshold-based particle analysis for determination of the apparent area. (e) Left: Error on Height; Right: Error on area by pixelization.

2.2.3 AFM-derived molecular-weight distributions and aggregate regimes

To examine whether the AFM workflow resolves single feature-level molecular-weight heterogeneity in real polymer samples, it was applied to the three SuFEx polymer samples,[21] with corresponding GPC-derived weight-average molecular weights of 209, 230, and 302 kDa, respectively (**Figure 2.4**). AFM-derived molecular-weight values obtained from these three samples are summarized in **Figure 2.4a**. For the 209 kDa sample, the AFM-derived molecular weight was 287 ± 108 kDa. For the 230 kDa sample, the corresponding value was 326 ± 165 kDa and for the 302 kDa sample, it was 454 ± 269 kDa. The mean AFM-derived molecular-weight values also showed an overall shift toward higher values from the 209 kDa sample to the 230 kDa sample and further to the 302 kDa sample, indicating that the AFM-derived output remained sensitive to molecular-weight differences across the sample set. The AFM-derived means were higher than the corresponding GPC-derived Mw values, consistent with the inclusion of aggregate-like surface-supported features in the AFM analysis. At the same time, all three samples exhibited broad feature-resolved distributions, as reflected by the substantial within-sample standard deviations, indicating molecular-weight heterogeneity at the level of individual detected features.

The broad distributions of each sample in **Figure 2.4a** required further analysis to determine whether the AFM-derived molecular-weight values within each sample were better described as one continuous feature population or as several distinguishable fractions associated with different aggregation states. To examine this, k-means clustering was applied to the AFM-derived molecular-weight values of each sample independently. This unsupervised method partitions the data into k clusters by minimizing the within-cluster sum of squares (WCSS), defined here as the sum of squared deviations between each AFM-derived molecular weight value and the center of its assigned cluster. Here, k=1 corresponds to the unpartitioned case, for which the WCSS was 2.12×10^5,

3.85×10^5, and 1.01×10^6 kDa^2 for the 209, 230, and 302 kDa samples, respectively. The effect of introducing further within-sample partitioning was then evaluated over k= 2, 3, and 4 by elbow and silhouette analysis (**Supplementary Fig. 2.1**). The elbow analysis evaluates how strongly WCSS decreases when additional clusters are introduced, whereas the silhouette score evaluates how well each data point fits within its assigned cluster relative to other clusters. For the 209 and 230 kDa samples, the elbow plots showed the largest reduction in within-cluster sums of squares when increasing from k=2 to k=3, and the silhouette analysis reached its highest value at k=3. For the 302 kDa sample, the elbow plot again showed its largest drop from k=2 to k=3, whereas the silhouette analysis reached its maximum at k=2 and remained comparable at k=3 (0.624 vs 0.607). On this basis, k=3 was retained as the most informative common partition across the three samples. The resulting within-sample cluster partitioning is shown in **Figure 2.4b**. For the 209, 230, and 302 kDa samples, the cluster centers were 153/276/451, 175/390/572, and 254/522/898 kDa, respectively, defining low-, intermediate-, and high-molecular-weight regimes within each sample rather than one uniform population. The separation between adjacent regimes remained clear at the level of mean ± 1 SD within each sample. The lowest regime centers corresponded to approximately 73%, 76%, and 84% of the respective GPC values, which is consistent with underestimation of AFM-derived volume if AFM height is underestimated, as discussed above. Within this framework, the three regimes are interpreted as resolved polymer-object populations most consistent with single-chain-like, medium-aggregate, and large-aggregate states. Representative AFM images corresponding to these regimes are shown in **Figure 2.4c**. The corresponding polymer objects exhibited feature areas of 640, 1746, and 3655 nm^2, with AFM-derived molecular-weight estimates of 169, 463, and 968 kDa. These examples show that the molecular-weight-based partitioning is physically interpretable at the level of resolved AFM objects.

Taken together, these results show that the AFM workflow yields feature-resolved molecular-weight distributions and distinguishes polymer-object populations with different aggregation states within real polymer samples.

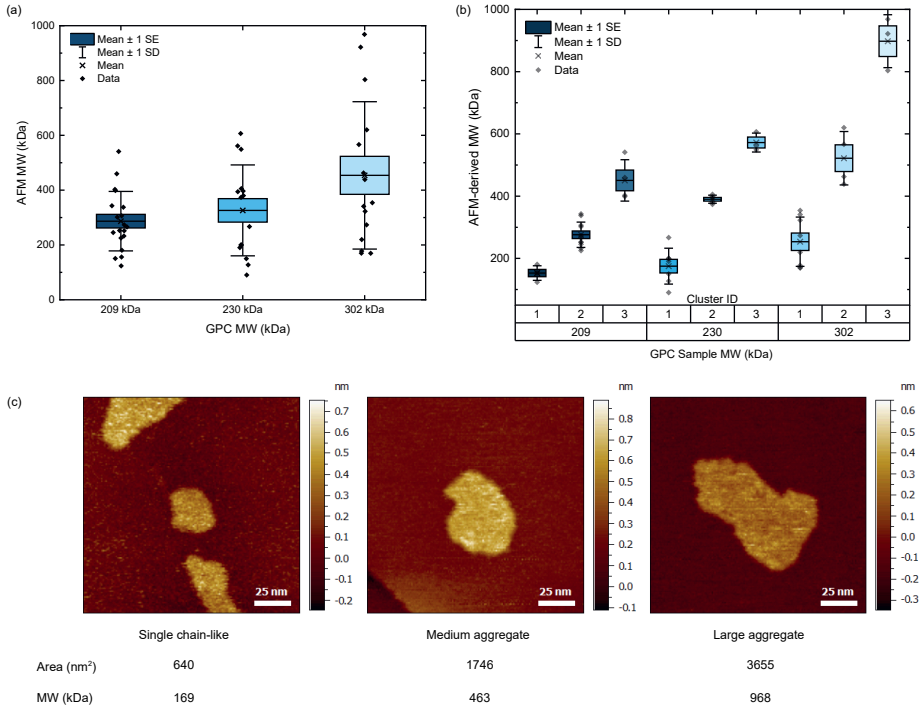

Figure 2.4. AFM-derived molecular-weight distributions and within-sample cluster partitioning. (a) AFM-derived molecular-weight distributions of the three polymer samples; box plots with overlaid individual feature values; centre line = mean; box = 1 SE; whiskers = 1 SD. (b) Sample-wise partitioning of the AFM-derived molecular-weight by k-means clustering; Cluster 1, single-chain-like regime; Cluster 2, medium aggregate regime; Cluster 3, large aggregate regime. (c) Representative AFM height maps from the three regimes identified in (b) with corresponding feature area and AFM-derived molecular-weight estimate below; left, single-chain-like feature; middle, medium aggregate; right, large aggregate.

2.3 Conclusions

This chapter establishes a topography-based AFM workflow for single-feature resolved polymer molecular-weight analysis. By combining deconvoluted feature area, measured feature height, density-based conversion, and explicit uncertainty treatment, the workflow converts AFM topography into molecular-weight estimates for individual detected features.

Applied to three SuFEx polymer samples differing only in molecular weight, the AFM-derived output followed the same overall ordering as the corresponding GPC molecular weights. A key result is that AFM resolves individual polymer chains and thereby enables molecular-weight analysis at the single-chain level. AFM-derived molecular-weight analysis further resolves heterogeneity within polymer samples and differentiates populations with different aggregate states, from single-chain-like to larger aggregate-like features. This AFM based workflow therefore enables estimation of the molecular weight of individual polymer chains, assessment of heterogeneity within polymer samples, and classification of detected polymer feature populations according to aggregate state.

The present workflow should nevertheless be interpreted as molecular-weight estimation rather than absolute mass determination. The AFM-derived values depend on topographic measurements of surface-supported features, the estimated polymer density, and the treatment of deconvolution and propagated uncertainty. Systematic underestimation of AFM height due to tip–sample and tip–substrate interactions, including van der Waals forces, may also contribute to underestimation of topographic volume and therefore of the AFM-derived molecular weight values.[17] In addition, the AFM readout is obtained from surface-supported objects that include both single-chain-like and aggregate-like populations, whereas GPC reports a bulk solution-state descriptor. The overall ordering of the AFM-derived distributions remains consistent with the corresponding GPC molecular weights, whereas the systematic numerical offset can be reconciled by the combined effects of AFM height underestimation and the different physical states probed by AFM and GPC.

Within this scope, AFM is best positioned not as a replacement for bulk molecular-weight analysis, but as a complementary methodology for resolving molecular-weight related variation across individual detected polymer features. This is particularly relevant in materials science and surface science, where

polymer behavior is often governed by molecular weight, aggregation state, and local heterogeneity rather than by bulk-average descriptors alone. The methodology described in this chapter therefore enables direct analysis of these parameters at the level at which individual surface-supported polymers are physically organized.

2.4 Supplementary information to:

Topography-Based AFM Analysis of Individual Polymer Chains for Molecular Weight Estimation

2.4.1 Methods

General Conditions

All commercial chemicals were used as received and stored under argon. Reagents were used without further purification unless stated otherwise. Unless specified, reactions were conducted in untreated glassware. For selected reactions requiring anhydrous conditions, oven-dried glassware (heated above 100 °C for at least 5 h) or vacuum-dried glassware treated with a heat gun (T > 200 °C) was used under oxygen- and moisture-free conditions. After weighing solids, glassware was connected to a Schlenk line, evacuated, and purged with nitrogen three times. Liquids were introduced via syringe through a rubber septum. Solvent abbreviations: *n*-hexane (n-hex), dichloromethane (DCM), tetrahydrofuran (THF), ethyl acetate (EA), N,N-dimethylformamide (DMF), and petroleum ether 40–60 (P.E.). All solvents were used as received without distillation.

Flash column chromatography was carried out on a Biotage® system using SiliCycle® precast silica gel columns (200–300 mesh or 300–400 mesh). Thin-layer chromatography (TLC) was performed on pre-coated, alumina-backed silica gel plates and visualized under UV light (254 nm) or by iodine staining.

NMR Measurements

^{1}H, ^{13}C{^{1}H}, and ^{19}F NMR spectra were recorded on a Bruker Avance III 400 MHz spectrometer at 298 K. Chemical shifts are reported in ppm on the δ scale and coupling constants (*J*) are given in hertz (*Hz*).

^{19}F NMR spectra were not referenced, while other chemical shifts were calibrated to residual non-deuterated solvent signals: $CDCl_3$ (δ = 7.26 ppm for ^{1}H, 77.16 ppm for $^{13}C\{^{1}H\}$). NMR data are described using the following abbreviations: chemical shift (δ, ppm), multiplicity (s = singlet, d = doublet, t = triplet, q = quartet, dt = doublet of triplets, m = multiplet, br = broad), and coupling constant (*J, Hz*).

Gel Permeation Chromatography (GPC) measurements

The polymer molecular weight (weight-average, M_w) and polydispersity (Đ) relative to polystyrene standards were determined on an Agilent Technologies 1200 GPC system. The system was equipped with a diode-array detector (DAD, G1315D, data collected at 250, 260, and 290 nm), a refractive index detector (RID, G1362A), autosampler (ALS, G1329A), binary pump (G1312A), and solvent degasser (G1322A). Separation was achieved using a VARIAN PLgel 5 μm MIXED-D column (300 × 7.5 mm, Part No. PL1110-6504). Calibration was performed with EasyVial PS-M and EasyVial PS-L polystyrene standards (Agilent Technologies), covering a molecular weight range from Mp 400 to 2,000,000 Da (Fluka). HPLC-grade *N*,*N*-dimethylformamide (DMF, Biosolve®, unstabilized) containing 0.1% LiBr (≥99%, Sigma-Aldrich) was used as the mobile phase. The elution rate was 1.0 mL/min, and all measurements were performed at room temperature or 25 °C. Samples and standards were injected at 10 μL (1.0 mg/mL).

AFM Sample Preparation

Sample deposition for atomic force microscopy (AFM) analysis was performed on two differently charged substrates: hydrophobic highly ordered pyrolytic graphite (HOPG) and negatively charged Mica. Sample preparation was realized by vacuum drying at room temperature by deposition of a 10 μL droplet of 0.5 μg/mL monomers/polymers solution in THF for and dried under vacuum in 3 s.

AFM Measurements

Atomic force microscopy (AFM) measurements were performed on a NX10 AFM (Park Systems, South Korea) operating in True Non-Contact™ Mode with a silicon tip SSS-NCHR (Park Systems, nominal spring constant 42 $N.m^{-1}$, nominal tip radii ~ 2 nm). Maps were acquired with a tip velocity of 0.4 μm per second. Map sizes with pixelization setting was employed: 1×1 μm^2 with 1 nm/px.

AFM Measurements Analysis

Image flattening and single polymers chains cross-sectional dimension analysis were performed by SPIP (Image Metrology, Denmark) and Mountains SPIP (Digital Surf, France) software. The image was first flattened with a first order polynomial fit for the global correction, and then, a zero-order least mean square (LMS) fit line-wise correction. Afterwards, the image was further flattened by first and second order LMS fit line-wise correction with area of interest masked.

2.4.2 SI Synthesis

Synthesis of Polymers

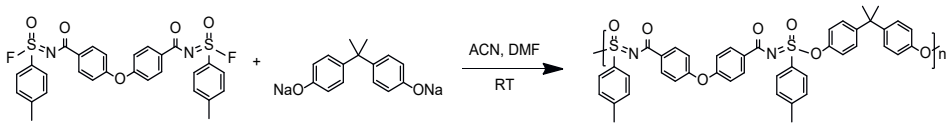

RS-diSF (RS-disulfonimidoyl fluoride) (25.0 mg, 0.044 mmol) and disodium bisphenol (12.0 mg, 0.044 mmol) were placed in a reaction vial under an argon atmosphere. Anhydrous ACN (0.1 mL, Biosolve HPLC grade) and anhydrous DMF (0.1 mL, Biosolve HPLC grade) were added, and the mixture was stirred vigorously for 48 hours. Methanol (10 mL) was then added to reduce the polymer's solubility, and stirring was paused to allow precipitation. The supernatant was removed carefully without disturbing the precipitate. The precipitate was redissolved in just enough THF (Biosolve HPLC grade, unstabilized) and reprecipitated with methanol. This redissolution–precipitation cycle was repeated eight times. The final polymer was dried in a vacuum oven at 50 °C overnight. Yield: 3.0 mg (0.0052 mmol, 12%), as a white powder.

The obtained compound is characterized with NMR, matching with literature[22]: ^{1}H NMR (400 MHz, $CDCl_3$) δ 8.13 (d, J = 8.0 Hz, 4H), 7.93 (d, J = 8.0 Hz, 4H), 7.35 (d, J = 8.0 Hz, 4H), 7.08 (d, J = 8.0 Hz, 4H), 7.00 (d, J = 8.0 Hz, 8H), 2.45 (s, 6H), 1.58 (s, 6H); ^{13}C NMR (101 MHz, $CDCl_3$) δ 171.05, 160.19, 149.45, 147.3, 145.83, 133.56, 132.04, 131.02, 130.07, 128.32, 128.17, 122.45, 118.46, 42.80, 30.92, 21.91. ^{19}F NMR (376 MHz, $CDCl_3$).

2.4.3 Supplementary Figure

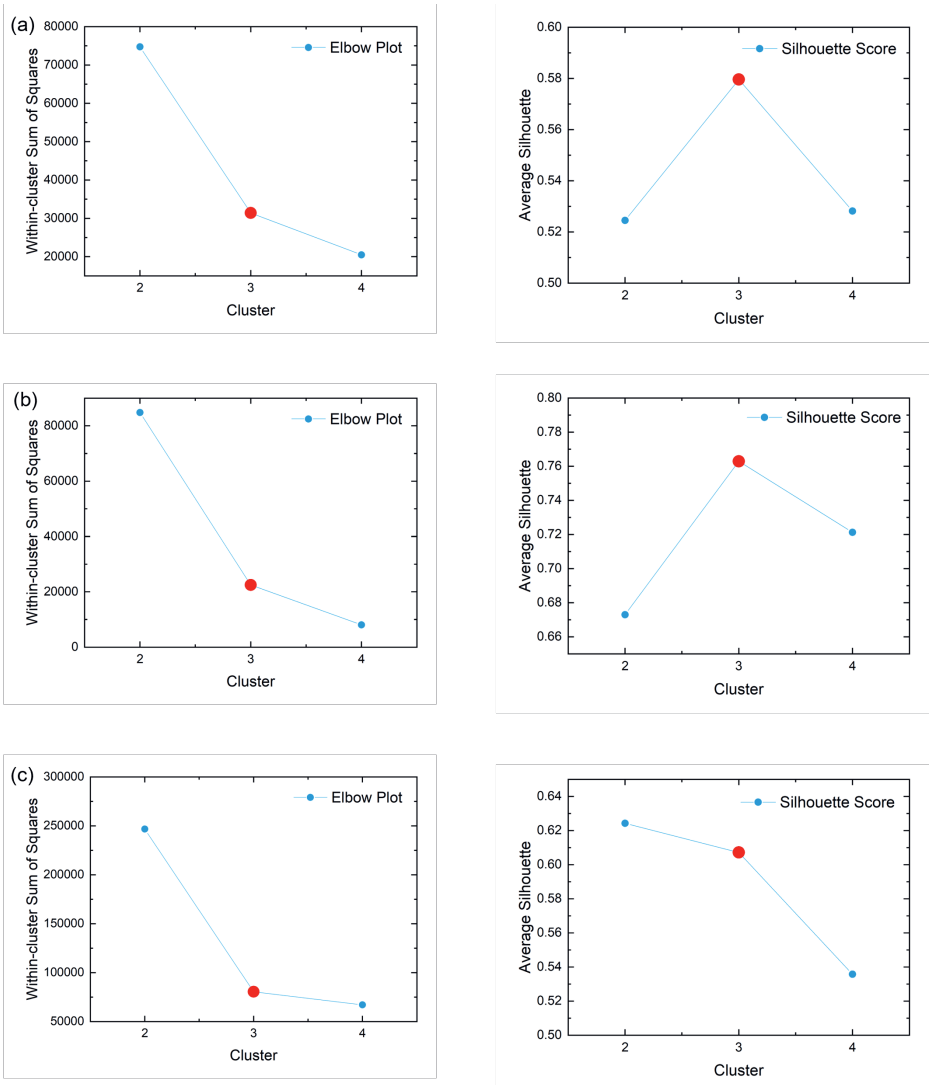

Supplementary Figure 2.1. Elbow and silhouette analysis for selection of cluster number in sample-wise k-means clustering. (a) 209 kDa sample; (b) 230 kDa sample; (c) 302 kDa sample. For each sample, the left panel shows the elbow plot of within-cluster sum of squares, and the right panel shows the average silhouette score for k=2, 3, and 4. Red circles mark the selected common partition at k=3.

2.4 References

(1) Gallegos, M. J.; Soetrisno, D. D.; Safi Samghabadi, F.; Conrad, J. C. Effects of Polymer Molecular Weight on Structure and Dynamics of Colloid–Polymer Bridging Systems. *J. Phys. Chem. B* **2023**, *127* (17), 3969–3978. DOI: 10.1021/acs.jpcb.3c01135.

(2) Gentekos, D. T.; Sifri, R. J.; Fors, B. P. Controlling polymer properties through the shape of the molecular-weight distribution. *Nat. Rev. Mater.* **2019**, *4* (12), 761–774. DOI: 10.1038/s41578-019-0138-8.

(3) Hu, J.; Sparrow, Z. M.; Ernst, B. G.; Mattes, S. M.; Coates, G. W.; DiStasio, R. A., Jr.; Fors, B. P. Designing Polymers with Molecular Weight Distribution-Based Machine Learning. *J. Am. Chem. Soc.* **2025**, *147* (12), 10238–10246. DOI: 10.1021/jacs.4c16325.

(4) Netopilík, M.; Podzimek, S. Retention Mechanism of Branched Macromolecules in Size Exclusion Chromatography. *ACS Omega* **2020**, *5* (24), 14254–14260. DOI: 10.1021/acsomega.9b03952.

(5) Fair, R. A.; Xie, R.; Lee, Y.; Colby, R. H.; Gomez, E. D. Molecular Weight Characterization of Conjugated Polymers Through Gel Permeation Chromatography and Static Light Scattering. *ACS Appl. Polym. Mater.* **2021**, *3* (9), 4572–4578. DOI: 10.1021/acsapm.1c00647.

(6) Izunobi, J. U.; Higginbotham, C. L. Polymer Molecular Weight Analysis by 1H NMR Spectroscopy. *J. Chem. Ed.* **2011**, *88* (8), 1098–1104. DOI: 10.1021/ed100461v.

(7) Nelson, T. F.; Ward, C. P. Diffusion-Ordered Spectroscopy for Rapid and Facile Determination of Consumer Plastic Molecular Weight. *Anal. Chem.* **2023**, *95* (22), 8560–8568. DOI: 10.1021/acs.analchem.3c00655.

(8) Marathianos, A.; Magiakos, A.; Han, Y.; Sanchez, A.; Whitfield, R.; Kammerer, J.; Anastasaki, A.; Wilson, P.; Patterson, J. P.; Barner-Kowollik, C.; et al. Atomic-Scale Imaging of Polymers and Precision Molecular Weight Analysis. *J. Am. Chem. Soc.* **2024**, *146* (50), 34292–34297. DOI: 10.1021/jacs.4c13812.

(9) Garcia, A. I. V.; Blum, S. A. Polymer Molecular Weight Determination via Fluorescence Lifetime. *J. Am. Chem. Soc.* **2022**, *144* (49), 22416–22420. DOI: 10.1021/jacs.2c10036.

(10) Yu-Su, S. Y.; Sun, F. C.; Sheiko, S. S.; Konkolewicz, D.; Lee, H.-i.; Matyjaszewski, K. Molecular Imaging and Analysis of Branching Topology in Polyacrylates by Atomic Force Microscopy. *Macromolecules* **2011**, *44* (15), 5928–5936. DOI: 10.1021/ma200821a.

(11) Liu, Y.; Vancso, G. J. Polymer single chain imaging, molecular forces, and nanoscale processes by Atomic Force Microscopy: The ultimate proof of the macromolecular hypothesis. *Prog. Polym. Sci.* **2020**, *104*, 101232. DOI: DOI: 10.1016/j.progpolymsci.2020.101232.

(12) Oliveira, O. N., Jr.; Caseli, L.; Ariga, K. The Past and the Future of Langmuir and Langmuir–Blodgett Films. *Chem. Rev.* **2022**, *122* (6), 6459–6513. DOI: 10.1021/acs.chemrev.1c00754.

(13) Sheiko, S. S.; da Silva, M.; Shirvaniants, D.; LaRue, I.; Prokhorova, S.; Moeller, M.; Beers, K.; Matyjaszewski, K. Measuring Molecular Weight by Atomic Force Microscopy. *J. Am. Chem. Soc.* **2003**, *125* (22), 6725–6728. DOI: 10.1021/ja0346779.

(14) Li, X.; Pujari, S. P.; van der Gucht, J.; Zuilhof, H.; Ruggeri, F. S. Unravelling emergence of chirality in click-chemistry polymers down to the single-chain level. *Nat. Commun.* **2025**, *16* (1), 6761. DOI: 10.1038/s41467-025-62041-0.

(15) Asadi, V.; Li, X.; Ruggeri, F. S.; Zuilhof, H.; van der Gucht, J.; Kodger, T. E. Synthesis of well-defined linear–bottlebrush–linear triblock copolymer towards architecturally-tunable soft materials. *Polym. Chem.* **2022**, *13* (32), 4666–4674, 10.1039/D2PY00841F. DOI: 10.1039/D2PY00841F.

(16) Ruggeri, F. S.; Sneideris, T.; Vendruscolo, M.; Knowles, T. P. J. Atomic force microscopy for single molecule characterisation of protein aggregation. *Arch. Biochem. Biophys.* **2019**, *664*, 134–148. DOI: 10.1016/j.abb.2019.02.001.

(17) Ruggeri, F. S.; Benedetti, F.; Knowles, T. P. J.; Lashuel, H. A.; Sekatskii, S.; Dietler, G. Identification and nanomechanical characterization of the fundamental

single-strand protofilaments of amyloid alpha-synuclein fibrils. *Proc. Natl. Acad. Sci. U.S.A.* **2018**, *115* (28), 7230–7235. DOI: 10.1073/pnas.1721220115.

(18) Li, H.; Chang, B. S.; Kim, H.; Xie, Z.; Lainé, A.; Ma, L.; Xu, T.; Yang, C.; Kwon, J.; Shelton, S. W.; et al. High-performing polysulfate dielectrics for electrostatic energy storage under harsh conditions. *Joule* **2023**, *7* (1), 95–111. DOI: 10.1016/j.joule.2022.12.010.

(19) Matsunaga, Y.; Fuchigami, S.; Ogane, T.; Takada, S. End-to-end differentiable blind tip reconstruction for noisy atomic force microscopy images. *Sci. Rep.* **2023**, *13* (1), 129. DOI: 10.1038/s41598-022-27057-2.

(20) Ruggeri, F. S.; Benedetti, F.; Knowles, T. P. J.; Lashuel, H. A.; Sekatskii, S.; Dietler, G. Identification and nanomechanical characterization of the fundamental single-strand protofilaments of amyloid α-synuclein fibrils. *Proc. Natl. Acad. Sci. U.S.A.* **2018**, *115* (28), 7230–7235. DOI: doi:10.1073/pnas.1721220115.

(21) Liang, D.-D.; Pujari, S. P.; Subramaniam, M.; Besten, M.; Zuilhof, H. Configurationally Chiral SuFEx-Based Polymers. *Angew. Chem. Int. Ed.* **2022**, *61* (8), e202116158. DOI: 10.1002/anie.202116158.

Chapter 3

Unravelling Emergence of Chirality in Click-Chemistry Polymers Down to the Single-Chain Level

This chapter has been published as: **Li, Xuecong**, Pujari, S.P., van der Gucht, J. et al. Unravelling emergence of chirality in click-chemistry polymers down to the single-chain level. *Nature Communications* **16**, 6761 (2025). https://doi.org/10.1038/s41467-025-62041-0

ABSTRACT

Chirality plays a critical role in the structure and function of natural and synthetic polymers, impacting their mechanical, optical, and electronic properties. However, a comprehensive understanding of the hierarchical emergence of chirality from monomers to macromolecular assemblies remains elusive, largely because of current limitations in studying their chemical-structural properties at the nanoscale. Here, we unravel the emergence of different forms of chirality from small molecules to their resulting polymers and supramolecular assemblies. We leverage bulk spectroscopic methods combined with the development of mechanical-acoustical suppressed infrared nanospectroscopy, to empower chemical-structural analysis of single-polymer chains. This ultra-high sensitivity allows identifying key functional groups as a signature for different forms of chirality: CH groups for central chirality in small molecules; C=O groups for backbone and supramolecular chirality in heterogeneous polymers. This work opens a new single-molecule chemical angle of observation into chirality and (bio)-polymers for the rational design in materials science, biotechnology, and medicine.

3.1 Introduction

Chirality plays crucial roles in the structure and functionalities of biomacromolecules and synthetic polymers.[1,2] Nucleic acids, proteins, natural carbohydrates, and several other naturally occurring polymers are composed of chiral building blocks contributing to their unique 3D structure and function, including biological recognition,[3] transcription,[4] and enzymatic processes.[5] Taking inspiration from nature, polymer scientists have designed innovative materials where specific arrangement of chiral centres allows unique mechanical,[6] optical,[7] and electronic[8] properties. However, understanding how to tune the molecular and chiral properties of polymers, to achieve new functionalities at the macromolecular level in advanced materials, remains a key challenge.[9]

A critical yet unresolved question is how chirality hierarchically emerges from the sub-molecular to the macromolecular level.[1] Previous work has studied the influence of molecular central chirality and polymerization conditions on polymer backbone chirality.[10-12] However, the mechanisms linking the stereochemistry of the small monomeric building blocks (central chirality), the arrangement and conformation of the polymer backbone (helical chirality), and the organization of single polymer chains in assemblies (supramolecular chirality) are still unclear.[13] This knowledge gap arises from the limits of current state-of-the-art analytical methods to characterize the complex manifestation of chirality in polymer systems across multiple length scales.

Bulk circular dichroism (CD),[14] infrared (IR) spectroscopy,[15] and vibrational circular dichroism[16] can provide insights into chirality of molecular systems. However, bulk methods cannot obtain single-molecule level information on heterogeneous systems; thus, they are not able to differentiate the diverse manifestations of chirality at the (sub)-molecular (central), backbone (helical), and assemblies (supramolecular) level.[17-19] Nano-imaging methods allow visualizing polymeric structures down to the single-chain level and excel in detailing their molecular and chiral conformations. Cryogenic electron microscopy (cryo-EM)[20] collects 2D images of single helical molecules with <0.5 nm resolution, although it is limited by the need for extensive sampling and computational 3D model reconstruction,[21] and has difficulties in reconstructing the structure of molecules with less-defined helices.[20] Atomic Force Microscopy (AFM)[22] can image the 3-D morphology of single polymers chains and their assemblies with angstroms resolution in the Z direction, and <1 nm resolution on the 2-D plane.[23]

However, both cryo-EM and AFM fall short in discerning chemical information, thereby limiting the understanding of backbone and supramolecular chirality emergence as a function of the central chirality of monomers.[18]

To unravel polymer properties, the chemical power of bulk spectroscopy and single-molecule imaging of AFM have been combined in nano-chemical imaging and spectroscopic techniques. Tip-enhanced Raman spectroscopy[24] and scattering scanning near-field optical microscopy allowed chemical imaging of single small organic molecules,[25] 2D monolayers,[26] or larger polymer systems.[27] However, because of scattering, plasmonic, and tip-reproducibility effects causing spectral deformation or band suppression, they are limited in extracting structural data from (bio-)organic polymers.[28,29] As a key advantage compared to scattering methods, AFM-based photothermal infrared nanospectroscopy (AFM-IR) has proven to acquire robust and reproducible nano-chemical and structural information from (bio-)organic polymers.[19] AFM-IR is free from scattering effects and independent of the surface/probe geometry.[30] While we have demonstrated to achieve AFM-IR single-molecule sensitivity, the method has up to now been limited to large biomolecules (>400 kDa), while requiring the enhancement of its signal at a gold probe/surface nanogap.[31] These technological and sensitivity constraints have precluded nanospectroscopic investigations of single polymer chains of smaller molecular weights and on different surfaces necessary to preserve their molecular conformations,[31] thus restricting polymer analysis primarily to mesoscopic and sub-micrometre scales on relatively homogenous model systems, such as monolayers,[32] block co-polymers[33] and polymer blends.[34,30]

Here, we gain molecular insights into the hierarchical emergence of chirality from single monomers (central) to polymers (backbone/helical) and their assemblies (supramolecular). To reach this objective, we designed a system with monomers and polymers possessing same connectivity, different chirality. We use racemic and chiral monomers to produce both racemic and homochiral (>99% ee) polymers of ~200 kDa, and their supramolecular assemblies, via enantiospecific click reactions.[35] We use a multiscale, correlative approach to identify and unravel the relationship among different forms of chirality (central, backbone, supramolecular), from bulk (CD,IR, UV-Vis) to single-chain and supramolecular assemblies imaging (AFM). To uncover the correlation between our bulk and single-molecule imaging observations, we then push the limits of AFM-IR nano-chemical analysis. We reach ultra-high sensitivity down to the single-chain level on non-metallic surfaces, revealing the chemical-structural origin of the emergence of supramolecular chirality. Our work paves the way

to generalise the characterisation of the mechanisms governing the emergence of chirality in (bio)-polymers, which is key for the rational design of innovative functional chiral macromolecules in healthcare and materials science.

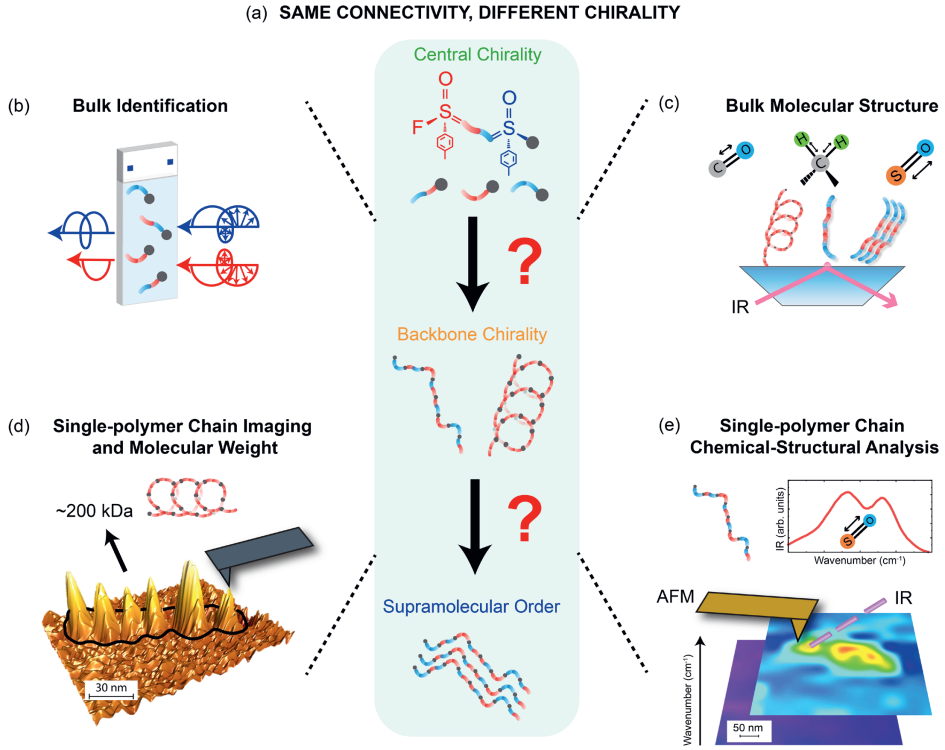

Figure 3.1: Unravel Origin and Emergence of Chirality in Polymers by Multiscale and Multimodal Bulk, Nano-Imaging and Nano-Chemical Analysis. (a) Our designed model system with identical connectivity but varying chiral configurations to study the link between central chirality in monomers, backbone chirality in polymers, and exploring how variations in chirality result in distinct supramolecular structures. Analysis in bulk with (b) CD, (c) FTIR, and at single molecule level with (d) AFM angstrom-resolution 3D imaging, (e) AFM-IR chemical analysis.

3.2 Results

3.2.1 Multiscale Analysis of Origin and Emergence of Chirality

Figure 3.1 illustrates our framework to perform a multiscale analysis of the emergence of chirality. While stereogenic centres in molecules define chirality, this term alone is insufficient to differentiate the different forms of chirality that emerge in polymeric systems over multiple length scales. We designed a same connectivity, different chirality system to unravel this hierarchical emergence (**Figure 3.1a**): i) from central chirality in small monomeric molecules: ii) to backbone chirality in single polymer chains, defined as the geometric configuration of the main axis of symmetry of the polymer induced by helical chirality; iii) and supramolecular order in their assemblies. We selected as model system chiral sulfur fluoride exchange (SuFEx) polymers, a novel class of environmentally friendly and sustainable polymers produced via click chemistry.[35,36]

To investigate how chirality manifests from the central chirality of molecules to the backbone and supramolecular chirality of polymers, we implemented a multimodal and multiscale approach (**Figure 3.1b-e**). We leveraged bulk Chiral High-Performance Liquid Chromatography (Chiral-HPLC), CD, IR and ultraviolet-visible (UV-Vis) spectroscopies (**Figure 3.1b-c**) to evaluate and compare the average chemical-structural properties of racemic and chiral monomers and polymers. AFM and AFM-IR empowered us to gain a single-molecule understanding of polymer morphology and chemical properties. Phase-controlled AFM nano-imaging allowed visualizing directly backbone helical chirality at the single-chain level, and unravelling heterogeneity among individual polymer chains and their supramolecular self-assemblies (**Figure 3.1d**).[37,38] The development of mechanical-acoustical suppressed AFM-IR enabled to correlate the morphological information with the corresponding molecular and chemical-structural properties of single-chains assemblies (**Figure 3.1e**).

3.2.2 The Chiral Building Blocks, Their Synthesis and Characterisation

Our framework with same connectivity but different chirality (**Figure 3.1a**) included monomers, linkers, repeating units, and polymers (**Figure 3.2a-c**, **Supplementary Fig. 3.1**).[18,35]

We synthetised two small molecules serving as building blocks of the polymers: a chiral molecule and a linker (**Figure 3.2a**, **Supplementary Fig. 3.1**, **Methods**). The chiral di(sulfonimidoyl fluoride) molecule (di-SF) had two chiral centres having R (red) or S (blue) configuration (**Figure 3.2a**). Molecules with mixed configurations were termed rac-monomers. Enantiopure chiral di-SFs molecules were termed χ-monomers. The linker is a symmetric bis(phenyl ether) (di-phenol) molecule, which is non-chiral and acted as linker for the polymerization (**Figure 3.2a**, link-monomer). The monomers and link-monomer were repetitively bonded via the SuFEx reaction to form the polymers (**Figure 3.2b**, **Supplementary Fig. 3.1**, **Methods**). Rac-monomers may lead to non-helical polymers termed here rac-polymer, while the χ-monomers may lead to polymers with helical backbone chirality, termed here χ-polymers. Gel Permeation Chromatography (GPC) determined a molecular weight (MW) and polydispersity (PDI) of (**Supplementary Fig. 3.2**): χ-polymer, Mn~209 kDa with Đ = 1.79; rac-polymer, Mn~220 kDa with Đ = 1.42.

To mimic the smallest χ- or rac-repeating unit of the polymers, we also synthesized a molecule consisting of a χ- or rac-monomer linked to a di-phenol link-monomer with an additional single methyl cap (**Figure 3.2c**, **Supplementary Fig. 3.1**, **Methods**). These repeating units allowed analysing the differences in chirality between monomers and the resulting polymers, focusing on structural differences rather than variations in the composition and presence of specific functional groups.

We finally synthetised both the RR and SS enantiomers of chiral χ-monomers, χ-repeating units, andχ-polymers; to compare their properties with the racemic (rac-) species. Our SuFEx-based polymer system with same connectivity, different chirality was here designed to enable the precise control of chirality (achieving 99% ee) while maintaining the same connectivity, making it an ideal platform for systematically studying structure-property relationships in chiral materials.

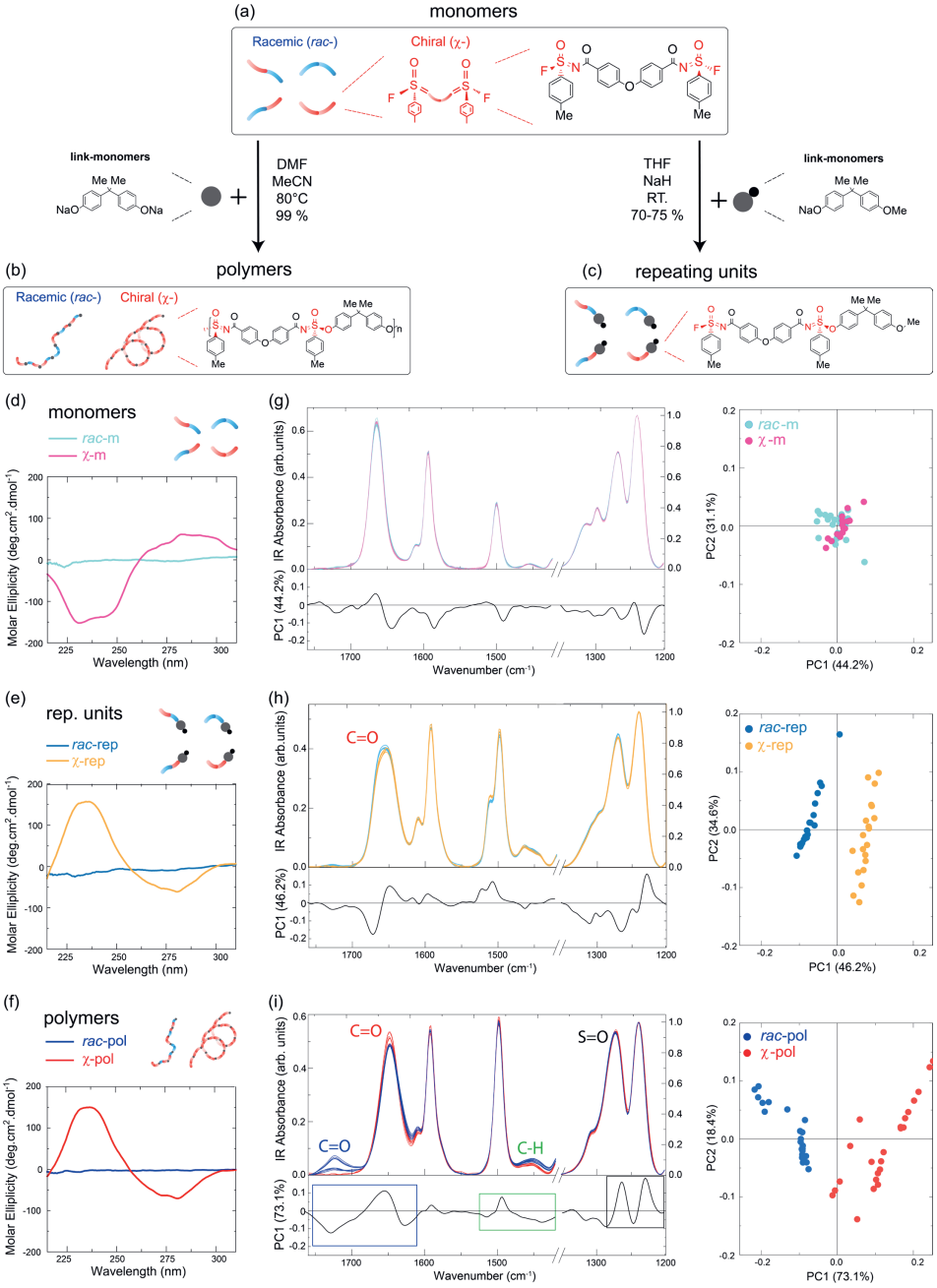

Figure 3.2. Bulk Identification of Chirality of Monomers, Repeating Units and Polymers with Same Connectivity but Different Chirality. Scheme of the SuFEx reaction pathways illustrating the synthesis of (a) racemic (rac-) and chiral (χ-) monomers with link-monomers to form: (b) rac- or χ-polymers; and the (c) repeating units, representing the building block of the polymer. (d-f) CD spectra of monomers, rep. units and polymers. (g-

i) Left: IR Spectra and loading plots of PC1 in the range from 1760-1200 cm^{-1}. For rac- and χ- monomers and repeating units: N=8 independent experiments, n=40 spectra each with 512 co¬-averaging; rac- and χ- polymers: N=9 independent experiments, n=50 spectra each with 512 co-averaging. (g-i) Right: PCA score plots analysis of rac- and χ- monomers, repeating units, polymers indicate statistically significant differences in the C=O and CH regions (see **Figure 3.3**).

3.2.3 Bulk Identification of Chirality

We first aimed to prove the presence or absence of chirality in our monomers, repeating units and polymers. We applied bulk chiral HPLC (**Supplementary Fig. 3.3**, **Supplementary Note 3.1**), CD (**Figure 3.2**, **Supplementary Fig. 3.4**, **Supplementary Note 3.2**) and Attenuated Total Reflection Fourier Transform Infrared (ATR-FTIR) spectroscopy (**Figures 3.2-3.3**, **Supplementary Fig. 3.5-3.7**, **Supplementary Note 3.3-3.4**) to investigate the general differences between chiral (χ-) vs racemic (rac-) species.

Chiral-HPLC allowed to separate and identify different enantiomers in the monomers and repeating units (**Supplementary Fig. 3.3**, **Supplementary Note 3.1**). For both monomers and repeating units, we had: i) rac-species with mixed configurations (RR, RS/SR, SS); ii) enantiomer pure chiral χ-species (RR, SS). Separation of chiral polymers was hampered by peak broadening due to polymers heterogeneity.[39]

We further used CD to identify chirality in all χ- versus rac- species, including polymers (**Figure 3.2d-f**, **Supplementary Fig. 3.4**, **Supplementary Note 3.2**).[40] Racemic molecules and polymers showed flat spectra, proving the absence of chiral asymmetry. Similar behavior was observed for isolated meso-monomers (100% RS/SR, **Supplementary Fig. 3.4**). All χ-species (RR, SS) showed a CD spectrum with two peaks (238 nm, 290 nm), proving chiral asymmetry. Yet, CD did not provide direct information on the configuration of chiral centres; nor does it differentiate between central chirality and new sources of chirality, such as backbone chirality emerging during polymer formation.[41]

To identify chirality at the molecular level and compare the χ- versus the rac-species, we then used ATR-FTIR spectroscopy (**Figures 3.2g-i**, **Supplementary Fig. 3.5-3.7**, **Supplementary Note 3.3-3.4**). Since symmetrical χ-enantiomers (RR, SS) have the same chemical properties, we focused on the RR species.

We acquired ATR-FTIR spectra in the mid-IR range of 3200-1000 cm^{-1}. We used chemometrics and Principal Component Analysis (PCA) to evaluate without bias the spectral differences in two spectral regions: 1800-1200 cm^{-1} (**Figure 3.2g-i**, **Supplementary Note 3.4**); 3200-2700 cm^{-1} (**Supplementary Fig. 3.5**).

The spectra and PCA score plots showed minor differences between rac- vs. χ- monomers (**Figure 3.2g-i**, **Supplementary Fig. 3.6**, **Supplementary Note 3.3**). Instead, we observed statistically significant differences along the first principal component (PC1) for the rac- vs. χ- species of the repeating units (46%) and the polymers (73%). In the 1800-1200 cm^{-1} region, these differences were associated with the: carbonyl group (C=O, 1780-1620 cm^{-1}, ~50%); carbon-hydrogen groups (C-H, 1550-1330 cm^{-1}, ~20%); and sulphonyl group (S=O, 1300-1200 cm^{-1}, ~30%). In the 3200-2700 cm^{-1} region (**Supplementary Fig. 3.6**), the differences were associated to the methyl groups (CH3, 2925-2800 cm^{-1}, ~60%). Overall, the FTIR analysis suggested that specific molecular bonds (C=O and CH_3) could be associated with chirality, with the largest differences observable in polymers.

3.2.4 Bulk Structural Differentiation of Forms of Chirality

We leveraged the molecular information contained in the IR spectra to unravel structural differences between χ- versus rac-species (**Figure 3.3**). PCA analysis (**Figure 3.2**) allowed to focus our analysis on the most significant spectral regions: i) methyl (CH_3) region, 3020-2800 cm^{-1} (**Figure 3.3a**); ii) the carbonyl (C=O) region, 1780-1620 cm^{-1} (**Figure 3.3b**). Our system with same connectivity but different chirality in turn ensured that the IR spectral differences could be attributed purely to different structural features.

CH_3 groups are abundant and often located directly or closely to chiral centres or the backbone of polymers.[42,43] Within 3020-2800 cm^{-1} the spectra showed significant differences between rac- vs. χ- species (**Figure 3.3a,c**). Monomers showed only minor differences (**Supplementary Fig. 3.5-3.7**). The repeating units instead showed a significantly higher IR absorption of the aromatic CH^3_{as} and CH^3_s groups for the rac- than the χ-species (**Figure 3.3c**), relative to the aliphatic CH3as (2970 cm^{-1}) in the link-monomer.

Our system with same connectivity with different chirality allowed to associate

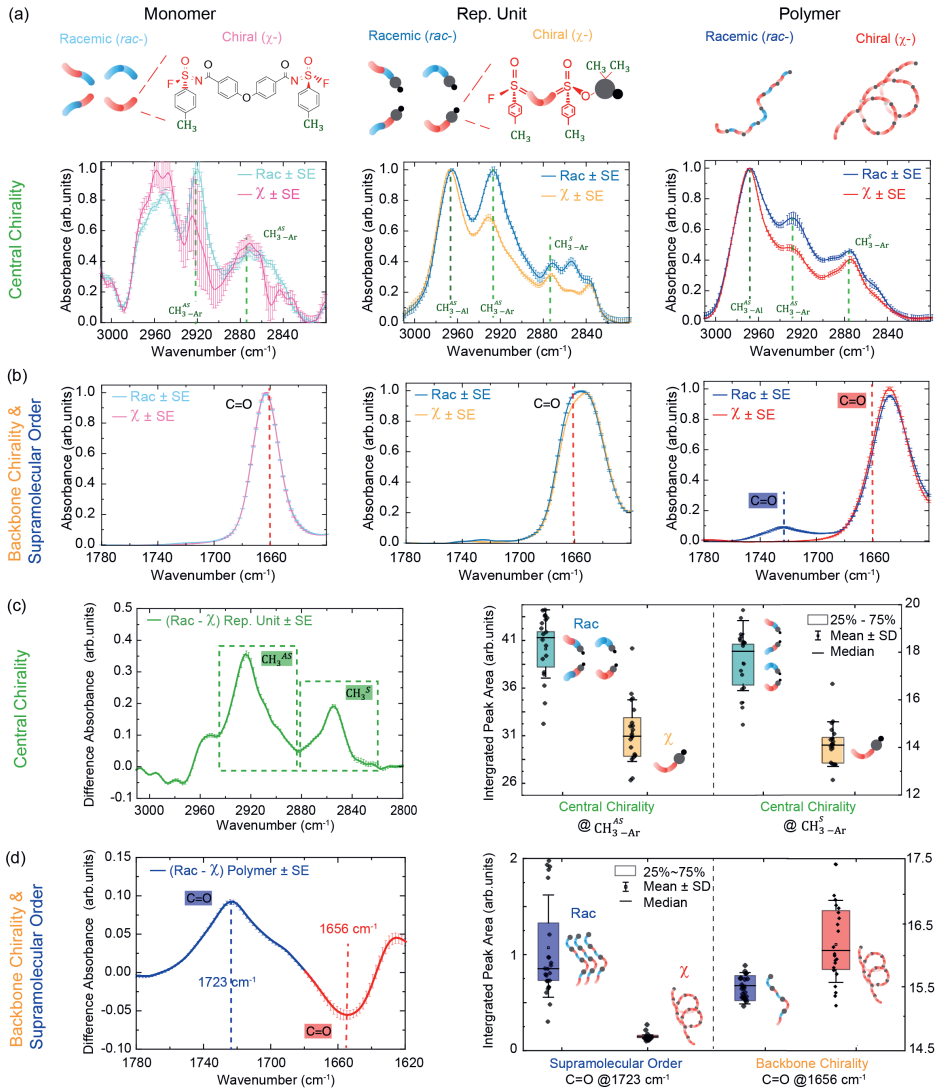

Figure 3.3. Bulk Spectroscopic Analysis of Molecules and Polymers with Same Connectivity but Different Chirality (a) ATR-FTIR spectra of monomer, repeating unit, polymers within CH_3 region (3020-2800 cm^{-1}) sensitive to central chirality. (b) C=O region (1780-1620 cm^{-1}) sensitive to backbone chirality and supramolecular order normalised to their maximum at the S=O peak at 1230 cm^{-1}. N=8 independent experiments, n=40 spectra with 512 co-averaging for monomers and repeating units; N=9 independent experiments, n=45 spectra with 512 co-averaging for polymers; error bars represent SE. (c) Left: Difference spectra for rac- minus χ-repeating units; error bars represent SE. Right: integrated peak areas at 2925 cm^{-1} and 2855 cm^{-1} (rac: green-blue, χ: orange, each data point represents the integration of the peak from a single spectrum), box plot has one SD as whiskers. (d) Left:

Difference spectra for rac- minus χ-polymers; error bars represent SE. Right: integrated peak areas at 1723 cm^{-1} and 1656 cm^{-1} (rac: blue, χ: red; each data point represents the integration of the peak from a single spectrum), box plot has one SD as whiskers.

the differences in IR absorption of the CH3 groups for monomers and repeating units purely to their central chirality (**Supplementary Note 3.4**).[8,42,44] The weaker IR absorption of χ-repeating units (RR) was associated with two less co-planar aromatic CH_3 groups; since these groups are arranged at fixed angles relative to the backbone, leading to reduced planarity because of steric constraints. The increased IR absorption of the rac-repeating units may instead be associated with the presence of a larger set of conformations (RR, SS, RS/SR), where the RS/SR conformations contribute to a higher IR absorption via a more planar configuration and enhancing electronic delocalization.

Thus, central chirality conformation was associated to an increased planarity of the rac-molecules compared to the χ-molecules. The polymers showed also differences in the C-H region, which however may also arise from polymerisation and phenomena such as backbone and supramolecular chirality.

The C=O stretching has been widely related to the structural conformation of the backbone of (bio)-polymers, such as protein.[15,45] In the range 1700-1620 cm^{-1}, monomers and repeating units did not show significant differences between rac- vs. χ-species, while the polymers showed statistically significant differences (**Figure 3.3b**, **Supplementary Fig. 3.7**, **Supplementary Note 3.4**). Thus, the spectral differences between rac- vs. χ-polymers could be ascribed only to other forms chirality arising from polymerisation and supramolecular assembly. We observed that (**Figure 3.3b,d**): i) the C=O peak shifted to lower wavenumbers from monomers (1663 cm^{-1}), via the repeating units (1655 cm^{-1}), to polymers (1648 cm^{-1}); ii) χ-polymers had higher absorption than rac-polymers at 1656 cm^{-1}; iii) χ–polymers exhibited a single C=O peak, while rac-polymers showed the emergence of a second C=O peak at 1723 cm^{-1}.

We associated the shift to lower wavenumbers to electron delocalization caused by the backbone formation in polymers.[46] For the χ-polymers, the increased IR absorption at 1656 cm^{-1} suggested the formation of helices in the backbone during the polymerisation process. Indeed, an IR absorption signature between 1650-1660 cm^{-1} is typically associated with the formation of χ-helix structure in protein, where the orientation of a specific sequence of amino acids stabilizes a secondary helical structure.[47] (**Figure 3.3d**, **Supplementary Note 3.4**). For

the rac-polymers, the emergence of the second C=O peak could be associated with (**Supplementary Note 3.4**): i) intramolecular interactions in their RS/SR repeating units, via a π-π resonance between the carbonyl groups and phenyl groups, inducing a planar conformation; ii) enhanced intermolecular π-π stacking of the RS/SR phenyls leading to supramolecular assembly and possibly higher chiral order.

To further investigate if emergence of the second C=O peak was associated with intra- or inter-molecular interactions, we conducted UV-Vis spectroscopy measurements on the racemic monomers and polymers as a function of their concentration in solution (**Supplementary Fig. 3.8**). The spectra of the polymers revealed a broadening and redshift of absorption peaks with increasing concentration, which are well-established indicators of π-π stacking intermolecular interactions.[48] These modifications were instead absent in the spectra of the monomers. Thus, UV-Vis indicated that rac-polymers undergo increased intermolecular π-π interactions rather than intramolecular.

Overall, the IR and UV-Vis structural analysis identified general key molecular vibrations useful to differentiate central chirality in small molecules (CH_3) and backbone/supramolecular chirality in polymers (C=O). The IR absorption of the CH_3 groups highlighted differences in conformation of the molecules associated with their central chirality, resulting in an increased planarity of the racemic molecules. The increased IR absorption of the C=O at 1656 cm^{-1} was associated with the emergence of backbone/helical chirality in the χ-polymers, while the C=O peak splitting and the new IR absorption at 1723 cm^{-1} might indicate increased intermolecular interactions in rac-polymers. However, bulk IR and UV-vis prevented studying sample heterogeneity at the single-molecule level to prove: i) presence of helicity in the backbone for χ-polymers; ii) supramolecular assembly for the rac-polymers, as suggested by the splitting of the C=O absorption and the emergent peak at 1723 cm^{-1}.

3.2.5 Single-molecule Imaging of Chirality with Angstrom Resolution

To unravel at the single-molecule level the origin of the emergence of chirality from small molecules to polymers, we further leveraged single-molecule 3D imaging. We investigated the presence of backbone helical chirality and the supramolecular assembly state of the rac- and χ-polymers with angstrom resolution imaging via phase-controlled AFM (**Figure 3.4**, **Supplementary Fig. 3.9-3.12**, **Supplementary Note 3.5**).[37]

AFM measurements must be performed on a surface, and performing the measurements on only one substrate could be limiting as it may bias the observed polymer morphology due to the specific surface charge of the substrate. To ensure a more comprehensive analysis, we studied the morphology of the polymers on three atomically-flat substrates with different charge: positive gold, negative mica, and hydrophobic HOPG. On hydrophilic gold and mica, the polymer formed large aggregates, whereas on hydrophobic HOPG the polymers showed their chain morphology for single-molecule analysis (**Supplementary Fig. 3.9**, **Methods**). HOPG was chosen for detailed analysis since, besides preserving polymeric structure, it also mimics the hydrophobicity of the diamond crystal used for the FTIR structural analysis.

AFM morphology maps on HOPG showed significant differences in shape and size of χ- versus rac-polymers (**Figure 3.4a**, **Supplementary Fig. 3.10**). A single-molecule statistical analysis of the volume of the polymers was conducted to estimate their molecular weight and polydispersity (**Supplementary Note 3.5**). The χ-polymers had AFM-measured molecular weight of 231.8 ± 138.9 kDa and PDI~1.36; while the rac-polymers had higher molecular weight of 1219 ± 1003 kDa and PDI~1.68. The comparison of single-molecule AFM and bulk GPC data (**Figure 3.4b**, **Supplementary Fig. 3.2**) demonstrated that χ-polymers maintained a single-chain conformation, while the rac-polymers self-assembled on the surface.

Ultra-high resolution AFM 3D imaging was further performed to unravel the topological structure of single rac- and χ-polymer chains. The AFM maps and the height cross-sectional profile of χ-polymer chains showed a helical structure (**Figure 3.4c**, **Supplementary Fig. 3.11**). The rac-polymers did not show any periodic structure at the single-chain level (**Figure 3.4d**). To quantitatively assess

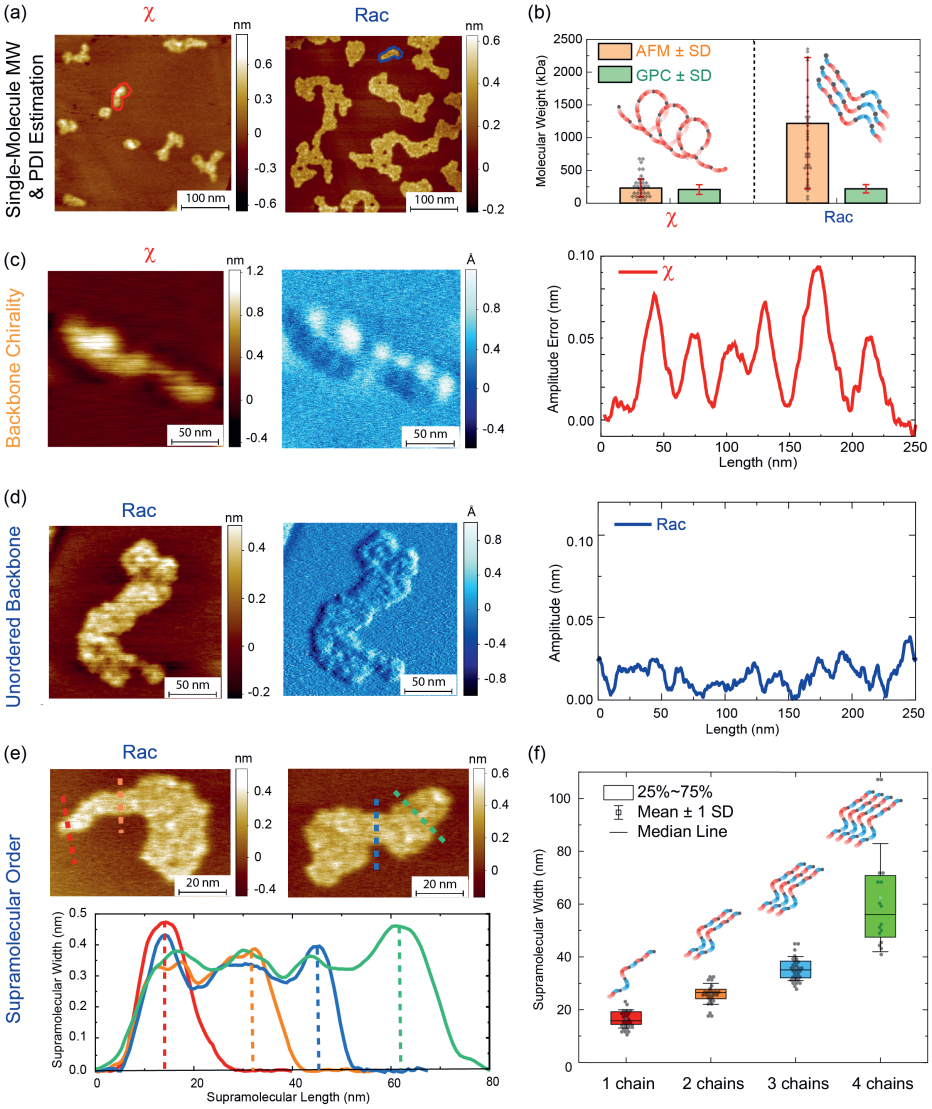

Figure 3.4. Nano-Imaging Analysis of Morphology and Supramolecular Assembly State of χ- and rac-polymer Chains. (a) AFM morphology maps of χ- (left) and rac- polymers (right). (b) Box plot comparing single-molecule volume-based molecular weight and polydispersity estimations by AFM (orange) and bulk GPC measurements (green) for χ- (left, n=33) and rac-polymers (right, n=42); error bars represent SD. (c, d) Ultra-high resolution AFM of morphology (brown-yellow) and amplitude error (blue) of single polymeric chains for (c) χ-polymer and (d) rac-polymer chains, together with their cross-sectional profile (smoothed using 3 pixels adjacent averaging, and a 7-points, 2nd order Savitzky-Golay filter). (e) AFM morphology map and cross-sectional profiles of the supramolecular assemblies of rac-polymers, made of one (red), two (orange), three (blue),

four (green) chains. (f) Box plot comparing the cross-sectional width of single (red) and assembled two (orange), three (blue), and four (green) rac-polymer chains (n=96); each data point is the width of a polymer, and box plot has one SD as whiskers.

the presence of a helical structure in χ- vs. rac-polymers, we calculated the Fast Fourier Transform (FFT) of the cross-sectional profiles of the single-chains against any possible residual periodicity on the HOPG surface (**Supplementary Fig. 3.11-3.12**). The FFT power spectra confirmed that χ-polymers had helical periodicity of ~40 nm, while single-chains of rac-polymers had no backbone periodicity.

Although rac-polymers did not have helical conformation, the AFM analysis showed that rac-polymers further self-assembled into ordered and periodic structures (**Figure 3.4a,e**). To unravel the supramolecular order of these rac-assemblies, we performed a single-molecule analysis of their shape as a function of their increasing size (**Figure 3.4e**). The smallest and most abundant rac-assemblies showed: a constant height of ~0.4 nm (**Supplementary Fig. 3.11**), which is the typical height of an organic chain on a surface; a transversal periodicity increasing in multiples of ~15 nm (**Figure 3.4f**), corresponding to the convoluted width of a single chain. This analysis indicated that the rac-polymers initially self-assemble via lateral interactions of single-chains, which further assembly into larger supramolecular species with increasing height (**Figure 3.5**).

Overall, the AFM single-molecule analysis was in excellent agreement with the IR structural results. AFM demonstrated that the χ-polymers have a helical backbone structure, in agreement with the C=O shift at lower wavenumber and increased IR absorption at 1656 cm^{-1}, which is a typical signature of helices in (bio)-polymers. It then showed that rac-polymers undergo self-assembly via lateral interactions; in agreement with FTIR conclusion that emergence of a new second C=O peak at 1723 cm^{-1} could be associated to intramolecular π-π resonances in the RS/SR polymeric-units with a co-planar conformation and their supramolecular assembly via intermolecular π-π stacking. However, structural analysis of rac-polymers by AFM nano-imaging and IR structural analysis separately could not prove directly whether the emerging C=O at 1723 cm^{-1} had an intra- or inter-molecular origin. To unravel the origin of this structural signature, we further applied AFM-IR nano-chemical analysis.

3.2.6 Achieving Single Polymer Chain Nano-Chemical Analysis

Chemical-structural analysis of single polymer chains and assemblies paves the way for understanding the molecular origin of the emergence of supramolecular order in the rac-polymers. However, to date, AFM-IR single-molecule sensitivity has been limited to molecules >400 kDa; and only if placed at a metallic nanogap between a gold surface and AFM probe. Indeed, the use of non-metallic substrates like HOPG would cause a further drop in AFM-IR sensitivity larger than 10-folds.

To allow the chemical analysis of single polymer chains of molecular weight down to ~200 kDa on non-metallic surfaces, such as HOPG, we developed acoustical-mechanical suppressed (AMS) AFM-IR with sub-Angstrom noise level (**Figure 3.5**, **Supplementary Fig. 3.13-3.14**). AFM-IR works by detecting the photothermal expansion of a sample after its absorption of IR light. This detection mechanism is highly sensitive to external mechanical and acoustic noise, with typical frequencies between 0-500 Hz, which can propagate into the cantilever and reduce the signal-to-noise ratio of the detected photothermal signal (**Supplementary Fig. 3.13**).[49] We leveraged composite foams, with absorption frequencies between 0-4 kHz to isolate the surfaces of our instrument from acoustical and mechanical noise, and its electronic controllers from ground oscillations (**Figure 3.5a**, **Methods**). This isolation overall suppressed the noise transduced to the AFM cantilever, while measuring the photothermal signal. It thus allowed to achieve RMS noise of 25 ± 5 pm in tapping-IR and 60 ± 5 pm in contact-IR modes. The low level of noise in turn allows chemical-imaging of monoatomic steps of HOPG with ~3 Å height (**Figure 3.5b**, **Supplementary Fig. 3.13-3.14**). To further allow single-molecule localisation with high-accuracy, we reduced AFM thermal drift by stabilising room temperature with variations <0.1 °C/h (**Supplementary Fig. 3.13**).[50]

We then applied AMS AFM-IR to extract structural information of single polymer chains from nano-resolved IR maps and spectra as in bulk FTIR. We first focused on χ-polymers (**Figure 3.5c-f)**. Tapping-IR allowed achieving multimodal imaging of morphology and IR absorption of a single polymer chain with a height down to ~5 Å (**Figure 3.5c**); the phase locked loop (PLL) tracking of contact resonance frequency assured that chemical contrast was not affected by mechanical effects. Next, we pointed the AFM probe on a single polymer chain in the map (**Figure 3.5d**) to acquire nano-localised IR spectra (**Figure**

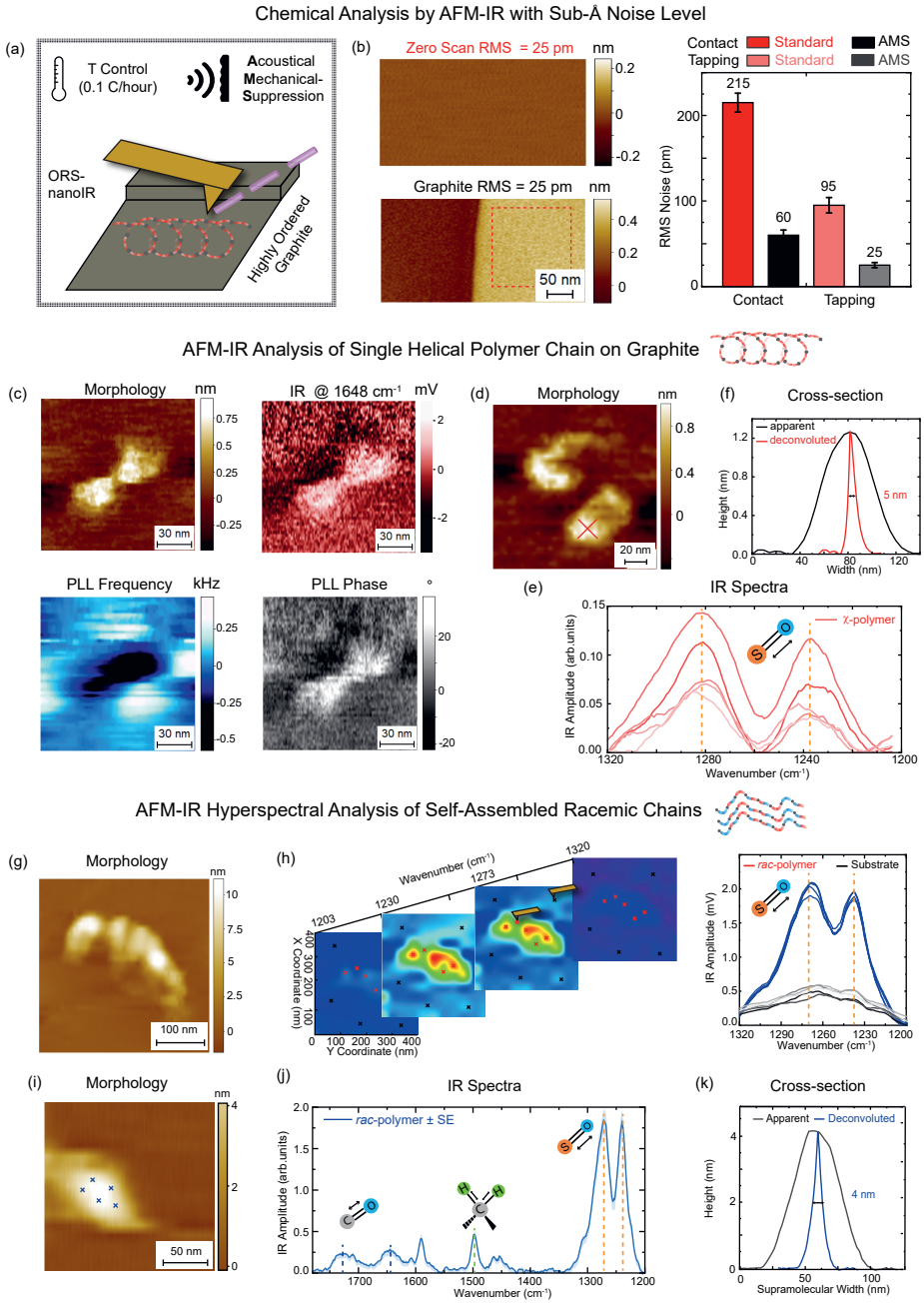

Figure 3.5. Nano-Chemical Imaging and Spectroscopy of Single Polymer Chains. (a) Schematic of the technological advances for acoustical mechanical suppression (AMS), which empowers chemical analysis with picometer-sensitivity by AFM-IR. (b, left) Morphology maps of bare HOPG in tapping mode in zero scan (top) and finite scan

(bottom) by AMS AFM-IR (red-dashed box indicates area used for RMS calculation). (b, right) RMS noise of AFM-IR with and without AMS in tapping and contact modes; error bars represent sensitivity uncertainty and SE of three different areas within the same map. (c-f) Single-chain χ-polymer nano-chemical analysis by AMS AFM-IR. (c) Morphology, IR amplitude, PLL frequency and PLL phase of a single polymer chain. (d) Morphological map of two single χ-polymer chains, with location of single-molecule IR spectrum indicated (cross). (e) Cross-sectional and deconvoluted polymer profiles at the cross location. (f) IR Spectra acquired on the single polymer chains showing characteristic S=O peaks (red cross, panel d). (g-k) Single-Chains rac-polymer nano-chemical analysis by AMS AFM-IR. (g) Morphology map of an assembly of a few single rac-polymer chains. (h) Left: Hyperspectral 4D plot (x-y coordinates, z-axis wavenumber, colour scale absorption intensity) with slices at 1203, 1240, 1273 and 1320 cm^{-1}. Right: Two sets of representative spectra (background and polymer indicated by AFM probe). (i) Morphology map of another assembly of single rac-polymer chains. (j) Corresponding IR spectra from marked positions (shading represents SE). (k) Cross-sectional and deconvoluted polymer profiles.

3.5e); for chains with a size down to ~0.8 nm height and ~5 nm width (**Figure 3.5f**), corresponding to a molecular weight of ~200 kDa. While preserving better topography, tapping-IR detection was limited to the S=O region of a single χ-polymer chain by low signal-to-noise ratio (SNR).

We thus employed contact-IR mode to detect the chemical properties of rac-polymers (**Figure 3.5g-k**, **Supplementary Fig. 3.15**). **Figure 3.5g** shows a representative rac-polymer assembly. Instead of single wavenumber IR maps (**Figure 3.5c**), we acquired 4D hyperspectral chemical maps of the polymers. **Figure 3.5h** shows four 3D-slices of the hyperspectral map, where each pixel represents an IR spectrum. The IR spectra showed the typical S=O absorption of the rac-polymer; while the HOPG surface showed significantly lower and uncorrelated IR absorption, which was subtracted to correct the spectra of the polymers (**Supplementary Fig. 3.14-3.15**). The high SNR allowed acquiring nano-localised spectra of single rac-polymer assemblies in the full 1800-1200 cm-1 fingerprint region (**Figure 3.5i-j)**, for assemblies with a size down to ~4.5 nm in height and ~4 nm in width, corresponding to ~2-4 chains (**Figure 3.5k**, **Supplementary Fig. 3.15**).

The emerging supramolecular C=O stretching at 1723 cm^{-1} was observed in all acquired IR spectra of different rac-assemblies (**Supplementary Fig. 3.15**), but with significant variations between different assemblies. We thus proceeded to a statistical analysis of their nano-chemical heterogeneity by AMS AFM-IR.

3.2.7 Unravelling the Origin of the Emergence of Supramolecular Chirality

We leveraged AFM-IR ultra-high sensitivity to investigate how the chemical signature of the rac-polymers varied as a function of their size and supramolecular state, to unravel if the emerging C=O at 1723 cm^{-1} is related to intra- or inter-molecular interactions (**Figure 3.6**, **Supplementary Fig. 3.15**).

We acquired AFM-IR spectra from racemic polymers assemblies with varying size, from the smallest one (**Figure 3.6a**, height ~4.5 nm; deconvoluted radius ~4 nm) to the largest ones (**Figure 3.6b**, height ~10 nm; deconvoluted radius ~6 nm). Although at the limit of AFM-IR sensitivity, smaller assemblies showed lower IR signal than larger ones in accordance with Beer-Lambert Law (**Figure 3.6c**, **Supplementary Fig. 3.15**).

To reduce spectral variability due to IR absorption intensity and perform a PCA analysis in the fingerprint region of protein (1750-1200 cm^{-1}), we normalized the IR spectra to their maximum. The PCA analysis showed that smaller (3.0-6.4 nm) and larger assemblies (7.5-15 nm) belong to separate spectroscopic clusters with 95% confidence (**Figure 3.6c**). Significant part of the observed spectroscopic difference between the two clusters related to the conformation of the C=O group (**Figure 3.6e**), thus indicating with statistical significance that rac-polymers of different sizes may have different structural properties.

To evaluate structural differences in the backbone and interactions between our rac-polymers, we consequently focused our analysis on the C=O groups (**Figure 3.6f**, 1780-1600 cm^{-1}). Indeed, the emergence of the second C=O at 1725 cm^{-1} was associated by IR and UV-Vis with inter-molecular interactions in the rac-polymers. We normalised the spectra to the backbone C=O peak at 1646 cm^{-1}, to investigate the structural differences related to the emergent C=O peak at 1723 cm^{-1}; independently of the number of C=O bonds present in the assemblies. The shape of the emergent C=O peak was significantly different for smaller assemblies compared to larger ones, as confirmed with 95% confidence by PCA analysis of the second derivatives of the spectra (**Figure 3.6g**). The PC1 loading plot of the second derivatives proved with statistical significance (**Figure 3.6h**, 81% variance) that larger assemblies had increased absorption of the emergent C=O peak compared to smaller assemblies. Moreover, larger assemblies showed a shift of the C=O maximum at higher wavenumber at 1730 cm^{-1}, compared to smaller

assemblies having a lower absorption peak at 1710 cm^{-1}. Since we normalised the spectra to the backbone C=O peak (1646 cm^{-1}), these modifications could only be associated to an increasing number of intermolecular (π-π stacking) interactions between the rac-polymer chains in the larger assemblies; rather than a constant number of intramolecular interactions in the single chains.

Overall, AMS AFM-IR proved the ability of studying the heterogeneous chemical-structural properties of single polymeric assemblies, composed of only few chains. The analysis enabled identifying the splitting of the C=O group absorption and the second peak at 1723 cm^{-1} as key signature of intermolecular π-π stacking, and of the emergence of supramolecular order and chirality in the rac-polymers (**Figure 3.6i**). The single-molecule results provided by AFM-IR were thus in excellent agreement with the independent spectroscopic evidence provided above by the IR and UV-Vis structural analysis.

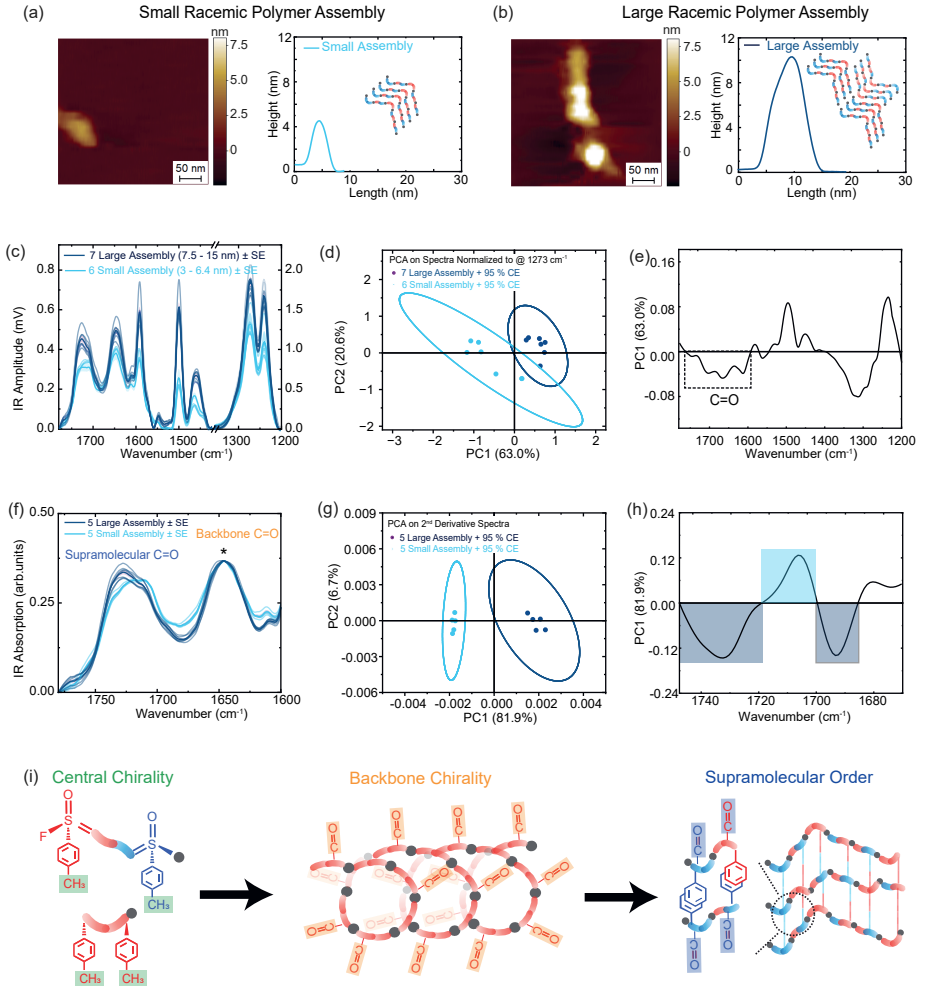

Figure 3.6. Nano-Chemical Analysis of the Emergence of Supramolecular Chirality in Heterogeneous Rac-polymer Assemblies. AFM Morphology maps of characteristic (a) large and (b) small racemic assembly. (c) AFM-IR spectra of several racemic assemblies normalized to 1273 cm^{-1} (**Supplementary Fig. 3.15**); shading represents SE. (d) Score plot of PCA analysis of the normalized spectra in (c) with 95% confidence ellipses (CE). (e) Loading plot of the spectra highlighting the molecular bonds related to the variance difference. (f) Zoomed spectra from 1780 – 1600 cm^{-1}, normalized to 1646 cm^{-1} (C=O peak); shading represents SE. (g) PCA Score Plot of second derivatives of spectra in (f) with 95% confidence ellipses (CE). (h) Loading plot of PC1 of the second derivatives highlighting the structural features of the small vs. large assemblies. (i) Schematic of the key molecular bonds used to identify and discriminate the emergence of different forms of chirality; from central chirality in molecules (CH_3), to backbone chirality in polymers (C=O at 1646 cm^{-1}), supramolecular order in assemblies (C=O at 1725 cm^{-1}).

3.3 Discussion

Despite over a century of investigations, the hierarchical emergence of chirality over multiple chemical and topological scales has remained elusive due to technological limitations in characterizing different forms of chirality at the molecular nanoscale.[9]

To bridge this gap, we have elucidated the complex interplay between central chirality in small molecules and the emergence of backbone and supramolecular chirality in polymers from sub-molecular scales to macro-molecular scales. To reach this objective, we have developed acoustical-mechanical suppressed AFM-IR to achieve chemical-structural analysis of the heterogeneity and assembly of single-polymer chain(s). This ultra-high sensitivity, combined with nano-imaging and bulk spectroscopy, enabled distinguishing between different forms of chirality and their structural manifestation at the molecular level via bonds generally present and abundant in small molecules, polymers and their supramolecular assemblies (**Figure 3.6i**). Introducing the concept of same connectivity, different chirality to discern and study different forms of chirality, we first identify the conformation of CH groups as a key signature of central chirality in small molecules. Second, we generalised the idea that C=O carbonyl is sensitive in polymers to backbone helical structure and self-assembly via π-π intermolecular stacking,[51,52] as in the case of χ-helical structure in single protein[51,52] and supramolecular stacking and ordering during their assemblies.[14,15]

Overall, the presented results contribute to understanding the hierarchical emergence of chirality in polymers and pose a new framework for offering key insights into the structural-chemical determinants of chirality across multiple scales. This understanding will be in turn fundamental for the rational design of advanced chiral materials with tailored properties and may help to accelerate the development of novel materials in electronics, chemical industry, biotechnology, and healthcare. Indeed, the concept of same connectivity, different chirality is not limited to synthetic polymer systems, but can be generalized to other chemistries allowing for modular design and stereospecific control. For example, backbone chirality also underlies protein secondary structures such as α-helices and β-sheets, which are crucial for the tertiary organization of human designed proteins and their functionality.[53]

Finally, this study pushes the limits of nano-analytical chemistry down to the

identification of the molecular fingerprint and the structural analysis of a single polymer chain on any surface, without requiring the enhancement of metallic surfaces. These capabilities pave the way to have a new single-molecule and angstrom resolved window of observation into the chemical-structural properties of virtually any (bio-)organic material in nature.

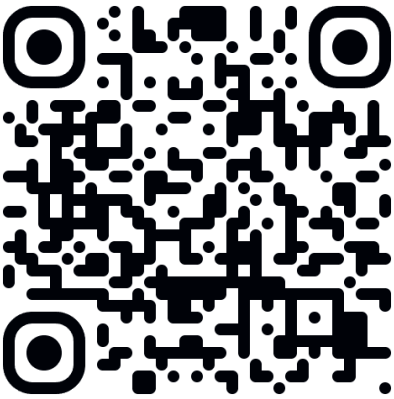

Link to the Original Paper

3.4 Supplementary information to:

Unravelling Emergence of Chirality in Click-Chemistry Polymers Down to the Single-Chain Level

1. Supplementary Notes

3.1 Chiral-HPLC

Chiral-HPLC allowed separating and identifying the presence of enantiomers in the monomers and repeating units (**Supplementary Fig. 3.1-3.3**), by leveraging the selective retention of enantiomers based on their unique interactions with chiral stationary phases (CSPs). The results of the measurements showed that our *rac*-monomers had a chromatogram with three peaks, thus each peak corresponded to one of the four possible chiral configurations (*R,R*) (25%), (*R,S*)/(S,R) (50%), and (*S,S*) (25%) where the presence of a plane of symmetry in the molecule renders the (*R,S*) and (S,R) configurations equivalent. While the *rac*-repeating units had a chromatogram with four peaks, corresponding to the four possible configurations: (*R,S*), (S,R), (*R,R*) or (*S,S*), where the plane of symmetry is absent resulting in the (S,R) and (*R,S*) configurations being distinct. Both the χ-monomers and χ-repeating units had a chromatogram with a single peak, demonstrating that they are chirally pure enantiomers. However, while effective at separating enantiomers, Chiral-HPLC alone does not allow to determine the absolute configuration on central chirality, as it only distinguishes them based on their interactions with the CSPs. Via comparison with established literature, which reported similar retention times using the same column[35], we concluded that we have *racemic* and enantiopure RR chiral configurations systems. Chiral-HPLC was not able to separate chiral polymers, as their heterogeneity leads to peak broadening that typically yields significant overlap in the peaks of enantiomeric polymers.

3.2 CD interpretation and Cotton Effect

CD allowed to study the asymmetry of the monomers, repeating units and polymers allowing to identify chirality in bulk, by measuring the difference in absorbance of left- and right-circularly polarized light and thus differentiating chiral asymmetry (**Figure 3.2**, **Supplementary Fig. 3.4**). The non-enantiospecific monomers, repeating units, and racemic polymers exhibit negligible CD bands with intensity of $\Delta\varepsilon_{max}$=24.4, $\Delta\varepsilon_{max}$=25.8, $\Delta\varepsilon_{max}$=8.7 (**Figure 3.2b**, *light blue*, *green blue* and *blue curves*). The absence of a CD response demonstrated a balanced mixture of the enantiomers in our sample, indicating that there was no enrichment of any particular chiral configuration as (*R,R*), (*R,S*), (*S,R*), or (*S,S*), thus confirming they are racemic species. To confirm the absence of chirality,

RS monomers alone were synthesized, and these also did not exhibit CD peaks (**Supplementary Fig. 4**).

The RR (and SS) χ-monomers, χ -repeating units, and χ -polymers showed two major peaks at 238 nm and 290 nm, demonstrating chiral asymmetry (**Figure 3.2b**). The χ-monomers (*magenta curve*) exhibited a prominent peak with an absorption maximum at 238 nm ($\Delta\varepsilon_{max}$=152.8) indicating the presence of chiral centers and reflecting the asymmetry in the structure of monomers.[13] The χ-repeating units (*orange curve*) demonstrated a similar trend, with an absorption maximum at 234 nm (which is slightly shifted compared to the monomers. This shift in the absorption peak is indicative of differences in the chemical structure in the repeating units. The χ-polymers (*red curve*) also exhibited significant peak at 236 nm ($\Delta\varepsilon_{max}$=156.1), though with slightly altered positions and intensities, reflecting the more complex chiral arrangement within the polymers.

We observed that that RR- and SS- monomers showed opposite CD signals due to the Cotton effect (**Figure 3.2d-f**). Moreover, the respective χ-monomers exhibited inverse signs of the peaks compared to the corresponding χ-repeating units and χ-polymers. This reversal of the sign of the peaks, attributed to variations in the electronic transitions affecting the differential absorption of circularly polarized light, is commonly known as Cotton effect. The Cotton effects observed in the spectra – a negative effect for the monomers at 238 nm followed by a positive effect at 290 nm, and a reverse-sign cotton effect for the repeating units and polymers – were in accordance with the chiral nature of the molecules. The reversal in the Cotton effects is attributed to the known rearrangement of the chiral centre during the S_N2 reaction of the SuFEx process.[35]

Overall, the comparison of the CD spectra of the racemic and chiral species confirmed the presence or absence of central chirality in the monomers and repeating unit molecules. Minor differences in the spectra of χ-repeating units versus χ-polymers were observed, suggesting the possibility of distinct structural chiral features beyond central chirality. Slight differences in the positions and intensities of peaks in the CD spectra of the χ-repeating units vs. χ-polymers indicate that, in addition to central chirality, there might be distinct structural features leading to chirality. While CD signals suggest the presence of central chirality also in the polymers, they do not provide direct information on the absolute configuration of chiral centres, nor can definitively differentiate between central vs. backbone chirality.[3]

3.3 Principal Component Analysis (PCA) of IR Spectra of Polymers

PCA was performed to extract the most relevant spectral features from the Infrared (IR) spectra of the racemic and chiral polymers, focusing on two primary regions: 1800 - 1200 cm^{-1} and 3500 - 2600 cm^{-1} (**Figure 3.2**, **Supplementary Fig. 3.5**). These regions are routinely investigated in IR spectroscopy due to their abundance of spectral information pertaining to the vibrational modes of many common chemical bonds.

Analysis of the 1800 - 1200 cm^{-1} Region:

Within this region, PCA was instrumental in highlighting the carbonyl stretching region of 1780-1620 cm^{-1}. In **Figure 3.2**, the *rac*- and χ-polymers were distinctly separated along the first principal component (PC1). The most prominent features of PC1 in this region were an absolute maximum at 1723 cm^{-1} and a nearby peak at 1656 cm^{-1}. These peaks are indicative of carbonyl stretching vibrations, which are inherent to *rac*- and χ-polymers.

Analysis of the 3500 - 2600 cm^{-1} Region:

PCA similarly studied the methyl stretching region (3020-2800 cm^{-1}) within the broader 3500-2600 cm^{-1} range. (**Supplementary Fig. 3.6**) The *rac*- and χ-polymers exhibited clear separation on PC1, indicating significant differences in the methyl group conformations and their associated stretching vibrations.

In summary, the application of PCA was essential in enabling us to select the most statistically relevant regions from within the broader IR spectral ranges for focused analysis. By directing our attention to the carbonyl stretching region (1620 - 1780 cm^{-1}) within the 1800 - 1000 cm^{-1} region and the methyl stretching region (3020 - 2800 cm^{-1}) within the 3500 - 2600 cm^{-1} range, PCA facilitated a more targeted and effective interpretation of the complex IR spectra.

3.4 Infrared Spectroscopy Analysis of Racemic vs Chiral Polymers

We leveraged the molecular information contained in the IR spectra to unravel structural differences between our racemic vs. chiral molecules and polymers (**Figure 3.3**). Thanks to our design of a system with same connectivity but different chirality, the spectral differences between *rac*- and χ- species were purely associated to their specific structural features. The PCA analysis (**Figure**

3.2) focused our analysis on the spectral regions where the largest significant differences were discernible. We thus investigated quantitatively how chemical differences may be related to different forms of chirality for the: i) CH_3 region, 3020-2800 cm^{-1} (**Figure 3.3a**); ii) the C=O region, 1780-1620 cm^{-1} (**Figure 3.3b**).

We first focused on CH_3 groups (**Figure 3.3a**, **Supplementary Fig. 6**), because they are abundant and often located directly or closely (i.e. via aromatic rings) to chiral centres of molecules or the backbone of polymers.[7,8,42,44]

Monomers and repeating units can only have central chirality. Thus, the spectral differences between *rac*- vs. χ- species allowed identifying how the conformation of CH_3 groups correlates to central chirality. To evaluate the changes between *rac*- and χ-species, we performed a difference spectroscopy analysis (**Figure 3.3c, Supplementary Fig. 3.7**). The IR spectra of *rac*- and χ-monomers showed minor differences, while the repeating units showed statistically significant differences in the aromatic antisymmetric (CH_3^{as}, 2925 cm^{-1}) and symmetric (CH_3^{s}, 2875 cm^{-1}) methyl stretching. The integration of the area of the difference peaks showed that the aromatic CH_3^{as} and CH_3^{s} groups had higher IR intensity for the *rac*-repeating units than the χ-species (**Figure 3.3c)**; relative to the absorption of the aliphatic CH_3^{as} stretching (2970 cm^{-1}) in the link-monomer. The weaker IR absorption of χ-repeating units (RR) may be associated with two less co-planar aromatic CH_3 groups, with a fixed angle with respect to the backbone.[8] The *rac*-repeating units (RR, SS, RS, SR) had a larger set of conformations, where the increased IR absorption may be instead associated with the RS/SR species with more co-planar aromatic CH_3 groups. Thus, central chirality in the χ– vs. *rac*-species was associated with a different conformational state of aromatic CH_3 groups and increased planarity of racemic (RS/SR) molecules.

Similar differences in the CH_3 groups were observed for the polymers (**Figure 3.3a**, **Supplementary Fig. 3.6-3.7**), suggesting a more co-planar structure for the racemic polymers compared to chiral ones. However, the differences in the spectra may also arise from polymerisation, affecting the conformation of the methyl groups, and other possible emerging phenomena such as backbone and supramolecular chirality.

We next focused on the C=O stretching (1700-1600 cm^{-1}, **Figure 3.3b**), since it is known to be related to the structural conformation of the backbone of (bio)-polymers.[15,45] We observed two major differences: the C=O peak shifted to lower wavenumbers from 1663 cm^{-1} for the monomers, via 1655 cm^{-1} for the repeating

units, to 1648 cm^{-1} for the polymers; chiral species had a single C=O peak, while *rac*-polymers showed the emergence of a second C=O peak at 1723 cm^{-1}.

The C=O shift to lower wavenumbers is related to electron delocalization, which may be caused by the polymerization and stabilisation of helices;[46,53] and to the possible supramolecular assembly via π–π stacking of the phenyl groups in our molecules and polymers.[47] The presence of two C=O peaks for the polymers may further correlate to different structure and assembly states of the rac- vs. χ- species.

To discriminate the origin of the differences between rac- vs. χ- species, we further performed a difference spectroscopy analysis (**Supplementary Fig. 3.7**). Monomers did not show significant changes. Repeating units showed only minor changes at 1660 cm^{-1}. Polymers showed significant changes between 1780-1620 cm^{-1} (**Figure 3.3d**). The χ-polymers had higher IR absorption than *rac*-polymers at 1656 cm^{-1}, which is typically associated with helices in bio-polymers, thus suggesting the emergence of a regular helicity in the backbone χ-polymers by reorienting the carbonyl groups.[15,51,52] Instead, *rac*-polymers showed the emerging extra C=O absorption at 1723 cm^{-1}. Thus, we suggest that the emergence of the additional C=O peak in the *rac*-polymer is related to: i) intramolecular interactions in their RS/SR repeating units, via a π–π resonance between the carbonyl groups and phenyl groups, inducing a planar conformation;[16] ii) intermolecular π–π stacking of the RS/SR phenyls leading to supramolecular assembly and possibly inducing chiral order.[47]

Overall, the IR structural analysis identified general key molecular vibrations useful to differentiate central chirality in small molecules (CH_3) and backbone/ supramolecular chirality in polymers (C=O). The absorption of aromatic CH_3 groups allowed differentiating the variability in conformation of central chiral groups in rac- vs χ-species, suggesting a more co-planar structure for the racemic molecules and polymers. The IR absorption of the C=O group at 1656 cm^{-1} could be used to determine the emergence of backbone helical chirality in χ-polymers. While the occurrence of a splitting of the C=O and the appearance of an extra peak at 1723 cm^{-1} was related to the presence of intramolecular π–π resonances in RS/SR species or their further supramolecular assembly via π–π stacking intermolecular interactions. Yet, bulk IR does not allow visualizing and differentiating backbone chirality (C=O at 1656 cm^{-1}) from supramolecular assembly and cannot probe sample heterogeneity at the single-molecule level, to determine whether the emergent C=O at 1723 cm^{-1} is related to an intramolecular

planar conformation or supramolecular assembly of the polymers.

3.5 AFM-Based Determination of Polymer Molecular Weight and Polydispersity

To perform a single-molecule estimation of the molecular weight of polymers maps obtained, we utilized an AFM volume-based estimation of polymer molecular weight and dispersity. We used probes with: i) radii equal <7 nm for AFM; radii <30 nm (gold coated) for AFM-IR. To ensure the consistency and reproducibility of our measurements, Phase Control AFM[37] was employed. This technique ensures we avoid applying excessive force on the polymers, facilitating consistent and reliable measurements across different measurements.

The identification of the polymer particles in the maps was conducted through a height filtering algorithm. By employing a threshold that is set at three times the Root Mean Square (RMS) roughness of the surface, we effectively excluded noise, thereby ensuring the selection of features are truly representative body of the polymers. The 3-D volume of the particle was then measured by Scanning Probe Image Processor (SPIP), a software developed by Image Metrology, Denmark. Additionally, the "preserve holes in shapes" function was enabled in the software, considering the possible coiled nature of the polymers and providing a more realistic representation of their morphology.

Lastly, the estimation of the molecular weight was accomplished by multiplying the calculated volume by the density of common sulfonate polymers, typically around 1.2 g/cm^3, and then multiplied by using Avogadro's number (6.022×10^{23} mol^{-1}) to convert to kDa.

2. METHODS

General Conditions of Materials Synthesis

All commercial chemicals were used as received and stored under argon. Reagents were used without further purification unless otherwise noted.[35] Unless otherwise noted, all reactions were performed using glassware without further preparation. Certain reactions were carried out under anhydrous conditions. For these reactions, glassware was oven-dried at temperatures exceeding 100°C for at least 5 h, or was dried under vacuum with a heat gun (T > 200 °C), under oxygen-free and water-free conditions.

After weighing any solids, the glassware was connected to a Schlenk line and then placed under vacuum and flushed with nitrogen gas (3× purged). Liquids were added via a syringe through a rubber stopper. The following solvent abbreviations are used: n-hexane (n-hex), tetrahydrofuran (THF), ethyl acetate (EA), N,N-dimethylformamide (DMF), and petroleum ether 40-60 (P.E.). For HPLC and GPC analysis, all solvents were purchased from Biosolve®. Extra-dry solvents were purchased from Acros Organics. Commercial solvents were obtained from Honeywell. These solvents were used as received without any distillation.

All reagents were used as received, following the procedure we have used in a previously published method from our group: Benzenesulfinic acid sodium salt (98%), 1,8-diazabicyclo[5.4.0]undec-7-ene (98%), sodium hydride (60% dispersion in mineral oil), 4,4′-oxybis (benzoic acid) (99%), bisphenol A (≥99%), were purchased from Merck Life Science N.V. Oxalyl chloride (98%), p-toluenesulfinic acid sodium salt (97%), triphenyl phosphine (99%), methyl iodide (99%) and potassium carbonate (≥99%) were purchased from Fisher Scientific B.V. and Selectfluor (98%) were purchased from Fluorochem Ltd. Flash column chromatography was performed using a Biotage® system using SiliCycle® precast silica columns (200–300 mesh or 300–400 mesh). TLC analysis was performed on pre-coated, alumina-backed silica gel plates. TLC plates were analyzed by UV fluorescence (254 nm) or I_2 staining.

Synthesis of Monomers

Synthesis of N',N"-(4,4'-oxybis(benzoyl))bis(4-methylbenzenesulfonimidoyl fluoride) (**rac-monomers**) and N'(R),N"(R)-(4,4'-oxybis(benzoyl))bis(4-

methylbenzenesulfonimidoyl fluoride) (χ-**monomers**) were synthesized by reacting 4,4'-oxybis(N-(p-tolylsulfinyl)benzamide) with NaH in THF to form an intermediate, which is then treated with Selectfluor and KOAc in EtOH at 0°C to room temperature.[35]

Characterisation of Monomers

To characterize the purity of the **monomers**, we performed NMR and HRMS analysis, as reported below:

rac-monomers:

^{1}H NMR (400 MHz, $CDCl_3$): δ 8.18 (d, J = 8.5 Hz,4H), 8.08 (d, J = 8.1 Hz, 4H), 7.48 (d, J = 8.1 Hz, 4H), 7.08 (d, J = 8.5 Hz, 4H), 2.53 (s, 6H);

^{13}C NMR (101 MHz, $CDCl_3$): δ 169.2, 160.5, 147.2, 132.3, 131.6 (d, J = 20 Hz), 130.3, 129.9, 128.0, 118.6, 21.8.

HRMS (ESI) m/z: $[M+Na]^+$ calc. for $C_{28}H_{22}F_2N_2O_5S_2Na$: 591.0830, found: 591.0834.

χ-monomers:

^{1}H NMR (400 MHz, $CDCl_3$): δ 8.09 (d, J = 8.5 Hz,4H), 7.98 (d, J = 8.1 Hz, 4H), 7.36 (d, J = 8.1 Hz, 4H), 6.98 (d, J = 8.5 Hz, 4H), 2.42 (s, 6H);

^{13}C NMR (101 MHz, $CDCl_3$): δ 169.2, 160.5, 147.2, 132.3, 131.6 (d, J = 20 Hz), 130.3, 129.9, 128.0, 118.6, 21.9.

HRMS (ESI) m/z: $[M+Na]^+$ calc. for $C_{28}H_{22}F_2N_2O_5S_2Na$: 591.0830, found: 591.0830.

Synthesis of the Polymers

The polymer was synthesized with slight modifications as follows. In a 2 mL Biotage microwave glass vial containing a magnetic stir bar, bis(4-methylbenzene sulfonimidoyl fluoride) **1** (100 mg, 1.0 equiv.) and disodium bis-phenolate **2** (47.9 mg, 1.0 equiv.) were added inside an argon-filled glovebox (MBRAUN's MB 20

G-LMF gas purifier with H_2O and O_2 values of <0.1 ppm).[35] The vial was placed on a magnetic stirring plate, and 1.00 mL of anhydrous acetonitrile (Acros organics 99.9+% Extra Dry over Molecular Sieve, AcroSeal®) and 1.00 mL of anhydrous N,N-dimethylformamide (Acros organics 99.9+%, absolute, over molecular sieves (H_2O ≤0.01%), ≥99.8% (GC), AcroSeal®) were added with vigorous stirring. The vial was then sealed with caps. The polymerizations were heated at 80°C. After stirring at 80°C in the glovebox for approximately 24 h, the glass vial was removed from the glovebox, and 0.5 mL of DMF was added. The vial was shaken to facilitate dissolution, and the resulting solution was slowly poured into 50 mL of MeOH while continuously stirring. After precipitation occurred, the stirring was continued for an additional 10 minutes. After allowing the formed precipitate to settle for 10 minutes, the methanol layer was removed, and a minimal amount of DMF was added to redissolve the precipitate. This cycle of precipitation, sedimentation, and redissolution was repeated four times. The resulting white powder/fibrous material was transferred to a 4 mL glass vial and dried at 50°C under vacuum for a minimum of 12 h. GPC measurements of the resulting polymers were conducted using a DMF:LiBr (0.1%) mixture as the eluent solvent.

Characterisation of Polymers

To characterize the purity of the polymers, we performed NMR analysis. The results are reported below:

rac-polymers:

^{1}H NMR (400 MHz, $CDCl_3$): δ 8.04 (d, J = 8.0 Hz, 4H), 7.86 (d, J = 8.0 Hz, 4H), 7.27 (d, J = 8.0Hz, 4H), 6.99 (d, J = 8.0 Hz, 4H), 6.93 (d, J = 8.0 Hz, 8H), 2.39 (s, 6H), 1.50 (s, 6H);

^{13}C NMR (101 MHz, CDCl3): δ 170.88, 160.07, 149.32, 145.48, 133.48, 132.27, 131.90, 130.91, 130.30, 129.92, 128.18, 128.02, 122.31, 118.32, 42.66, 30.77, 21.86, 21.75.

χ-polymers:

^{1}H NMR (400 MHz, $CDCl_3$): δ 8.04 (d, J = 8.0 Hz, 4H), 7.86 (d, J = 8.0 Hz, 4H), 7.27 (d, J = 8.0Hz, 4H), 7.00 (d, J = 8.0 Hz, 4H), 6.93 (d, J = 8.0 Hz, 8H), 2.37 (s, 6H), 1.51

(s, 6H);

^{13}C NMR (101 MHz, CDCl3): δ 170.89, 160.06, 149.32, 147.17, 145.68, 133.44, 132.32, 131.90, 130.89, 130.30, 129.92, 128.18, 128.02, 122.31, 118.57, 118.32, 67,99, 42.66, 30.78, 25,62, 21.88, 21.77.

^{19}F NMR (376 MHz, $CDCl_3$): δ 65.25.

Synthesis of Modified Monomers and Repeating units

Synthesis of 4-(2-(4-methoxyphenyl)propan-2-yl)phenol (**link-monomers with a methyl cap**): An oven-dried 250 mL round-bottomed flask was prepared with a magnetic stirbar and a rubber septum. The flask was charged with Bisphenol-A (5.0 gm, 21.9 mmol) was dissolved in dry DMF (50 mL), followed by the addition of potassium carbonate (3.0 gm, 21.9 mmol). The mixture was cooled to 0 ℃ with an ice bath, and a solution of methyl iodide (3.1 gm, 21.9 mmol) was added dropwise over 5 minutes. The mixture was stirred at 0 ℃ for approximately 2 h and then left to stir overnight. The reaction was then diluted with water (10 mL) and extracted with EtOAc (15 mL × 2). The combined organic layers were washed with water (15 mL × 2), saturated aqueous NaCl (15 mL), and dried over anhydrous sodium sulfate. The solvent was removed, and the crude material was purified by flash chromatography on silica gel (petroleum ether: ethyl acetate 8:2) to afford 5.1 g (96%) of 4-(2-(4-methoxyphenyl)propan-2-yl)phenol (**link-monomers with a methyl cap**) as a colorless oil.

Synthesis of 4-(2-(4-methoxyphenyl)propan-2-yl)phenyl N-(4-(4-((fluoro(oxo)(p-tolyl)-l6-sulfaneylidene)carbamoyl)phenoxy) benzoyl)-4-methylbenzenesulfonimidate (**rac-repeating units**) and/or 4-(2-(4-methoxyphenyl)propan-2-yl)phenyl (S)-N-(4-(4-(((R)-fluoro(oxo)(p-tolyl)-l6-sulfaneylidene)carbamoyl)phenoxy)benzoyl)-4-methylbenzene sulfonimidate (χ-**repeating units**): **rac-repeating units** and χ-**repeating units** were synthesized according to a protocol adapted from the literature.[54] In brief: a 100 mL round-bottomed flask was dried in an oven and fitted with a rubber septum and a magnetic stirbar. To the flask, 25.0 mg (0.044 mmol) of SuFEx (χ-**monomers** or **rac-monomers**) compound and 10.6 mg (0.044 mmol) of 4-(2-(4-methoxyphenyl) propan-2-yl)phenol (**link-monomers with a methyl cap**) were added in 1 mL dry THF, followed by the addition of 2.0 mg (0.044 mmol) of Sodium hydride (60% in oil). The mixture was stirred under argon at room temperature and monitored by thin layer chromatography (TLC). The reaction was stopped by adding 10

mL of water and the resulting mixture was extracted with CH_2Cl_2 (3 x 50 mL). The organic phase was dried using anhydrous $MgSO_4$ and the crude product was purified by column chromatography on silica gel, using a mixture of EtOAc and n-hexane in the ratio of 1:19 to 1:4 as the eluent. The final yield was 24 mg of 70% (**rac-repeating units**) or 26 mg of 75% (**χ-repeating units**), and both obtained as white solids.

Characterisation of Repeating units

To characterize the purity of the **repeating units**, we performed NMR and HMRS analysis. The results are reported below:

rac-repeating units:

^{1}H NMR (400 MHz, $CDCl_3$): δ 8.16-8.12 (m, 4H), 8.07 (d, 2H, J = 8.0 Hz), 7.96 (d, 2H, J = 8.0 Hz), 7.46 (d, 2H, J = 8.0 Hz), 7.37 (d, 2H, J = 8.0 Hz), 7.16 (d, 2H, J = 8.0 Hz), 7.08-7.00 (m, 8H), 6.79 (d, 2H, J = 8.0 Hz), 3.77 (s, 3H), 2.51 (ss, 6H), 1.61 (s, 6H).

^{13}C NMR (101 MHz, $CDCl_3$): δ 171.00, 169.38, 160.98, 159.80, 157.73, 150.49, 147.29, 147.07, 145.73, 142.29, 133.66, 132.46, 132.42, 132.08, 131.39, 130.42, 130.03, 129.67, 128.37, 128.19, 128.15, 127.83, 122.27, 118.72, 118.43, 113.51, 55.35, 42.31, 31.06, 29.85, 22.02, 21.90.

^{19}F NMR (376 MHz, $CDCl_3$): δ 65.27. (**Supplementary Fig. 3.3**)

HRMS (ESI) m/z : [M+H] + calc. for $C_{44}H_{40}O_7N_2FS_2$: 791.2255, found: 791.2256.

χ-repeating units:

^{1}H NMR (400 MHz, $CDCl_3$): δ 8.16-8.12 (m, 4H), 8.07 (d, 2H, J = 8.0 Hz), 7.96 (d, 2H, J = 8.0 Hz), 7.46 (d, 2H, J = 8.0 Hz), 7.38 (d, 2H, J = 8.0 Hz), 7.16 (d, 2H, J = 8.0 Hz), 7.08-7.00 (m, 8H), 6.79 (d, 2H, J = 8.0 Hz), 3.77 (s, 3H), 2.51 (ss, 6H), 1.61 (s, 6H).

^{13}C NMR (101 MHz, CDCl3): δ 170.97, 169.35, 161.00, 159.81, 157.76, 150.49, 147.28, 147.10, 145.71, 142.30, 133.74, 132.42, 132.08, 131.79, 131.43, 130.42,

130.02, 129.71, 128.38, 128.20, 128.15, 127.84, 122.27, 118.72, 118.43, 113.54, 55.35, 42.32, 31.07, 29.85, 22.01, 21.90.

^{19}F NMR (376 MHz, $CDCl_3$): δ 65.27.

HRMS (ESI) m/z: [M+H] + calc for $C_{44}H_{40}O_7N_2FS_2$: 791.2252, found: 791.2256.

NMR Measurements

A Bruker Avance III 400 MHz spectrometer was used to record ^{1}H NMR, ^{13}C NMR, and ^{19}F NMR spectra at a temperature of 298 K. The chemical shifts are listed in ppm on the δ scale and coupling constants were recorded in Hertz (Hz). The 19F NMR was not referenced. All other chemical shifts are calibrated relative to the signals corresponding of the non-deuterated solvents ($CHCl_3$: δ = 7.26 ppm for ^{1}H and 77.16 ppm for ^{13}C, DMSO: δ = 2.50 ppm for ^{1}H and 39.52 ppm for ^{13}C, CH3CN: δ = 1.94 ppm for ^{1}H and 1.32 and 118.26 ppm for ^{13}C). Abbreviations are used in the description of NMR data as follows: chemical shift (δ = ppm), multiplicity (s = singlet, d = doublet, t = triplet, q = quartet, dt = doublet of triplets, m = multiplet, br = broadened), coupling constant (J, Hz).

HR-MS measurements

The Quadrupole Time-of-Flight (QTOF) micro-spectrometer (Thermo Fisher Scientific Inc., United States) was used to obtain high-resolution mass spectra (HR-MS) through electrospray ionization (ESI) in either positive mode (ESI+) or negative mode (ESI-).

HPLC measurements

Enantioselectivity was monitored using high-performance liquid chromatography (HPLC, Agilent 1100 bearing a UV-Vis detector) with a CHIRALPAK® IA column (5 µm, 4.6 mm x 250 mm). As references, racemic products or nonchiral mixtures, including diastereoisomers, were synthesized to determine the column conditions for baseline separation. Unless specifically mentioned, these were found to be n-hexane/dichloromethane/iso-propanol (80/20/2.5) as the mobile phase, a flow rate of 0.5 mL/min, room temperature, and a detector wavelength of 240 nm.

GPC measurements

Gel Permeation Chromatography (GPC) was performed using an Agilent Technologies 1200 system, equipped with a diode-array detector (DAD, G1315D), a refractive index detector (RID, G1362A), autosampler (ALS, G1329A), bin pump (G1312A), solvent degasser (G1322A), and a VARIAN GPC/SEC column from PLgel 5 μm MIXED-D (300 × 7.5 mm). The system was calibrated with EasyVial PS-M and EasyVial PS-L polystyrene standards (Agilent Technologies), GPC polystyrene standards with a combined range from Mp 400 to 2,000,000 Da (Fluka). HPLC-grade tetrahydrofuran (THF, Biosolve®, unstabilized, HPLC grade) was used as a mobile phase for low molecular weight polymers and high molecular weight polymers were measured using HPLC grade N,N-Dimethylformamide (DMF, Biosolve®, unstabilized, HPLC grade) with 0.1% LiBr (ReagentPlus®, ≥99% from Sigma-Aldrich). . All GPC measurements were performed at room temperature or at 25 °C using an injection volume of 10 μL (1.0 mg/mL). The polymer number average molecular weight (M_n) and polydispersity (Đ) relative to a set of polystyrenes were determined using DAD (at 270 nm or 290 nm) or RI detectors.

FTIR measurements, Data Treatment and Analysis

Attenuated total reflection infrared spectroscopy (ATR-FTIR) was performed using a Bruker Tensor 27 IR equipped with Platinum ATR accessory with a diamond ATR element. Spectra were collected by the built-in software OPUS (version 7.8, Bruker, USA). The samples were deposited on the ATR crystal by 2 times of 0.5 μL droplet at a concentration of 2 mg×mL^{-1} in THF. Spectra were acquired at the range of 3500 cm^{-1} - 500 cm^{-1} with a resolution of 4 cm^{-1}. All spectra were processed using OriginPro (version 2022b, OriginLab, USA). For each sample, 5 spectra of 512 co-averages were collected. Since the spectral background line shape slightly depends on wavenumber regions and at lower wavenumber range (2500 - 500 cm^{-1} range) and higher wavenumber range (3500 - 2500 cm^{-1} range) does not share the same baseline. The spectra were first cut into two ranges that contains relevant information: lower wavenumber range (1800-1000 cm^{-1} range) and higher wavenumber range (3150-2700 cm^{-1} range). The final spectra for each range were obtained by averaging 5 individual spectra. Each spectrum was smoothed using a Savitzky–Golay filter (second order, 7pts), baseline-corrected (zero-order for 1800-1000 cm^{-1} range and first-order for 3150-2700 cm^{-1} range) and normalizing to the range [0,1].

Circular dichroism measurements

Circular Dichroism (CD) measurements were done on a Jasco J-715 spectropolarimeter equipped with a Peltier holder. CD spectra were measured at a concentration of 20 μg×mL^{-1} in a Hellma® Quartz Glass high performance macro absorption cell with a 0.1 cm pathlength. Measurements were performed with a scanning speed of 50 nm×min^{-1} with a data pitch of 0.5 nm at 20 °C and were averaged from 16 scans. All spectra were processed using OriginPro (version 2022b, OriginLab, USA). The final spectra were obtained by first subtraction of THF background, secondly, applying a Savitzky–Golay filter (second order, 21 pts) and finally converting to molar ellipticity by the following formular: , where is averaged molecular weight in g×mol^{-1}, is the path length (0.1 cm) and is the concentration [mg×mL^{-1}].

UV-Vis Measurements

UV-Vis measurements were done on a Shimadzu UV-2600 spectrometer. Spectra were measured in THF with a Hellma® Quartz Glass high performance macro absorption cell with a 0.1 cm pathlength. Measurements were performed in the range of 185-600 nm with a scanning speed of 1 nm×s^{-1} with a data pitch of 1nm, at room temperature, and with 16 co-averages. All spectra were processed using OriginPro (version 2022b, OriginLab, USA).

AFM Sample Preparation

Samples deposition for atomic force microscopy (AFM) analysis was performed on three differently charged substrates: hydrophobic highly ordered pyrolytic graphite (HOPG), negative charged Mica and positive gold. Sample preparation was realized by two different methods: manual deposition and vacuum drying. For manual deposition, a 10 μl droplet of 2 μg/ml polymers solution in THF was applied at room temperature for 40 seconds on substrate. After the incubation time on the surface, then the sample was rinsed with 1 ml Milli-Q water and dried with a gentle flow of nitrogen gas. For Vacuum drying, a 10 μl droplet of 2 μg/ml polymers solution in THF was applied at room temperature for 3 seconds on substrate under vacuum.

AFM Measurements

Atomic force microscopy (AFM) measurements were performed on a NX10 AFM (Park systems, South Korea) operating in True Non-Contact™ Mode

with a silicon tip PPP-NCSTR (Park systems, nominal spring constant 7.4 Nm^{-1}, nominal tip radii ~7nm). The image was acquired with a tip velocity of 0.8 μm per second. Three map sizes and two pixelization setting were employed: 4×4 μm^2 with 4 nm/px, 1×1 μm^2 and 0.5×0.5 μm^2 with 0.5 nm/px. Image flattening and cross-sectional dimension analysis of single polymers chains were performed by SPIP (Image Metrology, Denmark) software. We initially optimised the deposition of the polymers on three substrates with different charges: positive gold, negative mica, hydrophobic Highly Oriented Pyrolytic Graphite (HOPG) (**Supplementary Fig. 3.8**). HOPG was chosen as a substrate for high-resolution imaging because of its atomically flat surface, favourable interactions with hydrophobic polymers, and similar hydrophobicity as the diamond ATR-FTIR crystal, thus allowing to compare the molecules' behavior on the surface. Each image was first flattened with a first order polynomial fit for the global correction, and then, a zero order least mean square (LMS) fit line-wise correction. Afterwards, the image was further flattened by first and second order LMS fit line-wise correction with area of interest masked.

Acoustical-Mechanical Suppressed AFM-IR

AFM-IR is based on the mechanical detection of the photothermal expansion of a sample when absorbing IR light. To achieve AMS AFM-IR, we leveraged composite foams to suppress any source of mechanical and acoustic noise transmission caused by cables and vibrating parts inside and outside our AFM-IR system, as well as mechanical noise transmission from the ground (**Figure 3.5a**). Adhesive PUR Foam Acoustic Insulation (RS PRO, Netherlands) was applied directly under and on surface of the components of instrument to block the transmission of acoustic vibrations. To shield the controllers from vibrations, we used a double layer of foams: TC2 (EASYfoam, Netherlands) designed for broad-frequency cut-off from 500 Hz to 4 kHz; and PU (EASYfoam, Netherlands), with similar absorption values but with fire and water isolation for safety reasons. For ground noise isolation, we used EASYbond Trillingsisolatie (EASYfoam, Netherlands) with density of 140 kg/m3 to create a floating floor and dampen mechanical vibrations. The noise suppression was quantified on the acquired AFM-IR maps via their RMS noise and the integration of their FFT spectral noise within 0-500 kHz (**Supplementary Fig. 3.13**). In tapping mode, AMS AFM-IR achieved RMS noise level of 25 ± 5 pm to allow imaging single monoatomic steps of HOPG with a height of ~3 Angstroms (**Figure 3.5b**). In contact mode, the AMS suppression led to RMS down to 60 ± 5 pm, against a standard RMS noise of 215 ± 15 pm. To further allow single-molecule localisation with high-accuracy, we stabilised room temperature with variations below 0.1 °C per hour to reduce

AFM thermal drift (**Supplementary Fig. 3.13**).

AFM-IR measurements, maps treatment and analysis

Analysis by AFM-IR was performed with a nanoIR3 (Bruker, USA) on atomically flat HOPG substrates. The substrate roughness and chemical response were also characterized by AFM-IR in the **Supplementary Fig. 3.13**. The root mean square roughness of the AFM maps was measured by SPIP (Image metrology, Denmark). The morphology of the polymer samples was scanned by the nanoIR microscopy system, with a line scan rate within 0.1-0.5 Hz and in contact mode. All AFM maps were acquired with a resolution between 1-30 nm/pixel. A silicon gold coated PR-EX-nIR2 (Bruker, USA) cantilever with a nominal radius of ~30 nm and an elastic constant of about 0.2 N/m was used. The AFM images were treated and analyzed using SPIP software. The height images were corrected using a first order polynomial flattening. All measurements were performed at room temperature under controlled nitrogen atmosphere with relative humidity below 3%. Both spectra and images were acquired by using phase loop (PLL) tracking of contact resonance, the phase was set to zero to the desired resonant frequency around the IR amplitude maximum, and tracked with an integral gain I=0.2 and proportional gain P=1.

3. Supplementary Figures

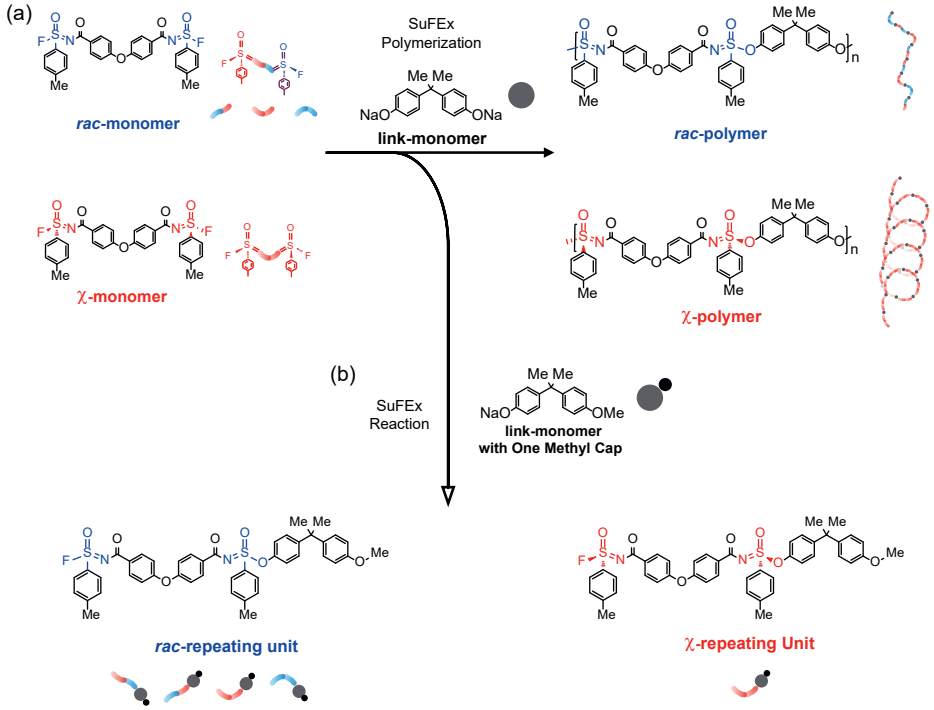

Supplementary Figure 3.1. Schematic Representation of the Reaction Pathways for the Synthesis of rac- or χ- Repeating units and Polymers via SuFEx Reaction. The chemical reaction scheme displays two reactions for the formation of polymers using rac- or χ-bis(iminosulfur oxydifluorides) (di-SFs) monomers. (a) Reaction 1 (top left to top right): SuFEx polymerization of rac- or χ-monomer with link-monomers bis(phenyl ethers) (di-phenolate), resulting in either rac- or χ-polymers, respectively. (b) Reaction 2 (top left to bottom): SuFEx reaction of rac- or χ-monomer with a link-monomer bearing a single methyl cap. This reaction leads to the formation of rac- or χ-repeating units.

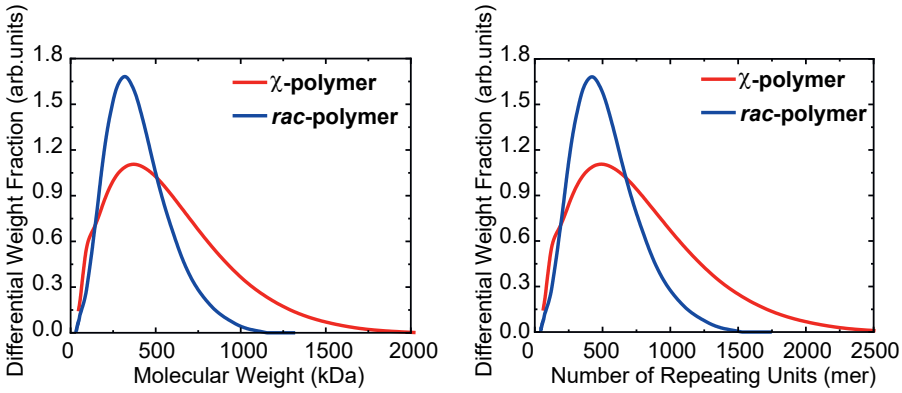

Supplementary Figure 3.2. GPC Chromatography of Polymers. Left: Differential Weight Fraction against Molecular Weight of χ- (Red Curve) and rac- (Blue Curve) polymers. Right: Differential weight fraction against number of repeating units.

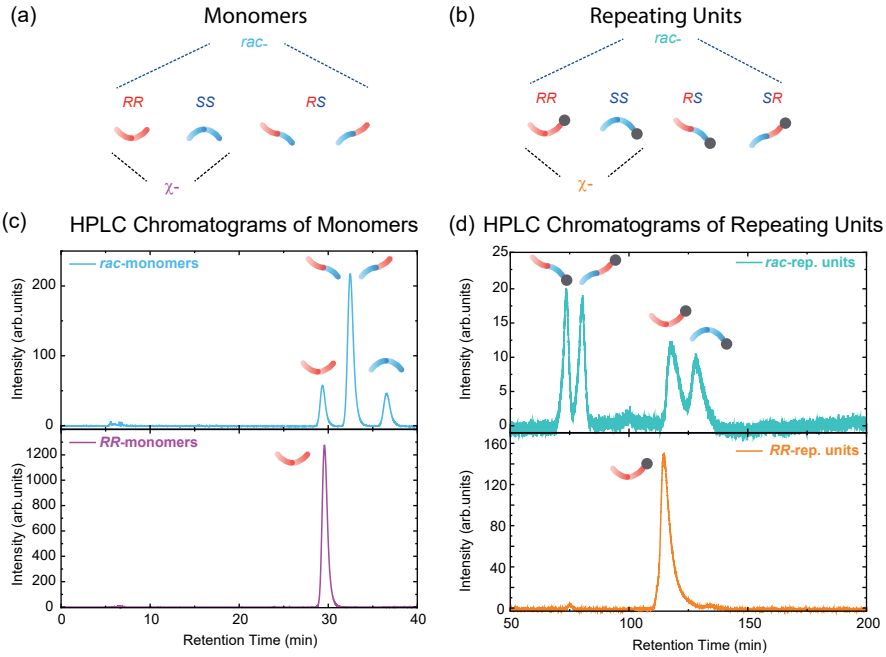

Supplementary Figure 3.3. HPLC Chromatography of Monomers and Repeating units. (a) schematic representations of monomers in different stereochemical forms: RR, RS, and SS.[1] (b) schematic representations of repeating units in different stereochemical forms: RR, SS, RS and SR. (c) HPLC trace for rac-monomers (Light Blue Curve, upper left), with three peaks corresponding to the RR, RS and SS configurations, and χ-monomers (Magenta Curve, bottom left) with RR Configuration. (d) HPLC trace for rac-rep. units (Green Blue Curve, top right), with four peaks corresponding to RS, SR, RR and SS configurations, and χ-repeating units (Orange Curve, bottom right) with RS configuration.[1]

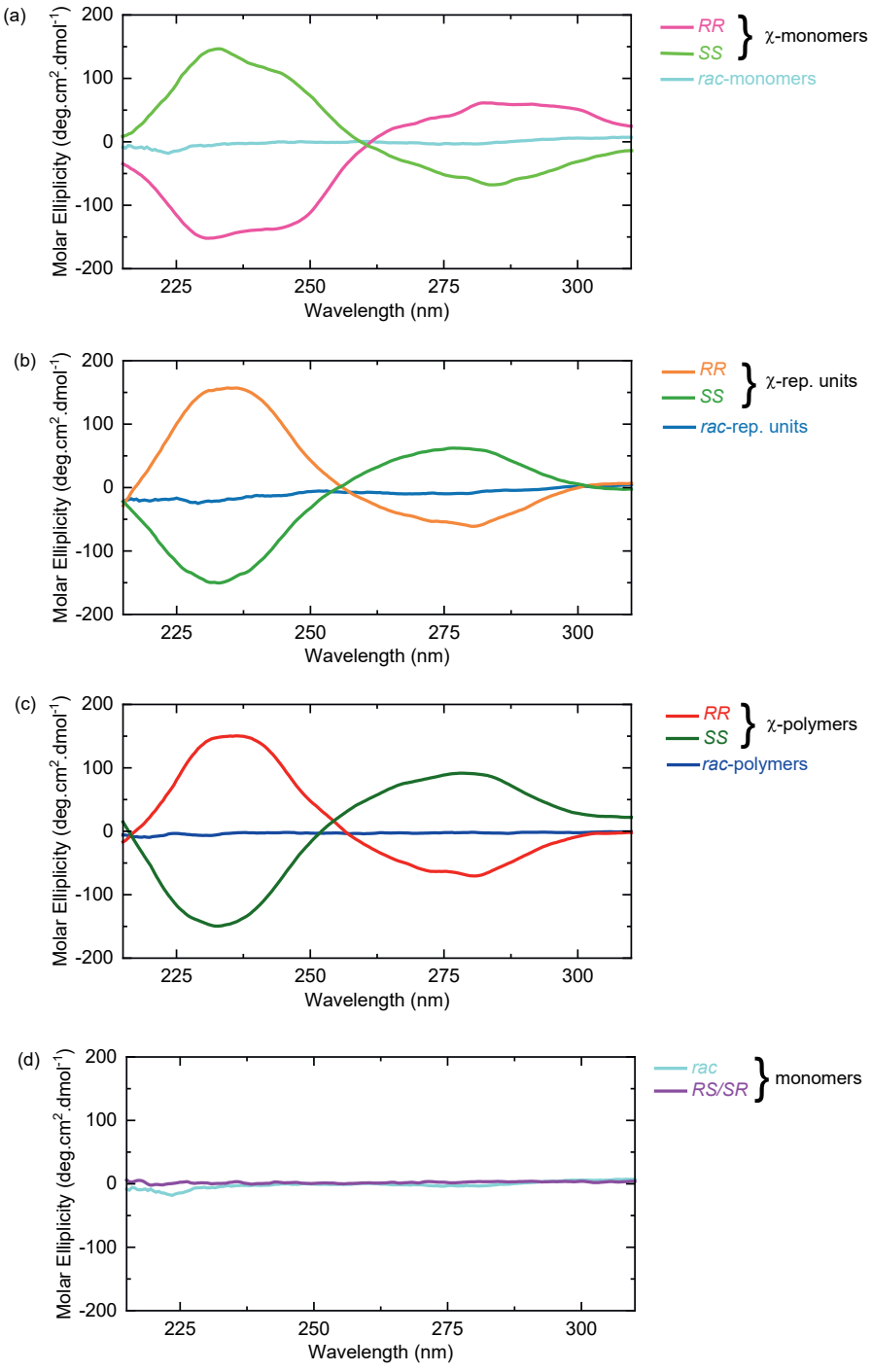
(a)
Molar Ellipticity (deg.cm^2.dmol^{-1})
200
100
0
-100
-200
225
250
275
300
Wavelength (nm)
RR
SS
χ-monomers
rac-monomers
(b)
Molar Ellipticity (deg.cm^2.dmol^{-1})
Wavelength (nm)
RR
SS
χ-rep. units
rac-rep. units
(c)
Molar Ellipticity (deg.cm^2.dmol^{-1})
Wavelength (nm)
RR
SS
χ-polymers
rac-polymers
(d)
Molar Ellipticity (deg.cm^2.dmol^{-1})
Wavelength (nm)
rac
RS/SR
monomers

Supplementary Figure 3.4. CD spectra of monomers, repeating units and polymers. (a) Monomers: rac- (light blue), RR- (magenta) and SS- (light green). (b) Repeating units: rac- (green blue), RR- (orange) and SS- (green). (c) Polymers: rac- (blue), RR- (red) and SS- (dark green). (d) Monomers: rac- (light blue) and RS- (light purple).

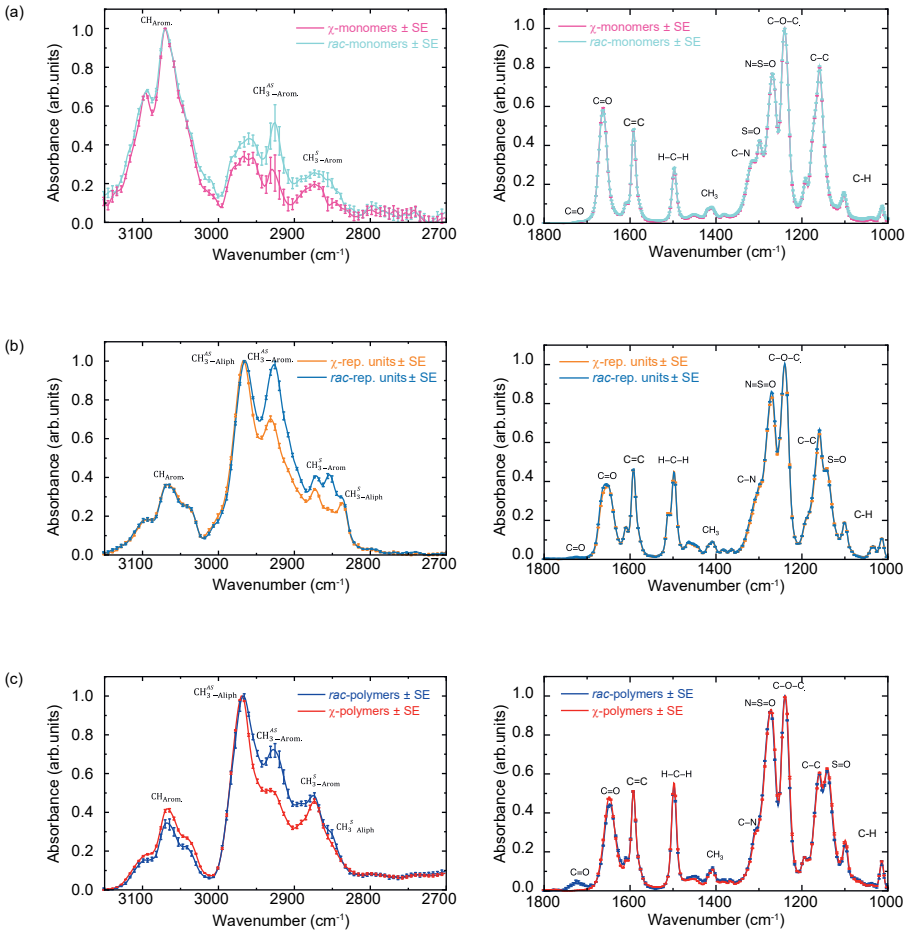

Supplementary Figure 3.5. IR spectra of monomers, repeating units, and polymers, with assignments. (a) Monomers: rac- (light blue, independent experiments N=8, replicates n=20; error bars represent SE) and χ- (magenta, N=8, n=20; error bars represent SE). (b) Repeating units: rac- (green blue, N=8, n=20; error bars represent SE) and χ- (orange, N=8, n=20; error bars represent SE). (c) Polymers: rac- (blue, N=9, n=25; error bars represent SE) and χ- (red, N=9, n=20-25; error bars represent SE).

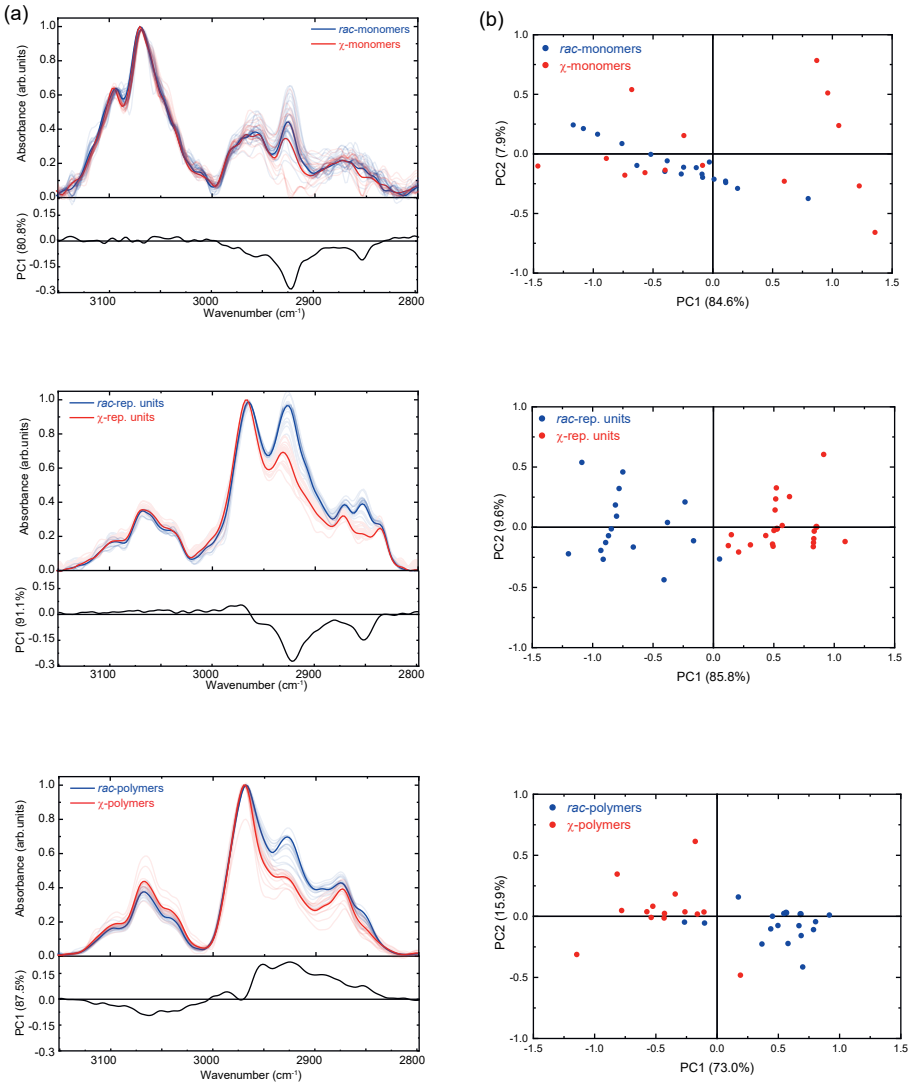

Supplementary Figure 3.6. Principal Component Analysis (PCA) of IR Spectra of Polymers in the methyl region. (a) IR Spectra and loading plots of PC1 in the range from 3150-2800 cm^{-1}: N=8 independent experiments, n=40 replicates, each co-averaging 512 spectra for rac- (blue) and χ- (red) monomers and repeating units; N=9 independent experiments, n=40 spectra, each co-averaging 512 spectra for rac- (blue) and χ- (red) polymers; for all spectra the solid line represents average spectrum, shading represents SE, the semi-transparent lines represent all individual spectra). (b) Score plots of PCA analysis applied to rac- (blue) and χ- (red) monomers, repeating units and polymers.

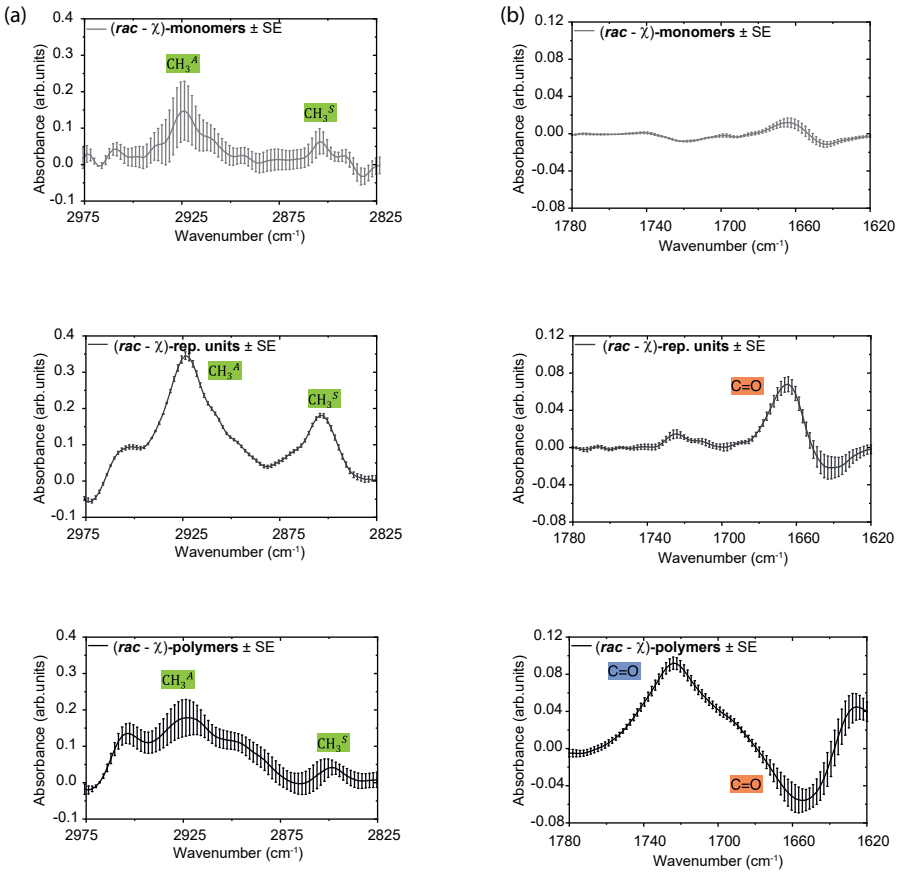

Supplementary Figure 3.7. Difference IR spectroscopy for the χ- vs. rac- polymers. (a) 2975-2825 cm^{-1} and (b) 1780-1620 cm^{-1} with assignments. (a) Top: (rac minus χ)-monomers; Middle: (rac minus χ)-repeating units; Bottom: (rac minus χ)-polymers. (b) Top: (rac minus χ)-monomers; Middle: (rac minus χ)-repeating units; Bottom: (rac minus χ)-polymers. All plotted as average ± error bars representing SE.

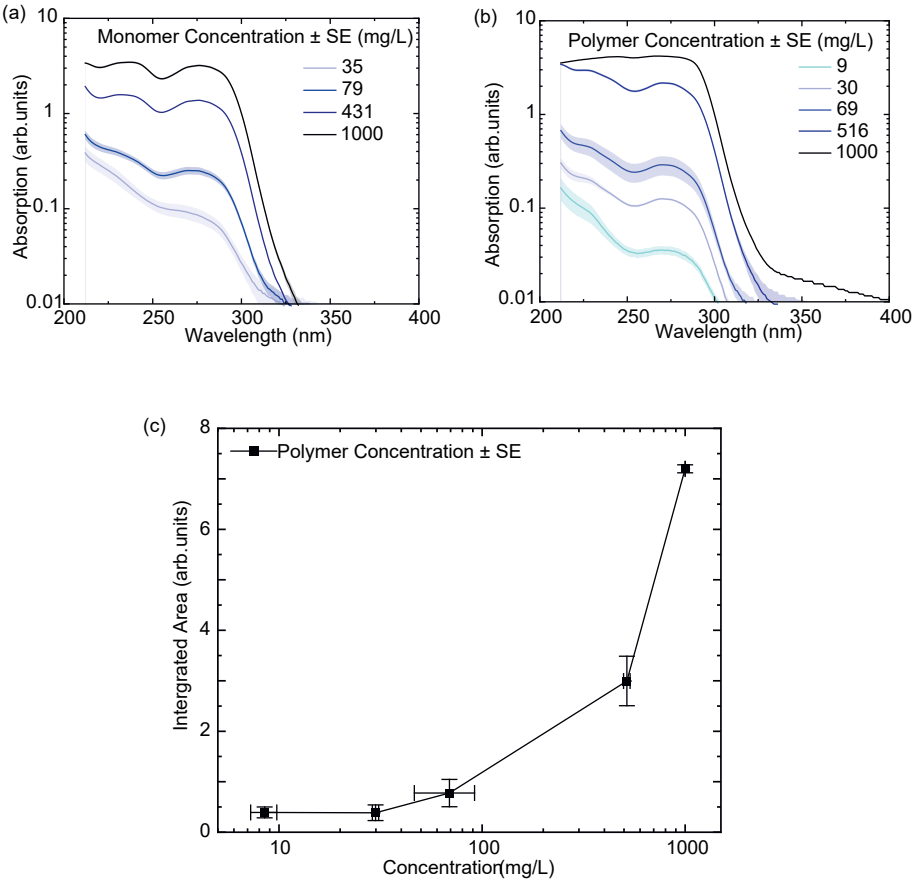

Supplementary Figure 3.8. UV-Vis Spectroscopy of monomers and polymers as a function of concentration in liquid. (a) Absorption spectra of racemic monomers at concentrations of 35, 79, 431, and 1000 mg/L, plotted on a logarithmic scale, the vertical grey line represents the cut-off due to signal saturation (shading represents SE). (b) Absorption spectra of racemic polymers at concentrations of 9, 30, 69, 516, and 1000 mg/L, plotted on a logarithmic scale (shading represents SE). (c) Integrated absorption area between 300-400 nm as a function of polymer concentration, quantifying the concentration-dependent peak broadening and red-shift; error bars represent SE on both concentration (X) and integrated UV-Vis peak area (Y).

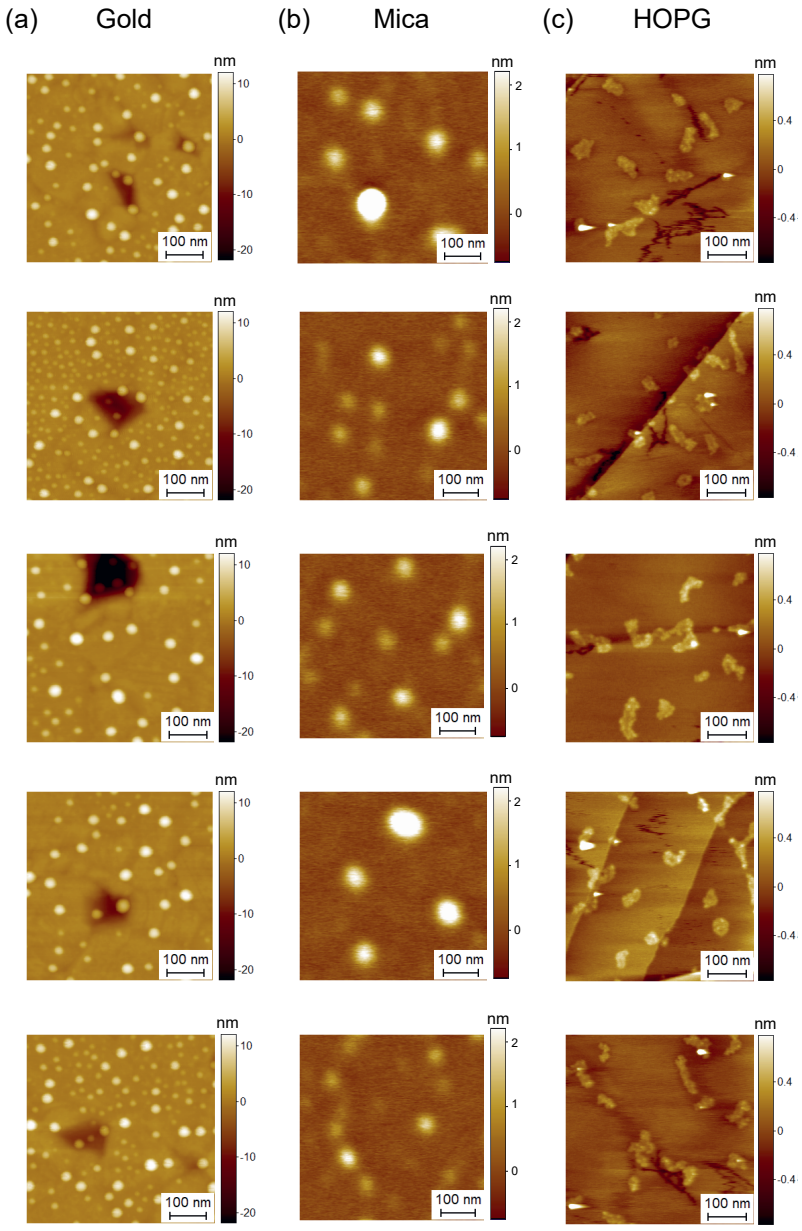

Supplementary Figure 3.9. Representative AFM Morphological Maps of χ-Polymers on Different Substrates at 2ug/mL concentration. (a) Positive charged gold. (b) Negative charged muscovite mica. (c) Hydrophobic Highly Ordered Pyrolytic Graphite (HOPG). Several areas were randomly imaged across the sample's surface (n=5) to account for possible heterogeneity.

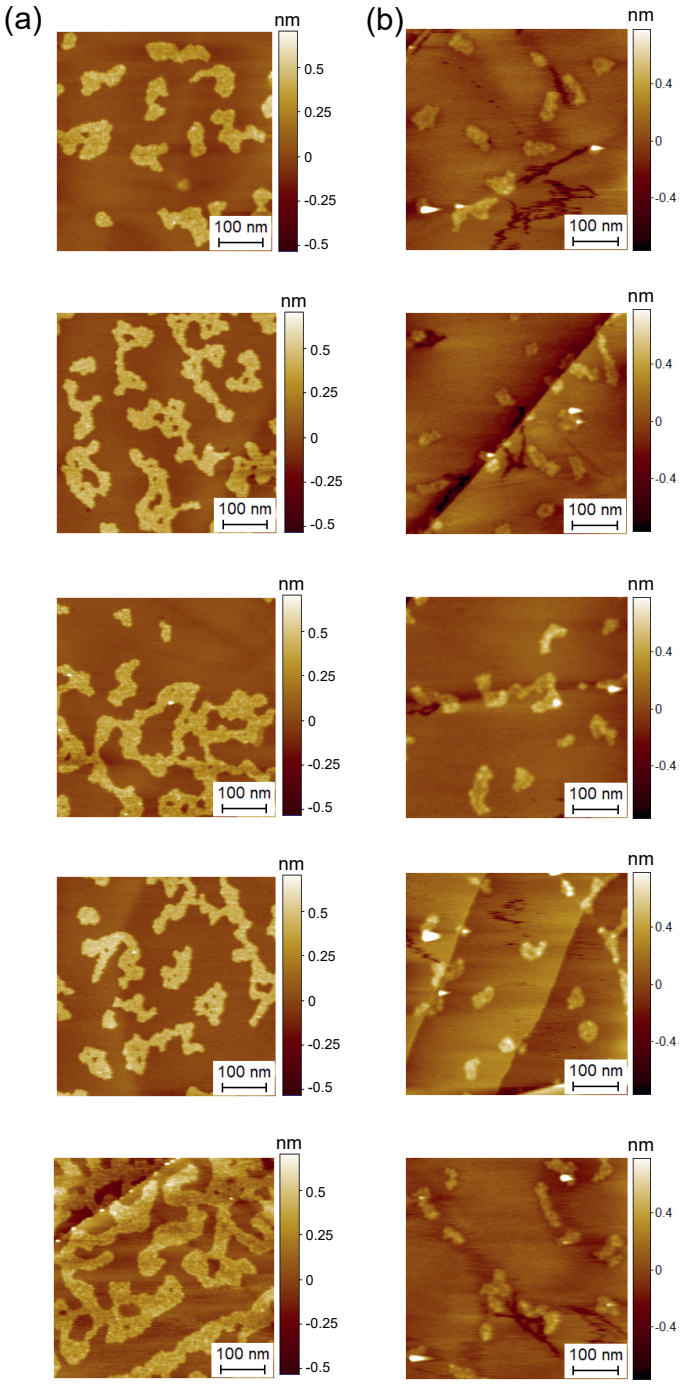

Supplementary Figure 3.10. Comparison of Representative AFM Morphological Maps at 2ug/mL concentration of (a) rac-polymers. (b) χ-polymers on HOPG.

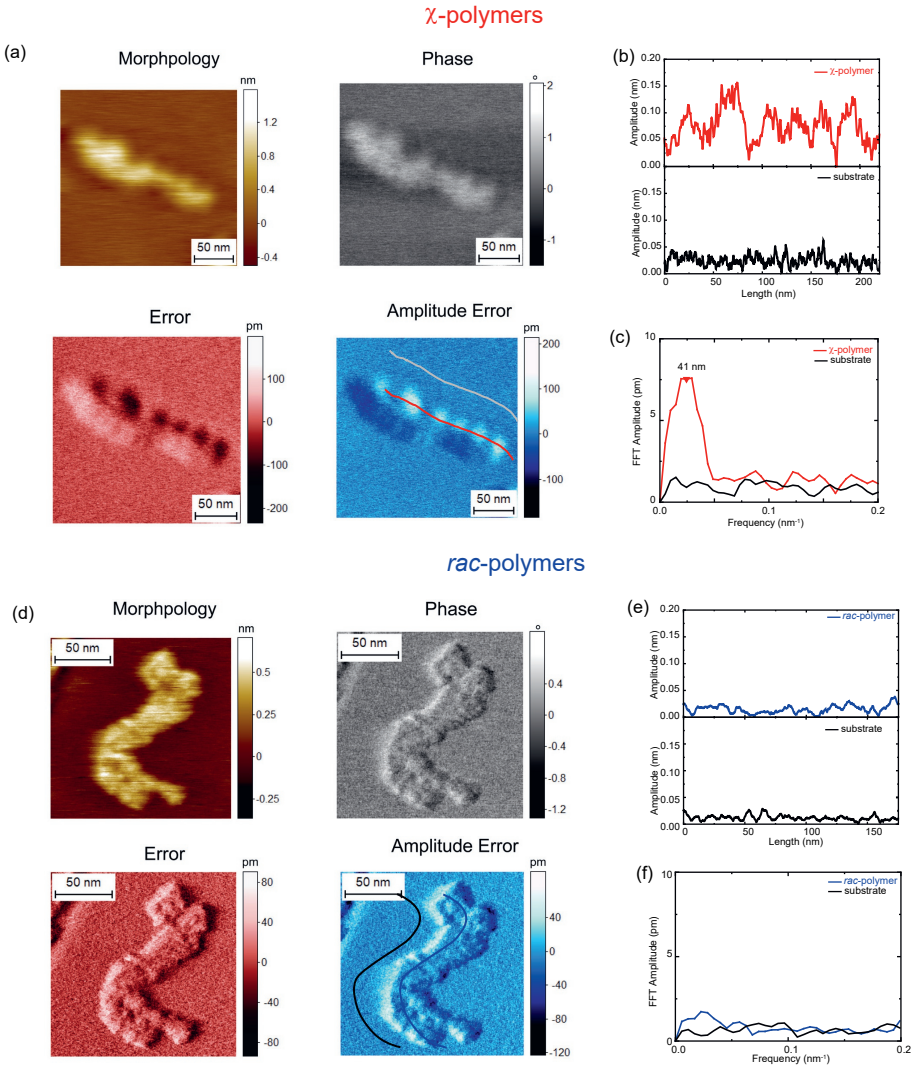

Supplementary Figure 3.11. Analysis of Helicity of Rac- and χ-polymers at Angstrom Resolution. AFM data channels of a representative (a) single χ-polymers chain and (b) cross-sectional profile of the single polymer chain(s) and substrate on the Amplitude Error channel. (c) FFT power spectrum of the line-profile of the single polymer chain(s) and substrate. (d) Rac-polymers chains at angstrom resolution. (e) Cross-sectional profile of the single polymer chain(s) and substrate on the Amplitude Error channel. (f) FFT power spectrum of the line-profile of the single polymer chain(s) and substrate.

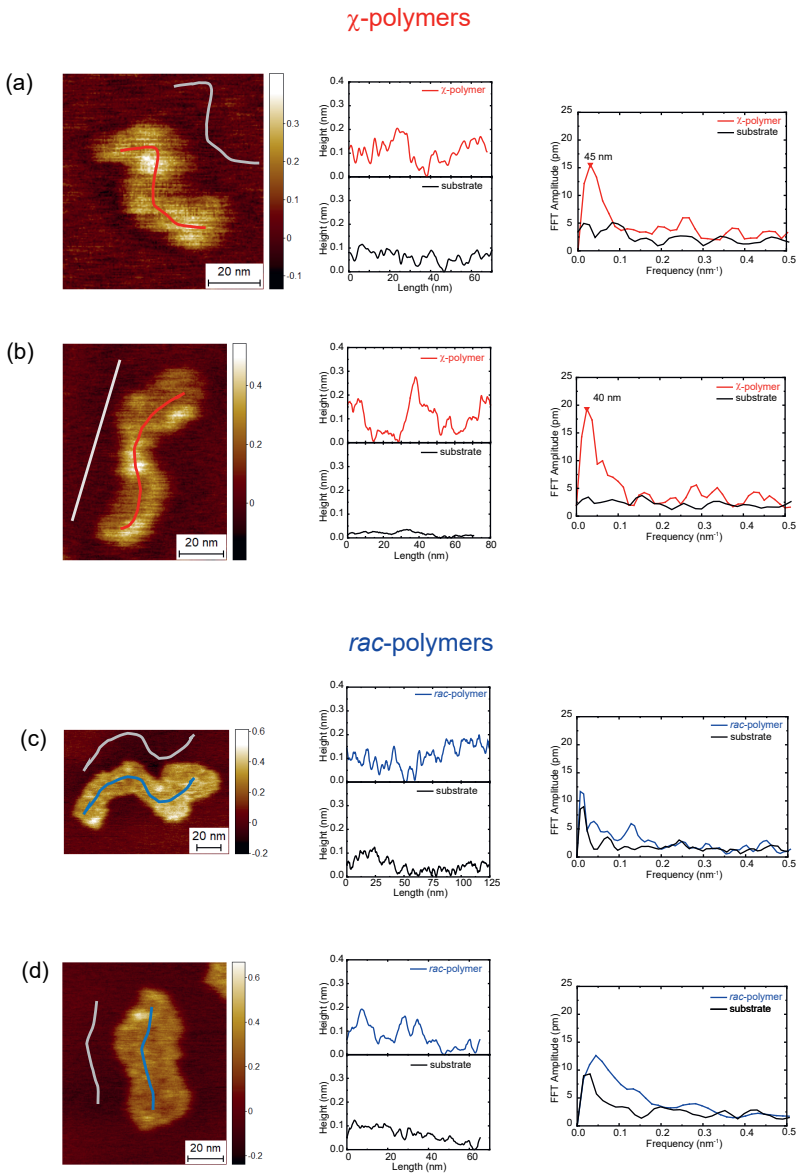

Supplementary Figure 3.12. Analysis of Periodicity of other rac- and χ-polymers on conventional AFM maps. (a)(b) Left: Morphological map of a representative single χ-polymer chain. Middle: Cross-sectional profile of the single polymer chain and substrate. Right: FFT power spectrum of the line-profile of the single polymer chain and substrate. (c)(d) Left: Morphological map of a representative single rac-polymer chains. Middle: Cross-sectional profile of the single rac-polymer chains and substrate. Right: FFT power spectrum of the line-profile of the single rac-polymer chains and substrate.

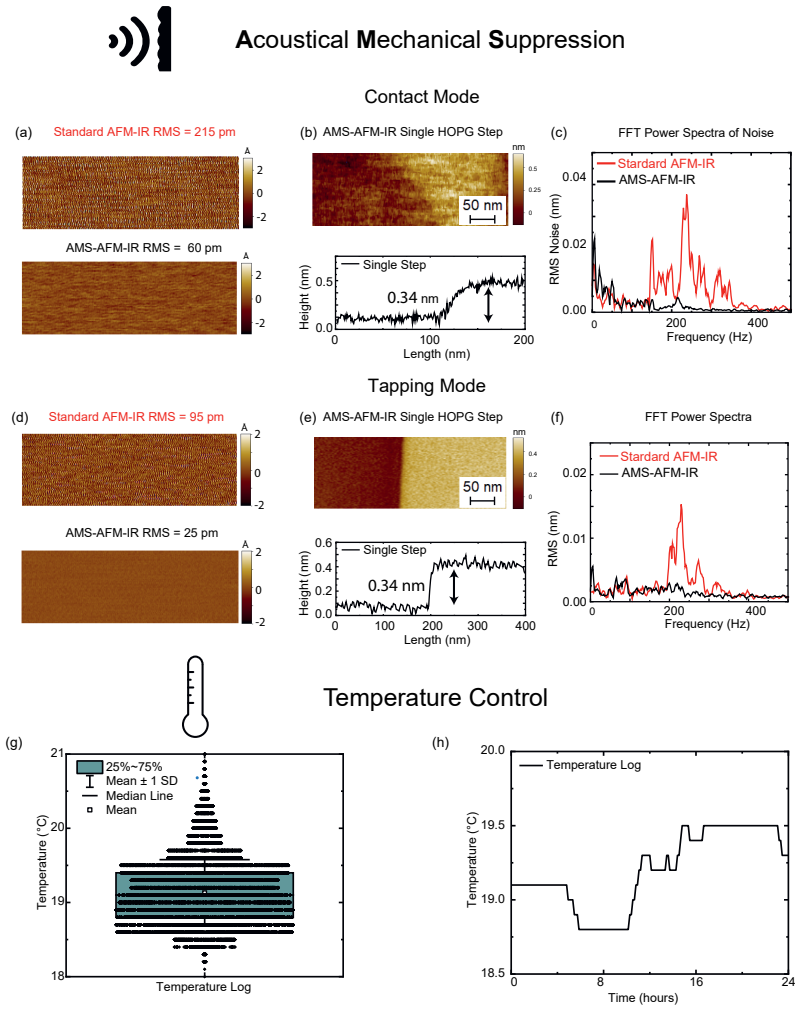

Supplementary Figure 3.13. AFM-IR Noise Level Comparison Before and After Acoustical Mechanical Suppression (AMS) and Temperature Stability of AFM-IR. (a) Morphological map of the bare HOPG substrate in contact mode, before and after AMS. (b) Morphological map of a single HOPG step and line profile of the step. (c) FFT power spectra of noise contribution before and after AMS. (d) Morphological map of the bare HOPG substrate in tapping mode, before and after AMS. (e) Morphological map of a single HOPG step and line profile of the step. (f) FFT power spectra of noise contribution before and after AMS. (g) Box plot showing the distribution of the temperature log, encapsulating the median, interquartile range (25th to 75th percentile), and mean with an indication of standard deviation (±0.5°C). (h) Typical temperature log upon 24 hours measurements. Of note, "standard AFM-IR" RMS indicates the noise of measurements where both AFM and IR components (laser controllers, chillers) are turned on to perform measurements.

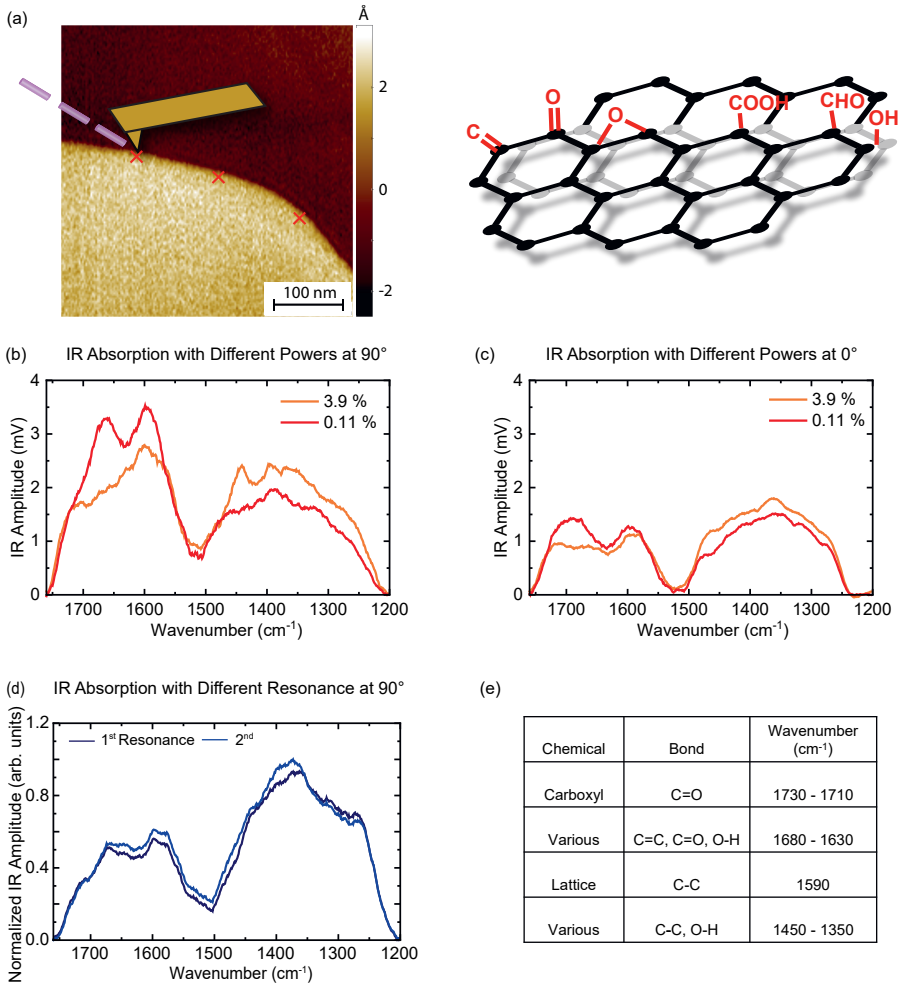

Chemical	Bond	Wavenumber (cm^{-1})
Carboxyl	C=O	1730 - 1710
Various	C=C, C=O, O-H	1680 - 1630
Lattice	C-C	1590
Various	C-C, O-H	1450 - 1350

Supplementary Figure 3.14. Determination of Substrate IR Absorption in Contact Mode for HOPG. (a) Left: AFM map of a single atomical step. Right: Illustration of chemical environment around the step. (b) IR absorption of HOPG at the second resonance under perpendicular polarization with respect to the surface, for varying laser power levels. (c) IR absorption of HOPG at the second resonance under parallel polarization with respect to the surface, for varying laser power levels. (d) IR absorption of HOPG at 12.5% laser power under perpendicular polarization with respect to the surface, for different resonance frequencies. (e) Assignments of HOPG IR absorption peaks.

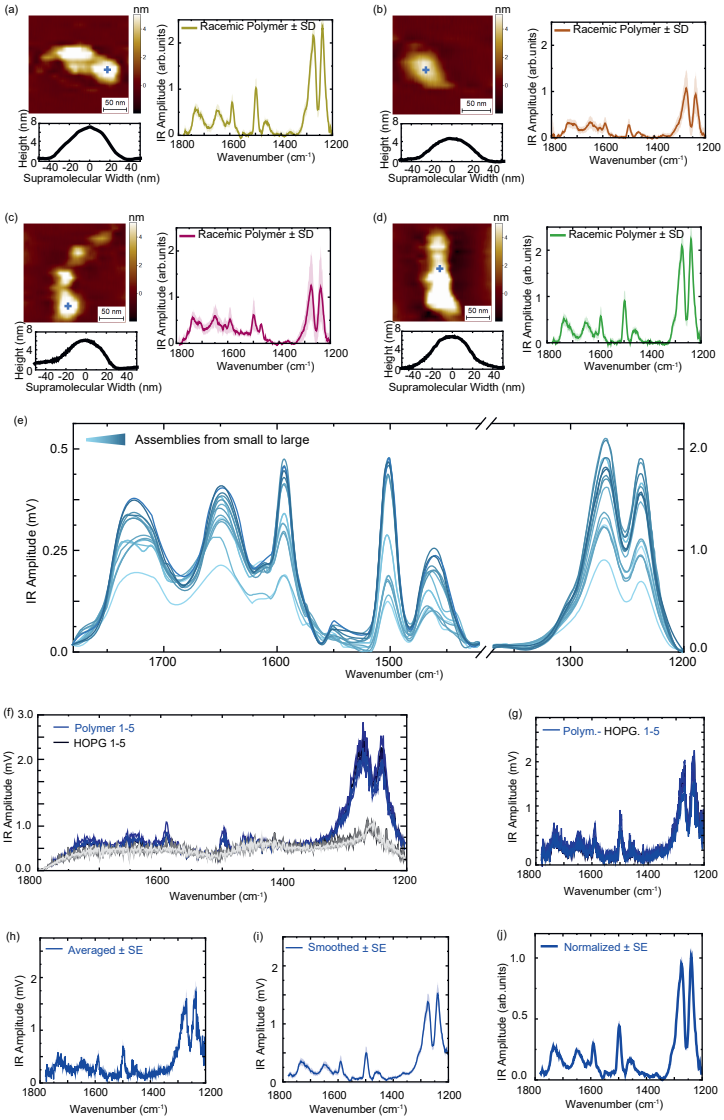

Supplementary Figure 3.15. AFM-IR Spectra of Different Assemblies and Spectra Analysis Procedure for rac-Polymers. (a-d) AFM-IR morphology, cross-sectional profile and spectra of different assemblies of rac-Polymers; average spectra, with shading representing SD. (e) Spectra of all assemblies ranking from smallest (light blue) to largest (dark blue) height, n=18. (f) Unprocessed HOPG substrate spectra and representative polymer spectra. (g) Subtracted polymer spectra. (h) Mean of the ratioed spectra with shading representing SE. (i) Smoothed spectra using a 15-point, 2nd order Savitzky-Golay filter with shading representing SE. (j) Final normalized spectra within the range [0,1] with shading representing SE.

4. References

1 Liu, M., Zhang, L. & Wang, T. Supramolecular Chirality in Self-Assembled Systems. *Chem. Rev.* **115**, 7304-7397 (2015). https://doi.org:10.1021/cr500671p

2 Adawy, A. Functional Chirality: From Small Molecules to Supramolecular Assemblies. *Symmetry* **14**, 292 (2022). https://doi.org:10.3390/sym14020292

3 Sessler, J. L., Lawrence, C. M. & Jayawickramarajah, J. Molecular recognition via base-pairing. *Chem. Soc. Rev.* **36**, 314-325 (2007). https://doi.org:10.1039/B604119C

4 Geider, K. & Hoffmannberling, H. Proteins Controlling The Helical Structure of DNA. *Annu. Rev. Biochem.* **50**, 233-260 (1981). https://doi.org:10.1146/annurev.bi.50.070181.001313

5 William F. DeGrado, a., Summa, C. M., Vincenzo Pavone, Flavia Nastri, a. & Lombardi, A. De Novo Design and Structural Characterization of Proteins and Metalloproteins. *Annu. Rev. Biochem.* **68**, 779-819 (1999). https://doi.org:10.1146/annurev.biochem.68.1.779

6 Xia, X. *et al.* Material Choice and Structure Design of Flexible Battery Electrode. *Adv. Sci.* **10**, 2204875 (2023). https://doi.org:https://doi.org/10.1002/advs.202204875

7 Zhang, L., Wang, H.-X., Li, S. & Liu, M. Supramolecular chiroptical switches. *Chem. Soc. Rev.* **49**, 9095-9120 (2020). https://doi.org:10.1039/d0cs00191k

8 Pop, F., Zigon, N. & Avarvari, N. Main-Group-Based Electro- and Photoactive Chiral Materials. *Chem. Rev.* **119**, 8435-8478 (2019). https://doi.org:10.1021/acs.chemrev.8b00770

9 Buhse, T. *et al.* Spontaneous Deracemizations. *Chem. Rev.* **121**, 2147-2229 (2021). https://doi.org:10.1021/acs.chemrev.0c00819

10 Ikai, T., Kurake, T., Okuda, S., Maeda, K. & Yashima, E. Racemic Monomer-Based One-Handed Helical Polymer Recognizes Enantiomers through Auto-Evolution of Its Helical Handedness Excess. *Angew. Chem. Int. Ed.* **60**, 4625-4632 (2021). https://doi.org:https://doi.org/10.1002/anie.202014946

11 Li, P., Gao, H., Zhao, B. & Deng, J. Enantioselective Induction, Amplification, and Storage of Helical Chirality in Absolutely Achiral Polymer Systems. *Chem. Mater.* **34**, 7503-7515 (2022). https://doi.org:10.1021/acs.chemmater.2c01783

12 Zha, X. *et al.* Modulating the Macroscopic Helicity of Poly(m-phenylenediamine) by Achiral Monomer Copolymerization. *Adv. Func. Mater.* **33**, 2211956 (2023). https://doi.org:https://doi.org/10.1002/adfm.202211956

13 Wang, H. F. *et al.* Generalizing the effects of chirality on block copolymer assembly. *Proc. Natl. Acad. Sci. U.S.A.* **116**, 4080-4089 (2019). https://doi.org:10.1073/pnas.1812356116

14 Hall, V., Sklepari, M. & Rodger, A. Protein Secondary Structure Prediction from Circular Dichroism Spectra Using a Self-Organizing Map with Concentration Correction. *Chirality* **26**, 471-482 (2014). https://doi.org:https://doi.org/10.1002/chir.22338

15 Barth, A. Infrared spectroscopy of proteins. *Biochim. Biophys. Acta* **1767**, 1073-1101 (2007). https://doi.org:10.1016/j.bbabio.2007.06.004

16 Kurouski, D. Advances of Vibrational Circular Dichroism (VCD) in bioanalytical chemistry. A review. *Anal. Chim. Acta* **990**, 54-66 (2017). https://doi.org:https://doi.org/10.1016/j.aca.2017.08.014

17 Ruggeri, F. S. *et al.* Infrared nanospectroscopy characterization of oligomeric and fibrillar aggregates during amyloid formation. *Nat. Commun.* **6**, 7831 (2015). https://doi.org:10.1038/ncomms8831

18 Li, S. *et al.* SuFExable polymers with helical structures derived from thionyl tetrafluoride. *Nat. Chem.* **13**, 858-867 (2021). https://doi.org:10.1038/s41557-021-00726-x

19 Schwartz, J. J., Jakob, D. S. & Centrone, A. A guide to nanoscale IR spectroscopy: resonance enhanced transduction in contact and tapping mode AFM-IR. *Chem. Soc. Rev.* **51**, 5248-5267 (2022). https://doi.org:10.1039/D2CS00095D

20 Wang, F., Gnewou, O., Solemanifar, A., Conticello, V. P. & Egelman, E. H. Cryo-EM of Helical Polymers. *Chem. Rev.* (2022). https://doi.org:10.1021/acs.chemrev.1c00753

21 Egelman, E. H. & Wang, F. Cryo-EM is a powerful tool, but helical applications can have pitfalls. *Soft Matter* **17**, 3291-3293 (2021). https://doi.org:10.1039/D1SM00282A

22 Kumaki, J., Sakurai, S.-I. & Yashima, E. Visualization of synthetic helical polymers by high-resolution atomic force microscopy. *Chem. Soc. Rev.* **38**, 737 (2009). https://doi.org:10.1039/b718433f

23 Liu, Y. & Vancso, G. J. Polymer single chain imaging, molecular forces, and nanoscale processes by Atomic Force Microscopy: The ultimate proof of the macromolecular hypothesis. *Prog. Polym. Sci.* **104** (2020). https://doi.org:10.1016/j.progpolymsci.2020.101232

24 Kurouski, D., Deckert-Gaudig, T., Deckert, V. & Lednev, I. K. Structure and Composition of Insulin Fibril Surfaces Probed by TERS. *J. Am. Chem. Soc.* **134**, 13323-13329 (2012). https://doi.org:10.1021/ja303263y

25 Lee, J., Crampton, K. T., Tallarida, N. & Apkarian, V. A. Visualizing vibrational normal modes of a single molecule with atomically confined light. *Nature* **568**, 78-82 (2019). https://doi.org:10.1038/s41586-019-1059-9

26 Shao, F. *et al.* In-situ nanospectroscopic imaging of plasmon-induced two-dimensional [4+4]-cycloaddition polymerization on Au(111). *Nat. Commun.* **12**, 4557 (2021). https://doi.org:10.1038/s41467-021-24856-5

27 Mrđenović, D. *et al.* Visualizing Surface Phase Separation in PS-PMMA Polymer Blends at the Nanoscale. *ACS Appl. Mater. Interf.* **14**, 24938-24945 (2022). https://doi.org:10.1021/acsami.2c03857

28 Mrđenović, D. *et al.* Nanoscale chemical analysis of 2D molecular materials using tip-enhanced Raman spectroscopy. *Nanoscale* **15**, 963-974 (2023). https://doi.org:10.1039/D2NR05127C

29 Centrone, A. Infrared Imaging and Spectroscopy Beyond the Diffraction Limit. *Annu. Rev. Anal. Chem.* **8**, 101-126 (2015). https://doi.org:10.1146/annurev-anchem-071114-040435

30 Kurouski, D., Dazzi, A., Zenobi, R. & Centrone, A. Infrared and Raman chemical imaging and spectroscopy at the nanoscale. *Chem. Soc. Rev.* **49**, 3315-3347 (2020). https://doi.org:10.1039/c8cs00916c

31 Ruggeri, F. S., Mannini, B., Schmid, R., Vendruscolo, M. & Knowles, T. P. J. Single molecule secondary structure determination of proteins through infrared absorption nanospectroscopy. *Nat. Commun.* **11**, 2945 (2020). https://doi.org:10.1038/s41467-020-16728-1

32 Jin, M. & Belkin, M. A. Infrared Vibrational Spectroscopy of Functionalized Atomic Force Microscope Probes using Resonantly Enhanced Infrared Photoexpansion Nanospectroscopy. *Small Methods* **3**, 1900018 (2019). https://doi.org:10.1002/smtd.201900018

33 Tseng, Y.-H. *et al.* Photoinduced Alignment under Solvent Vapor Annealing (PA-SVA): Enhanced Ordering and Patterning in Block Copolymer Films. *ACS Appl. Polym. Mater.* **4**, 8536-8542 (2022). https://doi.org:10.1021/acsapm.2c01453

34 Prine, N. *et al.* Enabling quantitative analysis of complex polymer blends by infrared nanospectroscopy and isotopic deuteration. *Nanoscale* **15**, 7365-7373 (2023). https://doi.org:10.1039/D3NR00886J

35 Liang, D.-D., Pujari, S. P., Subramaniam, M., Besten, M. & Zuilhof, H. Configurationally Chiral SuFEx-Based Polymers. *Angew. Chem. Int. Ed.* **61**, e202116158 (2022). https://doi.org:https://doi.org/10.1002/anie.202116158

36 Li, S. *et al.* SuFExable polymers with helical structures derived from thionyl tetrafluoride. *Nat. Chem.* **13**, 858-867 (2021). https://doi.org:10.1038/

s41557-021-00726-x

37 Ruggeri, F. S. *et al.* Nanoscale studies link amyloid maturity with polyglutamine diseases onset. *Sci. Rep.* **6**, 31155 (2016). https://doi.org:10.1038/srep31155

38 Korolkov, V. V. *et al.* Ultra-high resolution imaging of thin films and single strands of polythiophene using atomic force microscopy. *Nat. Commun.* **10**, 1537 (2019). https://doi.org:10.1038/s41467-019-09571-6

39 Shen, J. & Okamoto, Y. Efficient Separation of Enantiomers Using Stereoregular Chiral Polymers. *Chem. Rev.* **116**, 1094-1138 (2016). https://doi.org:10.1021/acs.chemrev.5b00317

40 Ranjbar, B. & Gill, P. Circular dichroism techniques: biomolecular and nanostructural analyses- a review. *Chem. Biol. Drug Des.* **74**, 101-120 (2009). https://doi.org:10.1111/j.1747-0285.2009.00847.x

41 Bulheller, B. M., Rodger, A. & Hirst, J. D. Circular and linear dichroism of proteins. *Phys. Chem. Chem. Phys.* **9**, 2020-2035 (2007). https://doi.org:10.1039/b615870f

42 Kane-Maguire, L. A. P. & Wallace, G. G. Chiral conducting polymers. *Chem. Soc. Rev.* **39**, 2545-2576 (2010). https://doi.org:10.1039/b908001p

43 Nakano, T., Pietropaolo, A. & Kamata, M. Chirality analysis of helical polymers. *Chem. Teach. Int.* **3**, 131-140 (2021). https://doi.org:10.1515/cti-2020-0009

44 Nakano, T. & Okamoto, Y. Synthetic helical polymers: Conformation and function. *Chem. Rev.* **101**, 4013-4038 (2001). https://doi.org:10.1021/cr0000978

45 Leigh, T. & Fernandez-Trillo, P. Helical polymers for biological and medical applications. *Nat. Rev. Chem.* **4**, 291-310 (2020). https://doi.org:10.1038/s41570-020-0180-5

46 Osman, Z. & Arof, A. K. FTIR studies of chitosan acetate based polymer electrolytes. *Electrochim. Acta* **48**, 993-999 (2003). https://doi.org:https://doi.org/10.1016/S0013-4686(02)00812-5

47 Wu, L. C. *et al.* A charge density study of π-delocalization and intermolecular interactions. *Phys. Chem. Chem. Phys.* **17**, 14177-14184 (2015). https://doi.org:10.1039/C5CP01575H

48 Dharmarwardana, M. *et al.* Strong π-stacking causes unusually large anisotropic thermal expansion and thermochromism. *Proc. Natl. Acad. Sci. U.S.A.* **118**, e2106572118 (2021). https://doi.org:doi:10.1073/pnas.2106572118

49 Kenkel, S., Mittal, S. & Bhargava, R. Closed-loop atomic force microscopy-infrared spectroscopic imaging for nanoscale molecular characterization. *Nat. Commun.* **11**, 3225 (2020). https://doi.org:10.1038/s41467-020-17043-5

50 Marinello, F., Balcon, M., Carmignato, S. & Savio, E. Long term thermal drift study on SPM scanners. *Mechatronics* **21**, 1272-1278 (2011). https://doi.org:https://doi.org/10.1016/j.mechatronics.2011.07.002

51 Hirata, S., Shigeta, Y., Xantheas, S. S. & Bartlett, R. J. Helical Organic and Inorganic Polymers. *J. Phys. Chem. B* **127**, 3556-3583 (2023). https://doi.org:10.1021/acs.jpcb.3c00620

52 Rohmer, M., Freudenberg, J. & Binder, W. H. Secondary Structures in Synthetic Poly(Amino Acids): Homo- and Copolymers of Poly(Aib), Poly(Glu), and Poly(Asp). *Macrom. Biosci.* **23**, 2200344 (2023). https://doi.org:https://doi.org/10.1002/mabi.202200344

53 Watson, J. L. *et al.* De novo design of protein structure and function with RFdiffusion. *Nature* **620**, 1089-1100 (2023). https://doi.org:10.1038/s41586-023-06415-8

54 Liang, D.-D. *et al.* Silicon-Free SuFEx Reactions of Sulfonimidoyl Fluorides: Scope, Enantioselectivity, and Mechanism. *Angew. Chem. Int. Ed.* 59, 7494-7500 (2020). https://doi.org:https://doi.org/10.1002/anie.201915519

Chapter 4

Nano-Chemical Analysis of Intermolecular Interactions in Self-assembled Monolayers

This chapter is adapted from: **Xuecong Li**, Samuel Visser Bravo, Sidharam P. Pujari, Jasper van der Gucht, Han Zuilhof*, Francesco Simone Ruggeri* Nano-Chemical Analysis of Intermolecular Interactions in Self-assembled Monolayers submitted to *Communications Chemistry*.

ABSTRACT

Self-assembled monolayers are governed by a competition between substrate–adsorbate interaction and adsorbate-adsorbate intermolecular interactions, yet direct monolayer-level readouts of this balance remain scarce. Here, ultra-sensitive photothermal infrared nanospectroscopy (AFM-IR) empowers to probe at sub-nanometer scale the intermolecular interactions involved in the self-assembly of monolayers formed by click-chemistry-based monomers and polymers. We prove that monomers adsorb on highly ordered pyrolytic graphite to yield a coverage-invariant monolayer, whereas polymers form a cooperative monolayer dominated by adsorbate-adsorbate intermolecular π–π stacking. For the polymer self-assembled monolayer, this difference is evidenced by a coverage-dependent increase in height, an emergent carbonyl band at ~1725 cm^{-1}, and a pronounced rise in water contact angle. These findings establish AFM-IR as a key tool to unravel the chemical principles of surface-driven self-assembly mechanisms, providing key information for the design of robust, tunable cooperative self-assembled monolayers for advanced surface functionalization.

4.1 Introduction

Self-assembled monolayers (SAMs) are critical in surface functionalization,[1, 2] enabling precise molecular-scale engineering for applications in catalysis,[3] electronics,[4] and biosensing.[5] These ordered assemblies form spontaneously on substrates, through a balance of substrate-adsorbate interactions (e.g. chemisorption,[6] physisorption)[7] and intermolecular interactions (e.g. Van der Waals interactions,[8] hydrogen bonding,[9] and π-π stacking).[10] Despite extensive study of substrate effects (e.g. surface charge and hydrophobicity), the contribution of adsorbate-adsorbate intermolecular interactions to SAM formation, morphology and functionality, remains yet unclear.[11, 12]

Polymer-based SAMs further deepen this knowledge gap.[13] Compared to monomeric assemblies, polymer SAMs introduce additional complexity through their conformational flexibility, multiple binding sites, diverse functional groups and quasi-2D confinement.[13, 14] These properties promote formation of highly ordered or hierarchical structures, but complicate the interplay between substrate–adsorbate and adsorbate–adsorbate interactions, altering domain formation and long-range patterns.[15] Thus, the key for understanding polymer self-assembly requires deconvoluting intermolecular interactions among adsorbates from substrate-adsorbate adsorption.[15-17]

Conventional spectroscopic and microscopic approaches, such as atomic force microscopy (AFM) and infrared (IR) spectroscopy, have provided important insight into SAM morphology and chemical structure.[13, 18] However, these techniques separately prevent to directly probe how intermolecular forces influence local conformations and supramolecular order during self-assembly of the monolayer.[19] Recent advances in AFM-based photothermal infrared nanospectroscopy (AFM-IR) allow to address this limitation, enabling nano-chemical imaging and spectroscopy of individual molecules and polymer chains on any surface.[20, 21] Combining nano-chemical analysis with 3D morphological imaging enables the direct correlation of the local molecular environment with intermolecular interactions, thereby providing a powerful approach to elucidate how intermolecular interactions govern the organization of self-assembled monolayers.

In this work, we leverage ultra-sensitive, acoustic-mechanical suppressed (AMS) AFM-IR[21] to directly probe the molecular driving forces underlying the

self-assembly into SAMs of monomers and the resulting polymers, formed via sulfur fluoride exchange (SuFEx)-based polymerization.[22] Our SuFEx system provides a modular and sustainable platform with tunable functional groups, making it an ideal model to disentangle the relative contributions of intermolecular interactions. By nano-imaging and chemical analysis, we demonstrate how polymers and their monomeric units exhibit distinct assembly behaviors on surfaces. This innovative approach allows answering long-standing knowledge gaps in how intermolecular interactions govern SAM formation, to guide the rational engineering of functional surfaces for applications in health care, electronics, and energy sectors.[4, 11, 23, 24]

4.2 Results

4.2.1 Model system for resolving intermolecular interactions in SAMs

We first established a framework to distinguish between monomeric and polymeric adsorbates on a substrate, to further elucidate the role of intermolecular interactions in their self-assembly into a monolayer (**Figure 4.1**). **Figure 4.1a** schematically depicts monomer–surface interactions, highlighting key classes of molecular interactions possible (ionic, covalent, Van der Waals), which together with adsorbate-adsorbate intermolecular interactions define the organization of the monolayer formed at high concentrations. The SuFEx monomers used here were synthesized by coupling a disulfonimidoyl fluoride with a mono-protected di-phenol, followed by chromatographic purification,[21, 22] while the polymer was produced by reacting this disulfuonimidoyl fluoride with an unprotected diphenol (**Figure 4.1b**, **Methods**). The monomers and polymers were then characterized by Nuclear Magnetic Resonance (NMR) and high-resolution mass-spectroscopy (HRMS) to ensure their identity, and by high-performance liquid-chromatography (HPLC) for their purity (**Methods**). Polymerization of SuFEx monomers into polymers introduced conformational flexibility and multiple interaction sites to the formed polymers. This conformational difference in turn may fundamentally alter the balance between adsorbate–substrate and adsorbate-adsorbate molecular interactions, leading to distinct self-assembly pathways of SAM formation for polymers compared to monomers (**Figure 4.1b**).

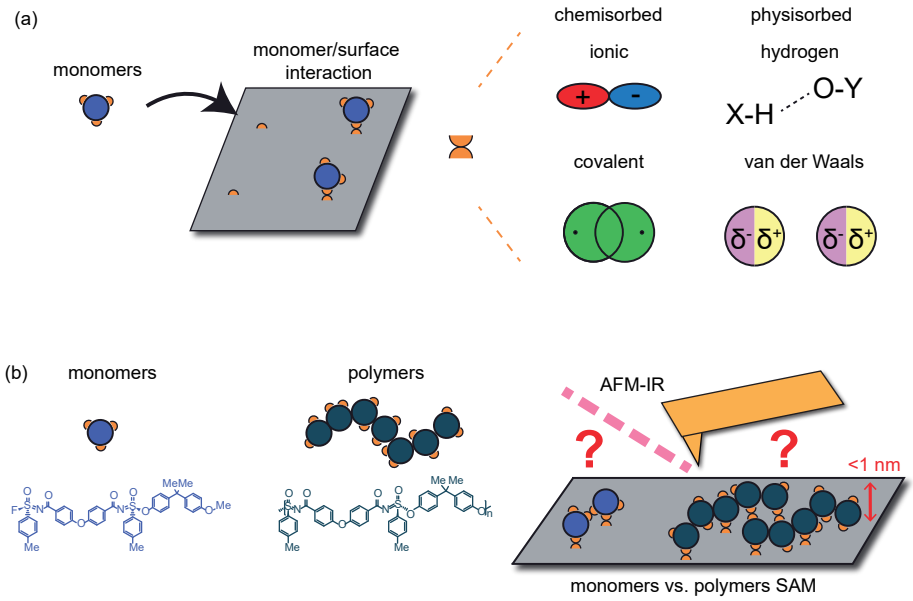

Figure 4.1. Framework for the Nano-analysis of the Intermolecular Interactions Driving SAM formation by Monomers and Polymers. (a) Left: Patch and ball model of a molecule adsorbate (blue) on a surface (grey) with possible interactions (orange patches). Right: Schematic representations of possible adsorbate-surface molecular interactions. (b) Left: Illustration and chemical structure of monomers (blue ball) and polymers (teal ball chain) (SI Synthesis). Right: AFM-IR nano-chemical analysis to unravel the role of intermolecular interactions in the formation and properties of SAMs at the sub-nanometer level.

4.2.2 Surface organization of monomer and polymer SAMs across coverage regimes

With this framework of well-defined SuFEx monomers and polymers in hand, the next step was to visualize the way in which monomers and polymers organize on a model substrate. We thus leveraged phase-controlled high-resolution 3-D imaging by AFM to investigate how our monomers and polymers could form SAMs.[25] Given the hydrophobic nature of our molecules and polymers, atomically flat and hydrophobic highly ordered pyrolytic graphite (HOPG) was chosen as the substrate. **Figure 4.2** compares the assembly behavior of monomers and polymers on HOPG across different surface coverage regimes, which were roughly divided into low, medium and high coverage.

For monomers, the AFM maps showed the process of SAM formation from low,

medium to high surface coverage regime, which we represented schematically next to the maps (**Figure 4.2a**, **Supplementary Fig. 4.1**). At low coverage, isolated monomers localized mostly at kink sites of HOPG steps. At medium coverage, some HOPG planes were partially covered by islands of monomers, while adjacent planes remained mostly empty. Only at high coverage, the surface was uniformly covered by a SAM, without showing any emerging patterns and lacking any evident supramolecular structure.

The polymers showed a SAM formation driven by the formation of an assembled network, as shown in the AFM maps and the relative schematics (**Figure 4.2b**, **Supplementary Fig. 4.2**). At low coverage, isolated bundles of individual chains and SAMs islands were present on the surface. At medium coverage, the polymers further associated into larger islands and an organized, extended, laterally connected network, spanning mesoscale distances. At high coverage, the polymer network consolidated into continuous SAMs, while retaining abundant pores similar as in the medium-coverage regime.

Comparing the assembling behavior on the surface, monomers formed a uniform featureless monolayer with coverage-independent adsorption behavior. Instead, the polymers assembled into a monolayer with a coverage-dependent behavior in conjunction with adsorbate-adsorbate interactions via lateral chains association.

4.2.3 Coverage-dependent structural changes of monomer and polymer SAMs

To elucidate how the different organization of monomers and polymers on the surface could relate to structural differences at the molecular level within the SAMs, we leveraged the sub-angstrom level noise of our AFM system (~0.2 Å). We thus studied how the cross-sectional height (thickness) of species, islands and SAMs formed by monomers and polymers varied as a function of surface coverage (**Figure 4.3**).

Figure 4.3a-b presents zoomed AFM maps of the monomers and polymers species, islands and SAMs; where colored lines represent example positions at which their cross-sectional heights are shown in **Figure 4.3c**. The cross-sections are then used to perform a statistical analysis of SAMs thickness (n=243, **Figure**

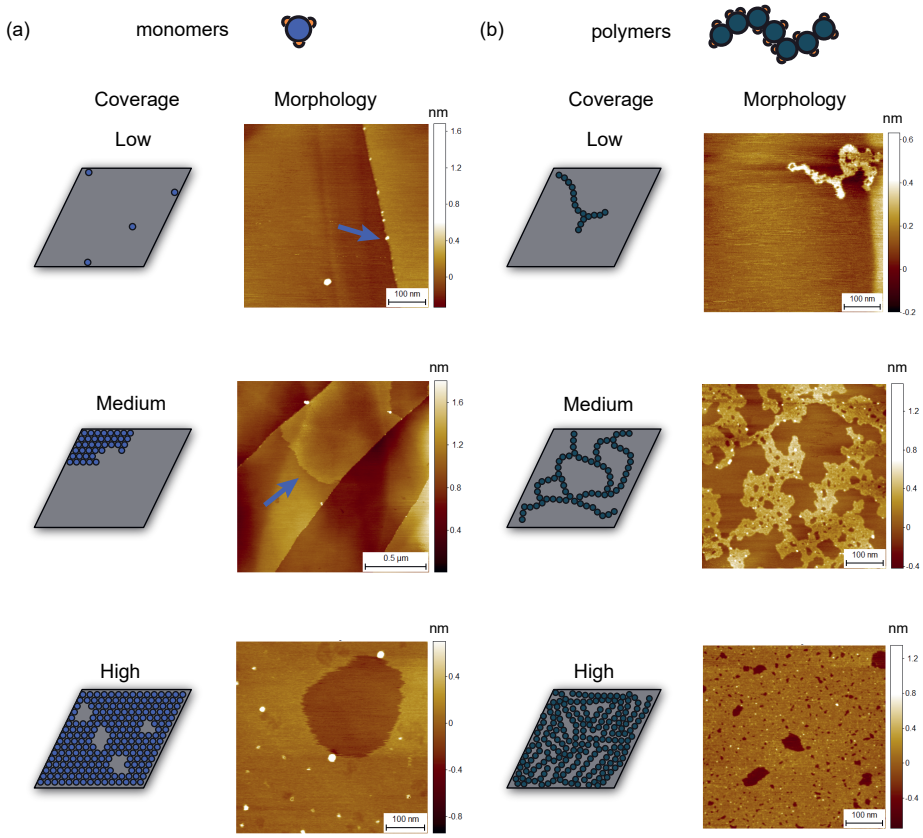

Figure 4.2. AFM characterization of SAMs formation by SuFEx monomers and polymers on HOPG. AFM morphology maps with schematic illustrations highlighting (a) monomers and (b) polymers at different coverage regimes – low, medium and high. For monomers, blue arrows mark: an assembly of monomers at low coverage; an island SAMs at medium coverage later leading to a continuous SAM at high coverage.

4.3d). In both cases, the surface was atomically flat down to a sub-Angstrom level (RMS = 0.17 Å), allowing to accurately measure height differences of ~0.5 Å.

For monomers, the cross-sectional height of the monomers, the locally formed assemblies and continuous SAM were constant (**Figure 4.3c**), and its distribution narrowly centered at 3.0 ± 0.5 Å, across all coverages indicating no coverage-dependent morphological changes (**Figure 4.3d**). The cross-sectional height of polymers, their assemblies, the locally formed and continuous SAM instead increased in height as a function of surface coverage (**Figure 4.3c**). Moreover, the height of SAMs formed by the polymers was always larger than that of the corresponding monomers at each coverage. Their average height increased as a

function of surface coverage from 4.0 ± 0.7 Å for low, to 4.5 ± 0.5 Å medium and to 5.5 ± 0.8 Å for high coverage.

The observed increase in height suggests that polymer form local islands and SAM via collective cooperative assembling, where higher surface coverage enhances lateral intermolecular interactions causing an increased height (thickness) of the SAM. Instead, the monomers form coverage-invariant islands and SAMs, with uniform height as a function of surface coverage, suggesting weaker intermolecular interactions competing with a substrate-driven adsorption.

4.2.4 Nanoscale chemical signatures of packing differences in monomer and polymer SAMs

To probe the difference in molecular interactions underlying the observed coverage-dependent morphological behavior of the monomer versus the polymer SAMs, we employed ultra-sensitive AFM-IR nano-chemical analysis with a sub-angstrom level noise (RMS ~ 0.2 Å, **Figure 4.4**).[21] We studied the SAMs formed at high coverage, where the largest morphological variations were observed (**Figure 4.4a-b, Supplementary Fig. 4.3-4.4**).

AFM-IR allowed acquiring spectra from both monomer and polymer SAMs across the IR fingerprint region (**Figure 4.4c**, 1780-1200 cm^{-1}), with high signal-to-noise SNR[26] >50 (**Methods**), despite the SAMs thickness being <1 nm (**Figure 4.3d**). The IR spectra of monomers and polymer SAMs showed a high degree of similarity, in agreement with their analogous chemical identity (**Figure 4.4c**, **Supplementary Fig. 4.3-4.4**). However, the polymers SAM showed the presence of a new distinct carbonyl (C=O) peak at 1725 cm^{-1}, which was absent in all monomer SAMs. For a quantitative assessment of this difference, we normalized the spectra at the signature of the O-C-O peak (1592 cm^{-1}) related to the backbone of the molecules, and then performed principal component analysis (PCA) within the 1760-1550 cm^{-1} region (**Figure 4.4c**). The relative score plot showed a clear separation of monomer and polymer spectra (95% CE ellipses). PC1 accounted for 81% of the variance between monomer and polymer SAMs, and the chemical difference was dominated for 65% by the signature of the emerging C=O peak at 1725 cm^{-1} (**Figure 4.4c**). For the polymers SAM, the additional band at 1725 cm^{-1} was consistent with a C=O situated in a densely stacked aromatic environment, where close π– π contacts suppress polar

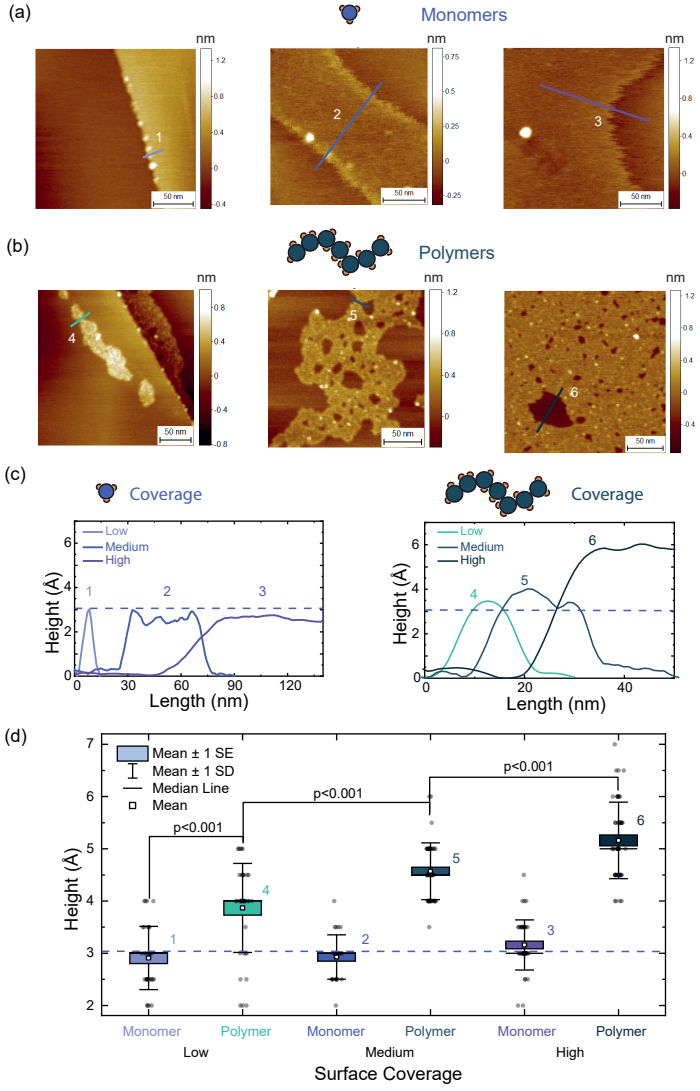

Figure 4.3. Sub-Angstrom AFM 3D Imaging of layer thickness of Monomer vs Polymer SAMs. (a) AFM morphological maps of (a) monomer and (b) polymer as a function of surface coverage: molecules and islands at low coverage (left), islands SAMs at medium coverage (center), continuous SAMs at high coverage (right). (c) Cross-sectional height profiles (thickness) of monomer (left), polymer (right) species and SAMs at low, medium, high coverage; colored lines on the maps indicate the position of representative cross-sections. (d) Statistical analysis of height of monomer and polymer species and SAMs as a function of surface coverage (n=243, box=1 Standard Error (SE); whiskers=1 Standard Deviation (SD); Fisher's two-tailed test).

interactions and hydrogen-bonding, stiffen the local field, and blue-shift the C=O stretching.[21]

To further evaluate how these different molecular interactions could influence the properties of the functional surfaces formed by the SAMs, we performed contact angle measurements (**Figure 4.4d**). The static water contact angle for HOPG was of 52 ± 1°.[27] This contact angle slightly increased to 59 ± 2° for the monomer SAM, but increased significantly to 105 ± 3° for the cooperative SAM formed by the polymers stabilized by lateral intermolecular π– π stacking. The substantial hydrophobisation of the surface may be related to a tighter aromatic packing reducing exposure of polar carbonyl/sulfonyl sites, the increased exposure at the surface of the several methyl groups in the polymers, and the nanostructured pattern of pores within the SAM.[28]

4.3 Discussion

In summary, this work provides a novel framework to elucidate at the monolayer level how substrate-adsorbate adhesion competes with adsorbate-adsorbate intermolecular interactions during SAM formation. We employ a click chemistry-based model system to showcase the ability to resolve the shift of balance between substrate–adsorbate adhesion and adsorbate–adsorbate intermolecular interactions, which contribute strongly to determine the role of collective cooperativity and intermolecular interactions in SAM formation.

For our monomers, adsorption on the surface lead to the formation of a featureless SAM with coverage-invariant thickness (~3 Å), without significant rearrangement of adsorbate conformation on the surface, and without significant change in surface wettability. Thus, suggesting that the formation of the SAM is driven by substrate–adsorbate interactions and weak adsorbate-adsorbate interactions. For the polymer, we observed that adsorbate–adsorbate interactions strengthen with increasing surface coverage leading to the formation of a SAM via stronger collective cooperativity, as evidenced by the coverage-dependent thickness increase from ~4 Å to ~5.5 Å related to significant intermolecular π–π stacking (new C=O band 1725 cm^{-1}), leading to a denser package of polymers and to increased exposure of non-polar sites, nano-structuring on the surface and a consequently highly increased hydrophobicity (contact angle ~105°). Overall, although both monomers and polymers initially adsorb and form islands on the surface via adsorbate-adsorbate interaction, the polymer SAM

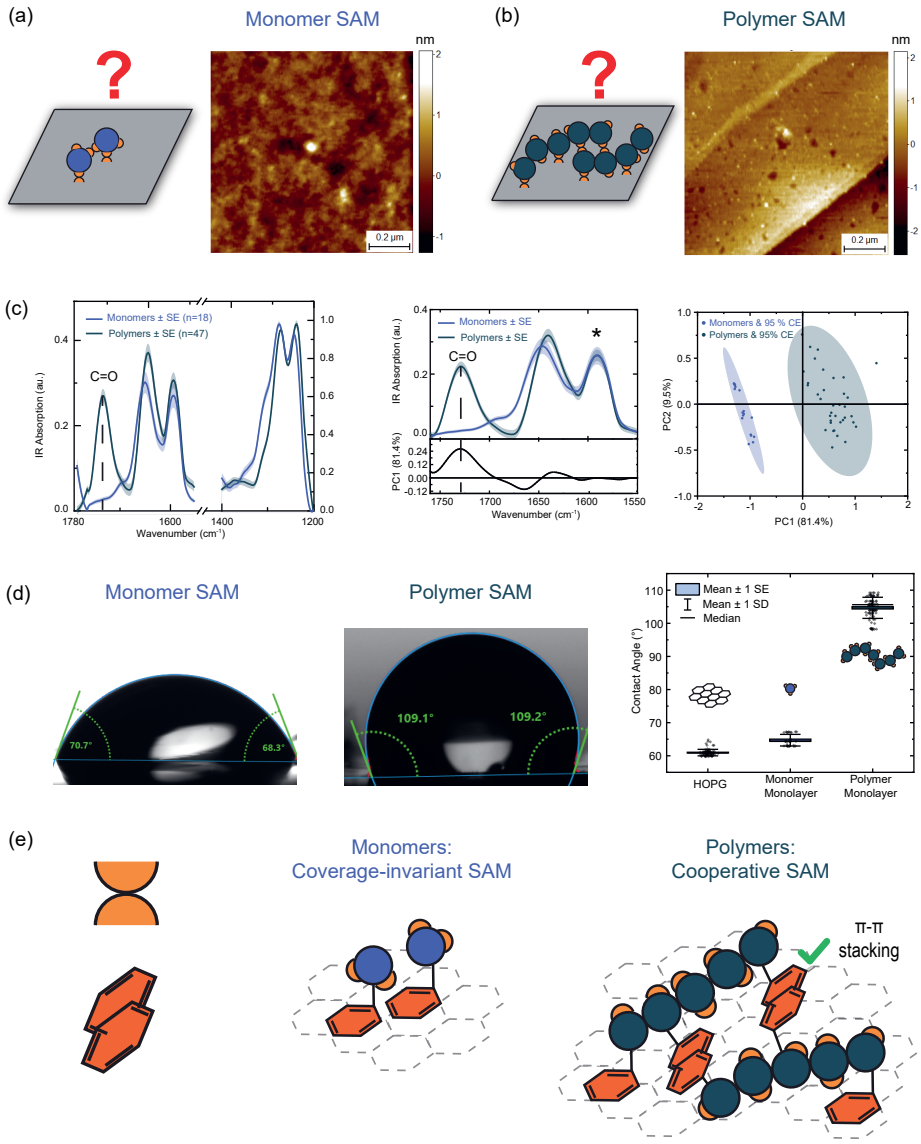

Figure 4.4. Nano-Chemical Analysis and Contact Angle Measurements of Monomers vs Polymer SAMs. AFM-IR morphology maps of SAMs formed by (a) monomers, (b) polymers. (c) Left: AFM-IR spectra of SAM formed by monomers (n=18, shading=1 SE) and polymers (n=47, shading=1 SE) within 1780-1200 cm^{-1}. Mid: PCA analysis of spectra of SAM of monomer (n=18, shading=1 SE) vs polymer (n=47, shading=1 SE) within 1760-1550 cm^{-1} with normalization to their backbone signature at 1592 cm^{-1}. Right: PCA score plot of the chemical signature of SAM formed by monomer (n=18, shading=95% CE) vs polymer (n=47, shading=95% CE). (d) Contact angle measurement of an aqueous droplet on the

formed SAMs. Right: Boxplot of contact angle of HOPG (N=3 independent experiment on different surfaces, n=90 replicates), monomer SAM (N=3, n= 32), polymer SAM (N=3, n=90) (box=1 SE, whisker=1 SD). (e) Left: Patch model (π-π stacking of benzene rings). Mid: Monomer monolayer with π-π stacking confined to substrate–adsorbate interactions. Right: Polymer monolayer with both substrate–adsorbate and intermolecular π-π stacking.

displays significantly stronger collective cooperativity, because of π–π staking intermolecular interactions (**Figure 4.4e**). Thus, our nano-analytical approach studying click-chemistry monomers and polymers, by AFM and AFM-IR with sub-nanometer sensitivity, allows quantifying (inter)-molecular interactions in SAMs in correlation with their supramolecular organization.

Our approach of combining sub-angstrom 3D imaging with nano-chemical analysis could be more broadly generalized to any SAM or other ultrathin coating where competition between substrate adhesion and intermolecular interactions is crucial. By studying how thickness, morphology, and specific molecular signatures change with surface coverage, the approach could distinguish whether assembly is adhesion-dominated or cooperative due to intermolecular interactions, and via the IR signals identify the relevant dominant molecular motifs (e.g., π–π stacking, hydrogen bonding). This information could in turn be useful to design functional surfaces in catalysis, electronics, and biosensing by tuning the balance between intermolecular interactions promoting cooperative assembly when tunable functionality is needed, versus surface adhesion leading to more uniform, coverage-invariant monolayers.

4.4 Supplementary information to:

Nano-Chemical Analysis of Intermolecular Interactions in Self-assembled Monolayers

1. Methods

General Conditions

All commercial chemicals were used as received and stored under argon. Reagents were used without further purification unless stated otherwise. Unless specified, reactions were conducted in untreated glassware. For selected reactions requiring anhydrous conditions, oven-dried glassware (heated above 100 ℃ for at least 5 h) or vacuum-dried glassware treated with a heat gun (T > 200 ℃) was used under oxygen- and moisture-free conditions. After weighing solids, glassware was connected to a Schlenk line, evacuated, and purged with nitrogen three times. Liquids were introduced via syringe through a rubber septum. Solvent abbreviations: n-hexane (n-hex), dichloromethane (DCM), tetrahydrofuran (THF), ethyl acetate (EA), N,N-dimethylformamide (DMF), and petroleum ether 40–60 (P.E.). All solvents were used as received without distillation.

Flash column chromatography was carried out on a Biotage® system using SiliCycle® precast silica gel columns (200–300 mesh or 300–400 mesh). Thin-layer chromatography (TLC) was performed on pre-coated, alumina-backed silica gel plates and visualized under UV light (254 nm) or by iodine staining.

Synthesis of Monomer 4-(2-(4-methoxyphenyl)propan-2-yl) phenyl N-(4-(4-(((R)-fluoro(oxo)(p-tolyl)-l6-sulfaneylidene) carbamoyl)phenoxy)benzoyl)-4-methylbenzenesulfonimidate:

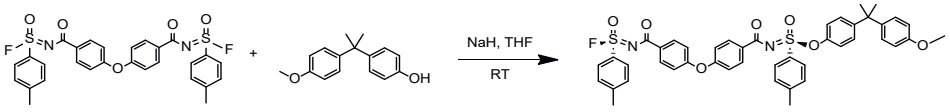

The two enantiomers, 4-(2-(4-methoxyphenyl)propan-2-yl)phenyl (R)-N-(4-(4-(((R)-fluoro(oxo)(p-tolyl)-l6-sulfaneylidene) carbamoyl)phenoxy)benzoyl)-4-methylbenzenesulfonimidate and 4-(2-(4-methoxyphenyl) propan-2-yl)phenyl (S)-N-(4-(4-(((S)-fluoro (oxo)(p-tolyl)-l6-sulfaneylidene) carbamoyl) phenoxy) benzoyl)-4-methylbenzenesulfonimidate : were synthesized according to a reported procedure[2]. Briefly, a dried 100 mL round-bottom flask was charged with (S)-N-(4-(4-(((R)-fluoro(oxo) (p-tolyl)-l6-sulfaneylidene) carbamoyl)phenoxy) benzoyl)-4-methylbenzenesulfonimidoyl fluoride (*R,S*) 25.0 mg, 0.044 mmol) and 4-(2-(4-methoxyphenyl)propan-2-yl)phenol (10.6 mg, 0.044 mmol) in dry THF

(1 mL). Sodium hydride (60% in oil, 2.0 mg, 0.044 mmol). was added, and the reaction mixture was stirred under an argon atmosphere at room temperature, with progress monitored by TLC. Upon completion, the reaction was quenched with water (10 mL) and the aqueous layer was extracted with dichloromethane (3 × 100 mL). The combined organic extracts were dried over anhydrous $MgSO_4$, and the solvent was removed under reduced pressure. The crude residue was purified by column chromatography on silica gel (eluent: n-hexane/EtOAc, 19:1 to 4:1, v/v) to afford the title compounds as a mixture of enantiomers (24 mg, 70% yield), obtained as white solids.

The obtained compound was characterized with NMR as followed, and matching results from literature[2]:

^{1}H NMR (400 MHz, $CDCl_3$) δ 8.01 (dd, *J* = 8.6, 6.3 Hz, 4H), 7.92 (d, *J* = 8.2 Hz, 2H), 7.82 (d, *J* = 8.2 Hz, 2H), 7.33 (s, 2H), 7.23 (d, *J* = 8.1 Hz, 2H), 7.02 (d, *J* = 8.8 Hz, 2H), 6.97 – 6.83 (m, 8H), 6.65 (d, *J* = 8.8 Hz, 2H), 3.64 (s, 3H), 2.35 (d, *J* = 16.8 Hz, 6H), 1.48 (s, 6H).

^{13}C NMR (101 MHz, $CDCl_3$) δ 171.00, 169.38, 160.98, 159.80, 157.73, 150.49, 147.29, 147.07, 145.73, 142.29, 133.66, 132.42, 132.08, 131.72, 131.51, 131.39, 130.42, 130.03, 129.80, 129.68, 128.37, 128.19, 128.15, 127.84, 122.45, 122.27, 118.72, 118.43, 113.51, 77.48, 77.36, 77.16, 76.84, 55.35, 42.31, 31.06, 29.85, 22.02, 21.90.

^{19}F NMR (376 MHz, $CDCl_3$) δ 65.27.

Synthesis of Polymers

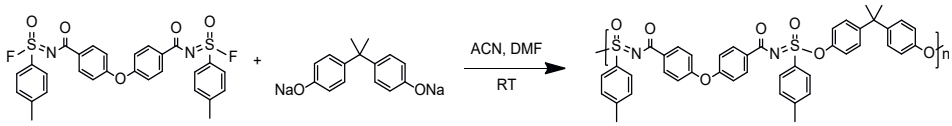

RS-diSF (RS-disulfonimidoyl fluoride) (25.0 mg, 0.044 mmol) and disodium bisphenol (12.0 mg, 0.044 mmol) were placed in a reaction vial under an argon atmosphere. Anhydrous ACN (0.1 mL, Biosolve HPLC grade) and anhydrous DMF (0.1 mL, Biosolve HPLC grade) were added, and the mixture was stirred vigorously for 48 hours. Methanol (10 mL) was then added to reduce the polymer's solubility, and stirring was paused to allow precipitation. The supernatant was removed

carefully without disturbing the precipitate. The precipitate was redissolved in just enough THF (Biosolve HPLC grade, unstabilized) and reprecipitated with methanol. This redissolution–precipitation cycle was repeated eight times. The final polymer was dried in a vacuum oven at 50 °C overnight. Yield: 3.0 mg (0.0052 mmol, 12%), as a white powder.

The obtained compound is characterized with NMR, matching with literature[2]: ^{1}H NMR (400 MHz, $CDCl_3$) δ 8.13 (d, J = 8.0 Hz, 4H), 7.93 (d, J = 8.0 Hz, 4H), 7.35 (d, J = 8.0 Hz, 4H), 7.08 (d, J = 8.0 Hz, 4H), 7.00 (d, J = 8.0 Hz, 8H), 2.45 (s, 6H), 1.58 (s, 6H); ^{13}C NMR (101 MHz, $CDCl_3$) δ 171.05, 160.19, 149.45, 147.3, 145.83, 133.56, 132.04, 131.02, 130.07, 128.32, 128.17, 122.45, 118.46, 42.80, 30.92, 21.91. ^{19}F NMR (376 MHz, $CDCl_3$).

NMR Measurements

^{1}H, ^{13}C{^{1}H}, and ^{19}F NMR spectra were recorded on a Bruker Avance III 400 MHz spectrometer at 298 K. Chemical shifts are reported in ppm on the δ scale and coupling constants (*J*) are given in hertz (*Hz*).

^{19}F NMR spectra were not referenced, while other chemical shifts were calibrated to residual non-deuterated solvent signals: $CDCl_3$ (δ = 7.26 ppm for ^{1}H, 77.16 ppm for ^{13}C{^{1}H}). NMR data are described using the following abbreviations: chemical shift (δ, ppm), multiplicity (s = singlet, d = doublet, t = triplet, q = quartet, dt = doublet of triplets, m = multiplet, br = broad), and coupling constant (*J, Hz*).

High-resolution mass spectra (HR-MS) measurements

The Quadrupole Time-of-Flight (QTOF) micro-spectrometer (Thermo Fisher Scientific Inc., United States) was used to obtain high-resolution mass spectra (HR-MS). Measurements were performed using electrospray ionization in positive (ESI^+) or negative (ESI^-) mode. The Q-Exactive Focus provided a resolving power of up to 70,000 (FWHM) at m/z 200, with a mass range of 100–1,200 Da, mass accuracy better than 1 ppm, and a maximum scan speed of 12 Hz.

Analytical HPLC measurements

Analytical HPLC was used solely for the quantification of the chiral mixture. Separation was performed on a CHIRALPAK® IA column (4.6 mm I.D × 250 mm, 5 μm, Part No. 80325, Daicel Corporation) using hexane/dichloromethane/

isopropanol (32:8:1) as the mobile phase. The flow rate was 0.5 mL/min, and 10 µL of a di-SF mixture (0.2 g/mL) was injected per run. Detection was performed at 230 nm, and all measurements were carried out at room temperature.

Preparative HPLC

Preparative HPLC was used to separate the RS isomer from the racemic mixture containing RS, RR, and SS isomers. Separation was performed on a CHIRALPAK® IA column (20 mm I.D × 250 mm, 5 µm, Part No. 80345, Daicel Corporation) with the same eluent (32:8:1). The flow rate was 5 mL/min, and 50 µL of a di-SF mixture (0.4 g/mL) was injected per run. Detection was performed at 230 nm, and all measurements were carried out at room temperature.

Gel Permeation Chromatography (GPC) measurements

The polymer molecular weight (weight-average, M_w) and polydispersity (Đ) relative to polystyrene standards were determined on an Agilent Technologies 1200 GPC system. The system was equipped with a diode-array detector (DAD, G1315D, data collected at 250, 260, and 290 nm), a refractive index detector (RID, G1362A), autosampler (ALS, G1329A), binary pump (G1312A), and solvent degasser (G1322A). Separation was achieved using a VARIAN PLgel 5 µm MIXED-D column (300 × 7.5 mm, Part No. PL1110-6504). Calibration was performed with EasyVial PS-M and EasyVial PS-L polystyrene standards (Agilent Technologies), covering a molecular weight range from Mp 400 to 2,000,000 Da (Fluka). HPLC-grade N,N-dimethylformamide (DMF, Biosolve®, unstabilized) containing 0.1% LiBr (≥99%, Sigma-Aldrich) was used as the mobile phase. The elution rate was 1.0 mL/min, and all measurements were performed at room temperature or 25 ℃. Samples and standards were injected at 10 µL (1.0 mg/mL).

AFM Sample Preparation

Samples deposition for atomic force microscopy (AFM) analysis was performed on two differently charged substrates: hydrophobic highly ordered pyrolytic graphite (HOPG) and negatively charged Mica. Sample preparation was realized by vacuum drying. at room temperature by deposition of a 10 µL droplet of 2-50 µg/mL monomers/polymers solution in THF for and dried under vacuum in 3 seconds.

AFM Measurements

Atomic force microscopy (AFM) measurements were performed on a NX10 AFM (Park Systems, South Korea) operating in True Non-Contact™ Mode with a silicon tip PPP-NCSTR (Park Systems, nominal spring constant 7.4 $N.m^{-1}$, nominal tip radii ~ 7 nm). Image was acquired with a tip velocity of 0.8 μm per second. Two map sizes with two pixelization setting were employed: 2×2 μm^2 with 2 nm/px, 1×1 μm^2 and 0.5×0.5 μm^2 with 1 nm/px.

Ultra Hi-res AFM Measurements

Ultra Hi-res Atomic force microscopy (AFM) measurements were performed on a NX10 AFM (Park Systems, South Korea) operating in True Non-Contact™ Mode with a silicon tip SSS-NCHR (Park Systems, nominal spring constant 42 Nm^{-1}, nominal tip radii ~ 2nm). Image was acquired with a tip velocity of 1 μm per second. Two map sizes and two pixelization setting were employed: 1×1 μm^2 with 1 nm/px and 0.4×0.4 μm^2 with 0.4 nm/px.

AFM Measurements Analysis

Image flattening and single polymers chains cross-sectional dimension analysis were performed by SPIP (Image Metrology, Denmark) software. The image was first flattened with a first order polynomial fit for the global correction, and then, a zero order least mean square (LMS) fit line-wise correction. Afterwards, the image was further flattened by first and second order LMS fit line-wise correction with area of interest masked.

AFM-IR measurements, maps treatment and analysis

AFM-IR spectra were collected using a nanoIR3 (Bruker, USA) was performed on atomically flat HOPG substrates. The morphology of the polymer samples was scanned by the nanoIR microscopy system, with a rate line within 0.1-0.5 Hz and in contact mode. All AFM maps were acquired with a resolution between 1-30 nm/pixel. A silicon gold coated PR-EX-nIR2 (Bruker, USA) cantilever with a nominal radius of ~ 30 nm and an elastic constant of about 0.2 N/m was used. The AFM images were treated and analyzed using SPIP software. The height images were first order flattened.

All measurements were performed at room temperature under controlled nitrogen atmosphere with relative humidity below 3%. Both spectra and images were acquired by using phase loop (PLL) tracking of contact resonance, the

phase was set to zero to the desired resonant frequency around the IR amplitude maximum, and tracked with an integral gain I=0.2 and proportional gain P=1.[1]

Contact Angle Measurements

Contact angle measurement was performed on a Krüss DSA 100 contact angle goniometer (Krüss, Germany) was employed to measure the wettability of the samples. The volume of the deionized water drop is 2.0 μL. The tangent 2 fitting model was used for the contact angle measurement of all samples.

AFM-IR Spectra Signal to Noise Ratio Calculation

AFM-IR spectra signal to noise ratio (SNR) is defined as ratio of the signal amplitude to the replicate-based RMS noise , i.e.,

$$SNR = \frac{S}{\sigma_{RMS}}$$

We first calculated the pointwise mean spectra by averaged the IR amplitude at each wavenumber as:

$$\overline{y}(\tilde{v}_j) = \frac{1}{N}\sum_{i=1}^{N} y_i(\tilde{v}_j)$$

RMS noise was calculated as pooled residual RMS:

$$\sigma_{RMS} = \sqrt{\frac{1}{NM}\sum_{i=1}^{N}\sum_{j=1}^{M}(y_i(\tilde{v}_j) - \overline{y}(\tilde{v}_j))^2} \approx 0.139$$

Signal amplitude was defined as mean of highest peak amplitude of each individual spectra , i.e.,

$$S = \frac{1}{N}\sum_{i=1}^{N} \max_i(s_i(\tilde{v})) \approx 7.831$$

Then we obtained the final SNR value estimation as:

$$SNR = \frac{S}{\sigma_{RMS}} \approx \frac{7.831}{0.139} \approx 56$$

2. Supplementary Figures

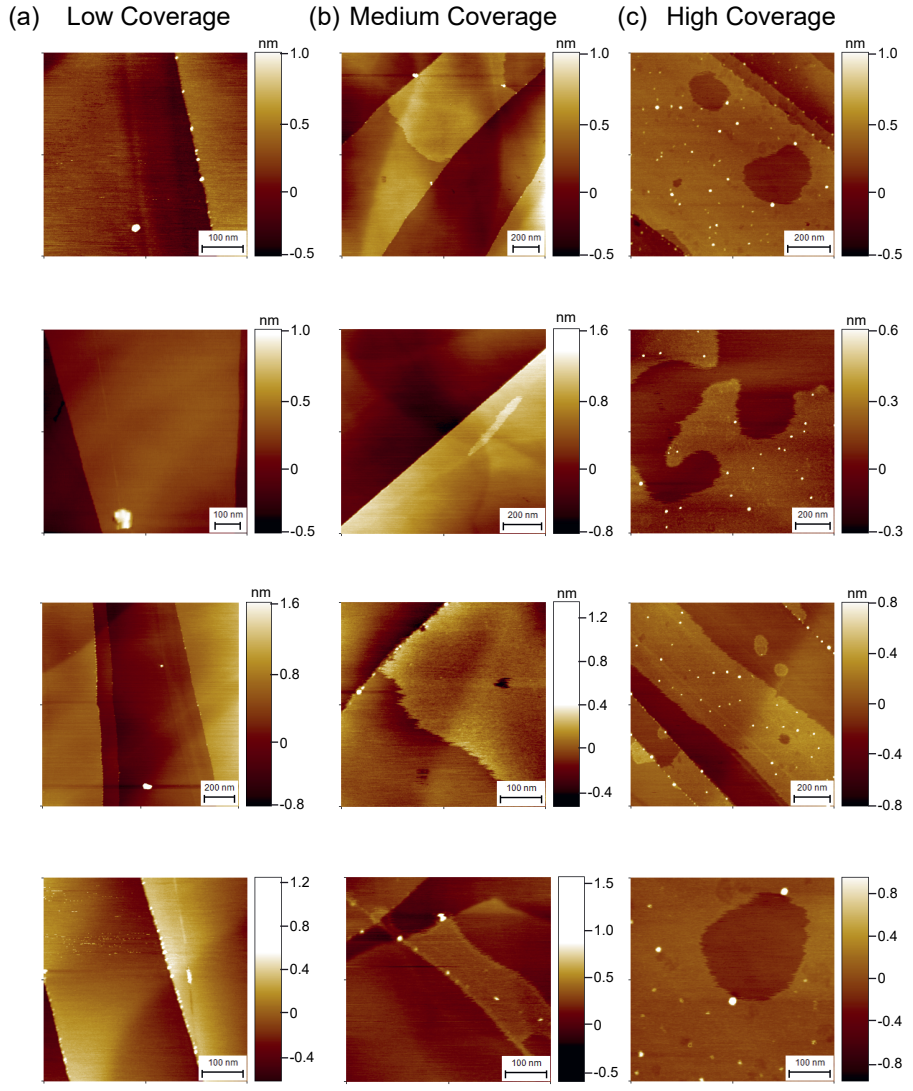

Supplementary Figure 4.1. AFM Maps of Monomers at (a) low; (b) Medium; (c) High surface coverage on HOPG.

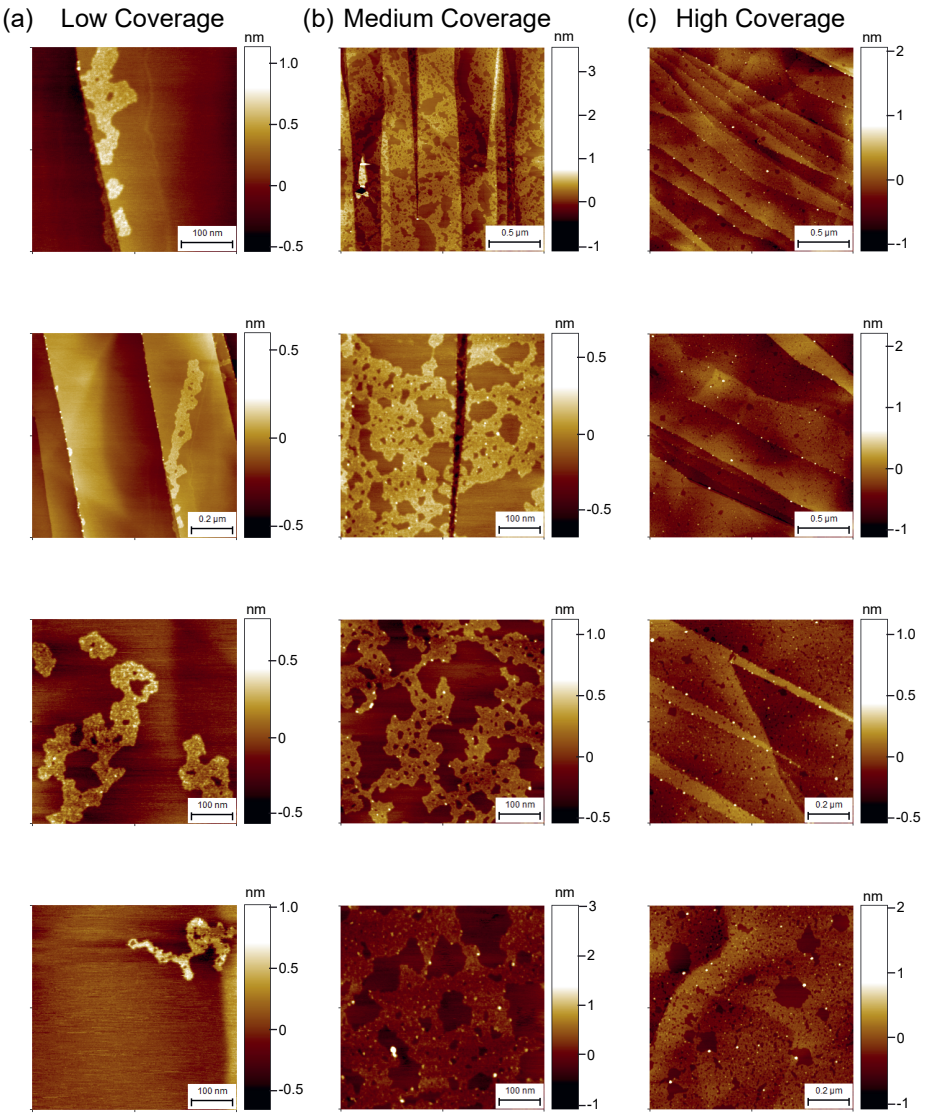

Supplementary Figure 4.2. AFM Maps of Polymers at (a) low; (b) Medium; (c) High surface coverage on HOPG.

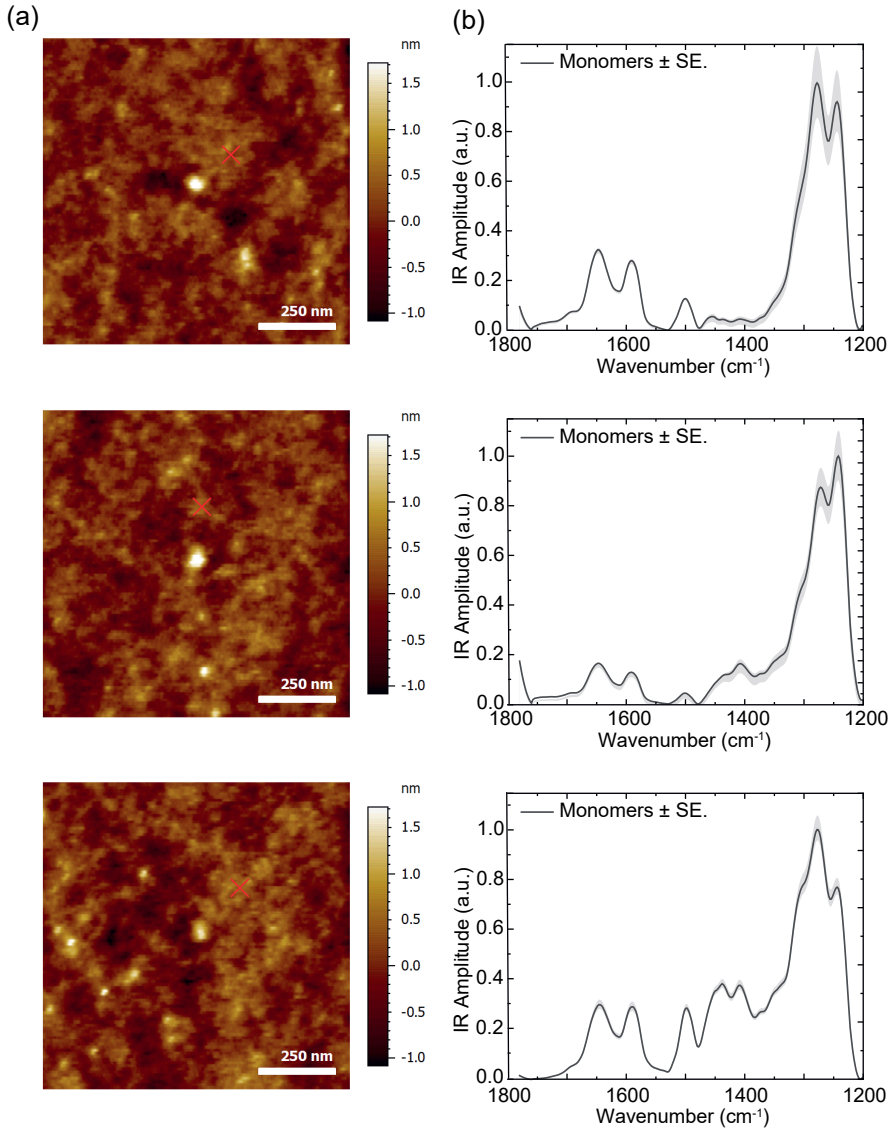

Supplementary Figure 4.3. AFM-IR (a) Morphological maps and (b) Spectra of monomers (n=6 each, shading = 1 SE).

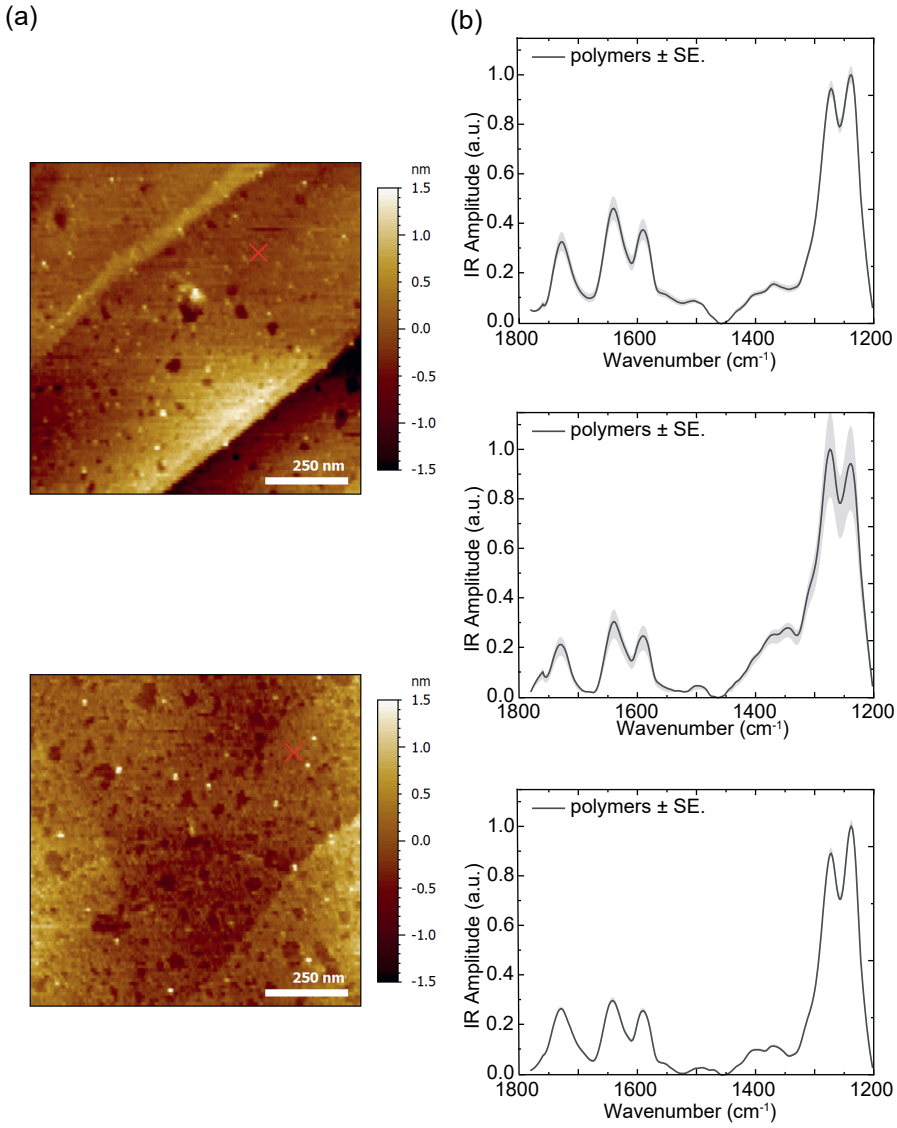

Supplementary Figure 4.4. AFM-IR (a) Morphological maps and (b) Spectra of polymers (top: n = 17; mid: n = 13; bottom: n = 17; shading = 1 SE).

3. References

(1) Pujari, S. P.; Scheres, L.; Marcelis, A. T. M.; Zuilhof, H. Covalent surface modification of oxide surfaces. *Angew. Chem. Int. Ed.* **2014**, 53 (25), 6322–6356. DOI: 10.1002/anie.201306709.

(2) Ulman, A. Formation and structure of self-assembled monolayers. *Chem. Rev.* **1996**, 96 (4), 1533–1554. DOI: 10.1021/cr9502357.

(3) Marshall, S. T.; O'brien, M.; Oetter, B.; Corpuz, A.; Richards, R. M.; Schwartz, D. K.; Medlin, J. W. Controlled selectivity for palladium catalysts using self-assembled monolayers. *Nat. Mater.* **2010**, 9, 853–858. DOI: 10.1038/nmat2849.

(4) Dong, B.; Wei, M.; Li, Y.; Yang, Y.; Ma, W.; Zhang, Y.; Ran, Y.; Cui, M.; Su, Z.; Fan, Q.; et al. Self-assembled bilayer for perovskite solar cells with improved tolerance against thermal stresses. *Nat. Energy* **2025**, 10 (3), 342–353. DOI: 10.1038/s41560-024-01689-2.

(5) Samanta, D.; Sarkar, A. Immobilization of bio-macromolecules on self-assembled monolayers: Methods and sensor applications. *Chem. Soc. Rev.* **2011**, 40 (5), 2567–2592. DOI: 10.1039/c0cs00056f.

(6) Azzaroni, O.; Salvarezza, R. C. Chemisorbed self-assembled monolayers. In Supramolecular chemistry: From molecules to nanomaterials, Gale, P. A., Steed, J. W. Eds.; John Wiley & Sons, 2012; pp 3445–3459.

(7) Gong, J.; Wan, L.; Yuan, Q.; Bai, C.; Jude, H.; Stang, P. J. Mesoscopic self-organization of a self-assembled supramolecular rectangle on highly oriented pyrolytic graphite and au(111) surfaces. *Proc. Natl. Acad. Sci. U. S. A.* **2004**, 102 (4), 971–974. DOI: 10.1073/pnas.0409145102.

(8) Mali, K. S.; De Feyter, S. Principles of molecular assemblies leading to molecular nanostructures. Philos. *Trans. R. Soc.*, A **2013**, 371 (2000), 20120304. DOI: 10.1098/rsta.2012.0304.

(9) Gatti, R.; Macleod, J. M.; Lipton-Duffin, J. A.; Moiseev, A. G.; Perepichka, D. F.;

Rosei, F. Substrate, molecular structure, and solvent effects in 2d self-assembly via hydrogen and halogen bonding. *J. Phys. Chem. C* **2014**, 118 (44), 25505–25516. DOI: 10.1021/jp507729w.

(10) Grimme, S. Do special noncovalent pi-pi stacking interactions really exist? *Angew. Chem. Int. Ed.* **2008**, 47 (18), 3430–3434. DOI: 10.1002/anie.200705157.

(11) Shao, L.; Ma, J.; Prelesnik, J. L.; Zhou, Y.; Nguyen, M.; Zhao, M.; Jenekhe, S. A.; Kalinin, S. V.; Ferguson, A. L.; Pfaendtner, J.; et al. Hierarchical materials from high information content macromolecular building blocks: Construction, dynamic interventions, and prediction. *Chem. Rev.* **2022**, 122 (24), 17397–17478. DOI: 10.1021/acs.chemrev.2c00220.

(12) Schwartz, D. K. Mechanisms and kinetics of self-assembled monolayer formation. *Annu. Rev. Phys. Chem.* **2001**, 52, 107–137. DOI: 10.1146/annurev.physchem.52.1.107.

(13) Park, J. W.; Kim, H.; Han, M. Polymeric self-assembled monolayers derived from surface-active copolymers: A modular approach to functionalized surfaces. *Chem. Soc. Rev.* **2010**, 39 (8), 2935–2947. DOI: 10.1039/b918135k.

(14) Asadi, V.; Li, X.; Ruggeri, F. S.; Zuilhof, H.; Van Der Gucht, J.; Kodger, T. E. Synthesis of well-defined linear–bottlebrush–linear triblock copolymer towards architecturally-tunable soft materials. *Polym. Chem.* **2022**, 13 (32), 4666–4674. DOI: 10.1039/D2PY00841F.

(15) Goronzy, D. P.; Ebrahimi, M.; Rosei, F.; Arramel; Fang, Y.; De Feyter, S.; Tait, S. L.; Wang, C.; Beton, P. H.; Wee, A. T. S.; et al. Supramolecular assemblies on surfaces: Nanopatterning, functionality, and reactivity. *ACS Nano* **2018**, 12 (8), 7445–7481. DOI: 10.1021/acsnano.8b03513.

(16) Hu, S.; Yan, J.; Yang, G.; Ma, C.; Yin, J. Self-assembled polymeric materials: Design, morphology, and functional-oriented applications. *Macromol. Rapid. Commun.* **2022**, 43 (14). DOI: 10.1002/marc.202100791.

(17) White, T. W.; Martsinovich, N.; Troisi, A.; Costantini, G. Quantifying the "subtle interplay" between intermolecular and molecule–substrate interactions

in molecular assembly on surfaces. *J. Phys. Chem. C* **2018**, 122 (31), 17954–17962. DOI: 10.1021/acs.jpcc.8b06797.

(18) Korolkov, V. V.; Summerfield, A.; Murphy, A.; Amabilino, D. B.; Watanabe, K.; Taniguchi, T.; Beton, P. H. Ultra-high resolution imaging of thin films and single strands of polythiophene using atomic force microscopy. *Nat. Commun.* **2019**, 10 (1), 1537. DOI: 10.1038/s41467-019-09571-6.

(19) Kurouski, D.; Dazzi, A.; Zenobi, R.; Centrone, A. Infrared and raman chemical imaging and spectroscopy at the nanoscale. *Chem. Soc. Rev.* **2020**, 49 (11), 3315–3347. DOI: 10.1039/C8CS00916C.

(20) Ruggeri, F. S.; Habchi, J.; Chia, S.; Horne, R. I.; Vendruscolo, M.; Knowles, T. P. J. Infrared nanospectroscopy reveals the molecular interaction fingerprint of an aggregation inhibitor with single aβ42 oligomers. *Nat. Commun.* **2021**, 12 (1), 688. DOI: 10.1038/s41467-020-20782-0.

(21) Li, X.; Pujari, S. P.; Van Der Gucht, J.; Zuilhof, H.; Ruggeri, F. S. Unravelling emergence of chirality in click-chemistry polymers down to the single-chain level. *Nat. Commun.* **2025**, 16 (1), 6761. DOI: 10.1038/s41467-025-62041-0.

(22) Liang, D. D.; Pujari, S. P.; Subramaniam, M.; Besten, M.; Zuilhof, H. Configurationally chiral sufex-based polymers. *Angew. Chem. Int. Ed.* **2022**, 61 (8). DOI: 10.1002/anie.202116158.

(23) Isikgor, F. H.; Pradhan, R. R.; Zhumagali, S.; Maksudov, T.; Naphade, D.; Petoukhoff, C. E.; Khan, J. I.; Hnapovskyi, V.; Harrison, G. T.; Combe, C.; et al. Self-assembled monolayer dyes for contact-passivated and stable perovskite solar cells. *Adv. Energy Mater.* **2025**, 15 (1). DOI: 10.1002/aenm.202402630.

(24) Li, C.; Li, Q.; Kaneti, Y. V.; Hou, D.; Yamauchi, Y.; Mai, Y. Self-assembly of block copolymers towards mesoporous materials for energy storage and conversion systems. *Chem. Soc. Rev.* **2020**, 49 (14), 4681–4736. DOI: 10.1039/d0cs00021c.

(25) Ruggeri, F. S.; Vieweg, S.; Cendrowska, U.; Longo, G.; Chiki, A.; Lashuel, H. A.; Dietler, G. Nanoscale studies link amyloid maturity with polyglutamine diseases onset. *Sci. Rep.* **2016**, 6, 31155. DOI: 10.1038/srep31155.

(26) Hendriks, R. C.; Gerkmann, T. Estimation of the noise correlation matrix. In 2011 IEEE International Conference on Acoustics, Speech and Signal Processing (ICASSP), 22–27 May 2011, 2011; pp 4740–4743. DOI: 10.1109/ICASSP.2011.5947414.

(27) Zou, Y.; Walton, A. S.; Kinloch, I. A.; Dryfe, R. a. W. Investigation of the differential capacitance of highly ordered pyrolytic graphite as a model material of graphene. *Langmuir* **2016**, 32 (44), 11448–11455. DOI: 10.1021/acs.langmuir.6b02910.

(28) Papadopoulos, P.; Mammen, L.; Deng, X.; Vollmer, D.; Butt, H.-J. How superhydrophobicity breaks down. *Proc. Natl. Acad. Sci. U. S. A.* **2013**, 110 (9), 3254–3258. DOI: 10.1073/pnas.1218673110.

Chapter 5

General Discussion

5.1 Main advances of this thesis

This thesis shows that the organization of polymers and functional surfaces arises from heterogeneity, hierarchical structural organization, and intermolecular interactions across molecular, single-feature, supramolecular, and monolayer length scales, which are resolved here beyond bulk-average characterization methods through nanoscale and single-feature-resolved analysis. A central advance brought about by the work described in this thesis is that morphology and chemical information are directly correlated across molecular, single-feature, supramolecular, and monolayer levels of organization, thereby making it possible to distinguish heterogeneity at the single-molecule level, follow the emergence of hierarchical structural organization, and identify the intermolecular interactions governing monolayer organization. Across the three research chapters, the correlation of morphology and chemical information constitutes the main analytical advance of this thesis.

Chapter 2 shows that AFM-based single-feature-resolved analysis can estimate molecular weight and distribution of single polymer chains and quantify heterogeneity beyond bulk-averaged readouts by resolving differences in apparent area, height, morphology and aggregate state between individual surface-supported polymer features. This establishes heterogeneity as an intrinsic and analytically relevant feature of surface-supported polymer systems rather than a deviation from one averaged population. **Chapter 3** shows that chirality in the polymer system is expressed across molecular, single-chain, and supramolecular length scales, thereby establishing that chirality emerges hierarchically from repeating-unit conformation to polymer backbone and supramolecular organization. This shows that hierarchical structural organization can be resolved beyond ensemble-averaged characterization rather than being confined to one structural level. **Chapter 4** shows that different balances between substrate–adsorbate and adsorbate–adsorbate interactions give rise to distinct monolayer structures and chemical signatures, specifically a coverage-invariant monomer monolayer and a cooperative polymer monolayer with coverage-dependent structural and chemical evolution. This establishes intermolecular interactions as the governing basis of monolayer organization in functional surfaces. In this way, **Chapters 2**, **3**, and **4** respectively define the main advances of this thesis in terms of heterogeneity, hierarchical structural organization, and intermolecular interactions.

The following sections discuss the advances of this thesis in turn. **Section**

5.2, based primarily on **Chapter 2** and further supported by **Chapters 3** and **4**, discusses why bulk-average characterization methods alone are insufficient to describe the studied systems and how heterogeneity across different length scales becomes analytically relevant. **Section 5.3** then discusses, mainly on the basis of **Chapters 3** and **4**, how heterogeneity develops into hierarchical structural organization. **Section 5.4** addresses, based primarily on **Chapters 3** and **4**, how intermolecular interactions govern this organization. On that basis, **Section 5.5** discusses the role of AFM and AFM-IR in enabling nanoscale chemical interpretation, and **Section 5.6** considers the broader scientific relevance, and future outlook of this thesis.

5.2 From bulk-average characterization methods to local heterogeneity

This thesis establishes that polymers and functional surfaces cannot be adequately understood from bulk-average characterization methods alone, because their relevant organization is locally heterogeneous. Bulk-average characterization methods remain essential for defining the overall composition and average material properties, but they do not fully describe the systems investigated. Nanoscale characterization is important, precisely because it discovers local variations that remain hidden within average readouts.[1]

Surface-supported polymer systems are composed of discrete polymer features that differ in morphology, molecular weight, and aggregate state. **Chapter 2** shows that individual polymer features cannot be treated simply as equivalent units belonging to one averaged population, because they differ in apparent area, height, morphology, molecular weight, and aggregation state. In this way, AFM-based analysis preserves single-feature-level molecular-weight distributions beyond bulk-averaged readouts and allows clustered populations of different aggregate states to be resolved. The significance of this result lies not only in approaching molecular-weight-related information on a single-feature-resolved basis, but also in showing that nanoscale variation is itself an intrinsic feature of the polymer sample rather than a deviation from its average description.

Chapter 3 further shows chemical-structural heterogeneity in the studied polymer system. Bulk Chiral-HPLC, CD, IR, and UV-Vis provide essential information on average differences between racemic and chiral species, but do not directly differentiate how chirality is manifested across single polymer chains, few-chain assemblies, and supramolecular structures. **Chapter 4** similarly shows that monomer and polymer self-assembled monolayers cannot be understood sufficiently from average characterization alone, because their organization differs across coverage regimes and is accompanied by distinct structural and chemical signatures.

Heterogeneity is therefore part of the relevant organization of the studied systems rather than a deviation from average description. In the studied polymer and surface systems, variation across single-feature, assembly, and monolayer states remains unresolved in ensemble-averaged outputs. Heterogeneity thus becomes analytically relevant when organization is resolved beyond average readouts.

5.3 From local heterogeneity to hierarchical structural organization

This thesis demonstrates that hierarchical structural organizations in polymers and functional surfaces develop from local heterogeneities across molecular, single-chain, supramolecular, and monolayer length scales. Once formed, this hierarchical structural organization further contributes to the overall local heterogeneity by generating additional structural variation across higher levels of organization. Nanoscale characterization thus reveals heterogeneity both in local chemical-structural states and in the hierarchical structures that develop from them.[2]

Hierarchical structural organization is most directly demonstrated in **Chapter 3** through the emergence of chirality from small molecules to single chains and supramolecular assemblies. The key result of **Chapter 3** is not only that racemic and chiral species differ in bulk spectroscopic measurements, but that chirality emerges across molecular, single-chain, and supramolecular length scales. Central chirality is already present at the molecular level and is associated with different conformational states of the repeating units, while polymerization gives rise to backbone chirality in chiral polymers and supramolecular chirality

in racemic polymers. **Chapter 3** therefore shows that chirality is not confined to one structural level, but can be resolved across multiple connected levels of organization.

Chapter 4 shows a related progression in functional surfaces. The self-assembly of monomers and polymers on HOPG does not proceed simply as a uniform increase in average surface coverage, but through different forms of monolayer organization. Monomers progress toward a featureless continuous monolayer, whereas polymers develop more extended and laterally organized monolayer structures. **Chapter 4** therefore shows that monolayer organization in functional surfaces also develops hierarchically across different length scales.

Hierarchical structural organization therefore develops from heterogeneity across different length scales. In the studied systems, molecular, single-chain, supramolecular, and monolayer organization are not isolated structural levels, but connected levels of organization. Hierarchical structural organization thus emerges from heterogeneity and further contributes to structural variation across higher levels of organization.

5.4 Intermolecular interactions govern local heterogeneity and hierarchical structural organization

This thesis establishes that local heterogeneity and hierarchical structural organization in polymers and functional surfaces are governed by intermolecular interactions. The local and higher-order structures discussed above are not independent structural observations, but reflect different intermolecular interaction regimes that determine packing, association, assembly, and local organization. The relevant properties of these systems therefore cannot be understood from their chemical identity alone.[3]

The role of intermolecular interactions is most explicitly resolved in the self-assembled monolayers formed by monomers and polymers on HOPG in **Chapter 4**. The monomer and polymer systems do not simply represent two different adsorbates on the same substrate, but two different balances between substrate–adsorbate and adsorbate–adsorbate interactions. The monomer system forms

a coverage-invariant monolayer without pronounced structural reorganization, consistent with a monolayer governed primarily by substrate–adsorbate interactions. The polymer system instead forms a cooperative monolayer with coverage-dependent increase in height, abundant lateral association, an emergent carbonyl band at ~1725 cm^{-1}, and a strong increase in water contact angle, together indicating that adsorbate–adsorbate intermolecular interactions play a dominant role in monolayer organization and surface properties.

Chapter 3 supports the same general conclusion beyond monolayer formation. The emergence of supramolecular chirality in the racemic polymer system is linked to intermolecular π–π interactions, showing that polymer organization beyond isolated chains also develops through intermolecular association.

Intermolecular interactions therefore govern how organization develops in the studied systems. Differences in aggregate state, supramolecular assembly, and monolayer organization reflect different intermolecular interaction regimes. Intermolecular interactions thus provide the basis linking heterogeneity to hierarchical structural organization.

5.5 AFM-IR enables nanoscale chemical interpretation of local heterogeneity, hierarchical structural organization, and intermolecular interactions

This thesis establishes that AFM-IR enables a nanoscale chemical interpretation of heterogeneity, hierarchical structural organization, and intermolecular interactions beyond what bulk-average readouts can reveal. In the studied systems, AFM and AFM-IR do not only add spatial resolution, but provide access to chemical-structural information at the hierarchical length scales of small molecules, single polymer chains, supramolecular assemblies, and monolayer organization. AFM and AFM-IR therefore make it possible to interpret organization not only through spatially averaged spectroscopic or morphological descriptors, but through correlated nanoscale structural and chemical information.

Although **Chapter 2** does not include AFM-IR readout, it provides the feature-resolved structural basis on which the later AFM-IR interpretation builds, by showing that surface-supported polymer systems are composed of distinguishable individual features rather than one averaged population.

Chapter 3 shows that AMS AFM-IR distinguishes nanoscale chemical signatures associated with different conformational and assembly states in the studied chiral polymer system. AFM-IR therefore does not only show that chirality is accompanied by structural differences across molecular, single-chain, and supramolecular organization levels, but also makes the corresponding chemical-structural differences experimentally accessible. In this way, AFM-IR allows hierarchical structural organization to be resolved not only as a morphological progression, but also as a chemically distinguishable progression across connected organization levels.[4]

Chapter 4 shows that AFM-IR resolves the emergent carbonyl signature associated with polymer monolayer organization and distinguishes the polymer monolayer from the coverage-invariant monomer monolayer. AFM-IR therefore provides direct nanoscale chemical evidence that different balances between substrate–adsorbate and adsorbate–adsorbate interactions give rise to different monolayer states. AFM-IR thus makes monolayer organization in functional surfaces chemically interpretable at the nanoscale rather than inferable only from average surface descriptors.[5]

AFM-IR therefore does not function in this thesis simply as a higher-resolution version of bulk spectroscopy. AFM provides the structural basis of nanoscale organization, whereas AFM-IR provides the chemical information required to interpret how heterogeneity, hierarchical structural organization, and intermolecular interactions are expressed within that organization. *The main contribution of AFM-IR in this thesis is that nanoscale organization becomes chemically interpretable rather than only structurally observable.*[4,5]

5.6 Significance and outlook

The results presented in this thesis show that the organization of polymers and functional surfaces cannot always be described sufficiently through bulk-average characterization methods alone. Instead, the studied systems

are resolved through heterogeneity, hierarchical structural organization, and intermolecular interactions across different length scales. In that sense, the present work contributes by showing how nanoscale and single-feature-resolved characterization can distinguish organization that is averaged out in bulk readouts, and how AFM-IR can add the chemical information needed to interpret that organization rather than only describe it morphologically.

The broader relevance of this conclusion extends beyond the specific polymer and monolayer systems studied here. In materials science, the results support the view that relevant material behavior may arise from organization distributed across different structural levels rather than from averaged descriptors alone. For new material design and functional surface design, the combination of feature-resolved morphology and nanoscale chemical information provides a more direct way to identify which organization states, assembly pathways, and intermolecular interaction regimes are associated with the resulting material or surface properties.

The conclusions reached here also suggest several directions for further study. For **Chapter 3**, an important next step is to examine how supramolecular chirality can emerge from polymer systems that are not chiral at the molecular level, since recent work has shown chiral emergence from achiral conjugated polymers during hierarchical assembly and broader reviews have highlighted analogous possibilities in achiral polymer systems.[6] For **Chapter 4**, a potential extension would be to test whether the interaction-governed organization identified here also applies to more complex confined or sheet-like assembly systems, including recent examples in which chiral porous sheet assembly is coupled to chirality induction during macrocycle formation.[7] Such directions would extend the present thesis from resolving organization in model systems toward testing how generally nanoscale chemical-structural organization can be used in the design of new materials and functional surfaces.

Overall, the present thesis establishes a nanoscale and single-feature-resolved basis for understanding the organization of polymers and functional surfaces, while also opening clear directions for extending such analysis toward more complex materials, more diverse interfaces, and more predictive structure–organization–property relationships.

5.7 References

(1) Park, K. S.; Xue, Z.; Patel, B. B.; An, H.; Kwok, J. J.; Kafle, P.; Chen, Q.; Shukla, D.; Diao, Y. Chiral emergence in multistep hierarchical assembly of achiral conjugated polymers. *Nat. Commun.* **2022**, *13* (1), 2738. DOI: 10.1038/s41467-022-30420-6.

(2) Zhang, G.; Cheng, X.; Wang, Y.; Zhang, W. Supramolecular chiral polymeric aggregates: Construction and applications. *Aggregate* **2023**, *4* (1), e262. DOI: 10.1002/agt2.262.

(3) Li, M.; Liu, M.; Qi, F.; Lin, F. R.; Jen, A. K. Y. Self-Assembled Monolayers for Interfacial Engineering in Solution-Processed Thin-Film Electronic Devices: Design, Fabrication, and Applications. *Chem. Rev.* **2024**, *124* (5), 2138–2204. DOI: 10.1021/acs.chemrev.3c00396.

(4) Dazzi, A.; Prater, C. B. AFM-IR: Technology and Applications in Nanoscale Infrared Spectroscopy and Chemical Imaging. *Chem. Rev.* **2017**, *117* (7), 5146–5173. DOI: 10.1021/acs.chemrev.6b00448.

(5) V. D. dos Santos, A. C.; Hondl, N.; Ramos-Garcia, V.; Kuligowski, J.; Lendl, B.; Ramer, G. AFM-IR for Nanoscale Chemical Characterization in Life Sciences: Recent Developments and Future Directions. *ACS Measurem. Sci. Au* **2023**, *3* (5), 301–314. DOI: 10.1021/acsmeasuresciau.3c00010.

(6) Groves, C.; Reid, O. G.; Ginger, D. S. Heterogeneity in Polymer Solar Cells: Local Morphology and Performance in Organic Photovoltaics Studied with Scanning Probe Microscopy. *Acc. Chem. Res.* **2010**, *43* (5), 612–620. DOI: 10.1021/ar900231q.

(7) Li, Y.; Zheng, T.; Li, Z.; Kim, Y. Y.; Lee, M. Chiral Porous Sheet Assembly for Multiple Chirality Induction in Macrocycle Formation. *J. Am. Chem. Soc.* **2025**, *147* (34), 31198–31203. DOI: 10.1021/jacs.5c09981.

Summary

Polymers and functional surfaces are often described by bulk-average characterization methods, but these do not fully capture how organization and properties arise across hierarchical length scales. This thesis addresses this limitation through nanoscale chemical and structural characterization of polymers and functional surfaces. By combining atomic force microscopy (AFM) with acoustic-mechanical suppressed photothermal infrared nanospectroscopy (AMS-AFM-IR), this thesis resolves local heterogeneity, hierarchical structural organization, and intermolecular interactions beyond bulk-average readouts.

Chapter 2 establishes an AFM-based methodology for single-feature-resolved molecular-weight estimation of surface-supported polymer features. Individual polymer features are analyzed through their apparent area and height, followed by density-based conversion to molecular weight. The results show that surface-supported polymer systems are composed of discrete features that differ in morphology, molecular weight, and aggregation state, and therefore cannot be treated as equivalent units within one averaged population. AFM-based analysis preserves feature-level molecular-weight distributions beyond bulk-averaged readouts and resolves clustered populations consistent with different aggregate states. Chapter 2 therefore shows that nanoscale variation is an intrinsic feature of the polymer sample rather than a deviation from its average description.

Chapter 3 shows that chirality in chiral and racemic polymer systems emerges across molecular, single-chain, and supramolecular length scales. Bulk Chiral-HPLC, circular dichroism (CD), infrared (IR), and UV-Vis spectroscopy provide average information, but AFM imaging combined with AMS-AFM-IR resolves the nanoscale chemical-structural heterogeneity of these systems directly. Chirality is not expressed as a single uniform average state, but as the sum of locally distinct conformations, assembly states, and nanoscale chemical signatures. Central chirality is present at the molecular level, while polymerization gives rise to backbone chirality in the chiral polymer and supramolecular chirality in the racemic polymer. Chapter 3 therefore demonstrates that chirality can be resolved hierarchically across different levels of organization.

Chapter 4 investigates self-assembled monolayers formed by monomers and polymers on highly ordered pyrolytic graphite (HOPG). AFM and AFM-IR show that the monomer system forms a coverage-invariant monolayer, whereas

the polymer system forms a cooperative monolayer with coverage-dependent structural changes, lateral association, and an emergent carbonyl band at approximately 1725 cm^{-1}. Together with the increase in water contact angle, these results provide direct evidence that the polymer monolayer is governed by adsorbate-adsorbate intermolecular interactions, whereas the monomer monolayer remains dominated by substrate-adsorbate interactions. Chapter 4 therefore shows that local monolayer organization and intermolecular interactions govern the formation of these functional surfaces.

Taken together, this thesis shows that polymers and functional surfaces are best understood beyond bulk-average characterization methods and at the level of local organization. Across single polymer features, supramolecular assemblies, and self-assembled monolayers, local heterogeneity, hierarchical structural organization, and intermolecular interactions are shown to govern how organization and properties arise. Overall, this thesis establishes nanoscale chemical-structural characterization as a direct route to understanding polymers and functional surfaces at the level where their relevant organization and properties are formed.

论文总结

很多高分子材料和功能表面，平时都是用“看平均值”的方法来研究的。比如测平均分子量、平均厚度、平均光谱信号，或者平均表面性质。这些方法当然很重要，因为它们能告诉我们材料整体是什么样。但问题是，很多材料真正决定性能的关键，并不只存在于“平均值”里，而是存在于很小很小的局部区域中。也就是说，材料在微小尺度上可能并不均一，不同位置、不同结构单元之间可能有明显差异，而这些局部差异最后会影响整个材料的性质。

这篇论文研究的核心，就是把观察尺度缩小到纳米尺度，也就是非常小的尺度，去看高分子和功能表面在局部到底是怎样组织起来的，它们的性质又是怎样从这些局部结构中产生出来的。为此，这篇论文主要结合了两类实验方法。一类是原子力显微镜，它可以把表面的形貌看得很清楚，知道表面上有什么结构、这些结构有多高、多宽、长什么样。另一类是原子力显微红外光谱，它不仅能看到形貌，还能在很小的尺度上读出局部的化学信息。在部分研究中，论文还使用了更高灵敏度的声学-机械抑制型原子力显微红外光谱。把“形貌”与“化学信息”放在一起，才能更直接地理解材料真正的组织方式，而不是只停留在平均结果上。

论文第二章研究的是：能不能不用传统的整体平均方法，而是直接对表面上的单个高分子特征进行分析，估算它们各自的分子量。传统上，分子量通常是通过整体测量得到的，比如用凝胶渗透色谱这类方法，得到的是整个样品的平均结果。但这一章的结果表明，表面上的高分子并不是很多“完全一样的单位”，而是由一个个彼此不同的局部特征组成。这些特征在大小、形状、高度、分子量以及聚集状态上都存在差别。也就是说，一个高分子样品在很小尺度上本来就具有差异性，而这种差异不是误差，也不是实验噪音，而是材料本身真实的一部分。

论文第三章研究的是“手性”问题。手性可以简单理解成像左手和右手那样，彼此相似但不能完全重合的区别。很多分子和材料都会表现出这种特性。传统方法，例如手性高效液相色谱、圆二色光谱、红外光谱和紫外-可见吸收光谱，可以告诉我们样品整体上有没有手性差别，但往往看不清这种差别具体是如何在不同层级上表现出来的。这一章发现，手性并不是只存在于单个分子的层面，而是会从分子层面继续发展到单条高分子链，再到更大的聚集结构。通过原子力显微镜和声学-机械抑制型原子力显微红外光谱的结合，可以看到这些体系在纳米尺度上既有结构上的差异，也有化学上的差异。换句话说，手性不是以一种均匀、平均的方式分布在整个材料里，而是通过不同的局部构象、不同的聚集方式以及不同的局部化学特征表现出来。

论文第四章研究的是功能表面中的单分子层，也就是分子或高分子在表面上铺成非常薄的一层。这样的体系常被用来作为功能表面的模型。这里使用的基底是高定向热解石墨。结果发现，小分子和高分子在表面上的组织方式并

不一样。小分子形成的单层比较稳定，在不同覆盖程度下变化不大；而高分子形成的单层则会随着覆盖程度变化，出现更明显的侧向聚集、结构重排，以及新的化学信号。这说明，高分子单层的形成并不只是“有多少分子铺在表面上”这么简单，更重要的是这些高分子彼此之间怎么相互作用、怎么组织起来。也就是说，功能表面的形成和性质，和分子之间的相互作用有非常直接的关系。

综合来看，这篇论文说明了一件很重要的事情：高分子和功能表面的很多关键性质，并不能只靠整体平均测量来真正解释。要理解这些材料，必须进一步看到它们在很小尺度上的局部差异、不同层级上的结构组织，以及分子之间的相互作用。原子力显微镜和原子力显微红外光谱的结合，使我们不仅能看到材料“长什么样”，还能知道它“在化学上有什么不同”。这让我们能够在材料真正形成结构和产生性质的那个层级上去理解它们。也正因为这样，这篇论文的意义不只是多测了一些更细的图，而是提供了一种更直接理解高分子和功能表面的方式。

Acknowledgements

一切的一切, 首先我要感谢我自己, 选择了PhD这条路, 不问自己后不后悔。或许是一条最直接的路, 或许是一条最难走的路, 或许是一条最确定也是最不确定的路。一路上学会了太多, 新的课题, 新的技术, 新的方法论, 对一切新的看法与角度。都说喝茶是小登向中登的转变, 一路上是如何和自己的野望与不甘心和解的。一分一秒累计成四年多, 岁月永远留不住, 是不是学会了和野望和解。是不是还留恋着过往的一切, 想要停留在那个年轻的永远没有烦恼的自己。谁都会不敢直面将来的风险与挑战。感谢自己从来没有后悔, 没有瞻前顾后, 没有万一, 不问如果。

然后要感谢我的父母, 没有给我任何压力, 没有给我任何顾虑, 支持我的一切选择。或许他们物质上不是富有的, 或许他们学理上没有博士与教授的头衔, 但是他们给了我他们可以给予的一切, 不管是物质上的还是精神上的。他们是最棒的父母。你们一直很关注我的工作, 我在电话里也一直讲不清, 我特意写了一个中文的总结, 肯定你们一看就懂。

还要感谢Nano。感谢你在这五年里始终陪伴着我。很多时候, 只要看到你, 皮质醇好像就会在一瞬间清零。你其实没有选择: 离开妈妈, 跟着我来到新的生活里, 而你只是摇着尾巴接受了这一切, 从不追问, 也从不抱怨。你用那双单纯而明亮的大眼睛抚慰着我, 在我疲惫、焦虑、失落的时候, 把我重新带回到当下。有时我甚至觉得, 不是我在养你, 而是你用行动、用灵魂、用你所拥有的一切, 毫无保留地爱着我。谢谢你成为我的 Nano, 成为这段 PhD 旅程里最柔软、最坚定的陪伴。

I would like to thank my supervisor Francesco Simone Ruggeri. We are very different people which I knew from the beginning. But you are like an endless well of wisdom, pouring forth knowledge like vintage wine, deep, refined, and ever flowing. Maybe we didn't say it, or we haven't said it enough, you are a great supervisor and mentor.

I would like to thank my promotors: Han Zuilhof and Jasper van der Gucht. You have very much different expertise as well as characters, but I am deeply thankful for the steadfast support and encouragement for both of you. Your insight and mentorship have played a pivotal role in guiding both my academic journey and personal growth.

Special thanks to my paranymphs: Giacomo Nisini and Yongfang Lu.

Nanoscale Microscopy and Spectroscopy Group, my beloved colleagues, namely Anouk Bosman, Mengsha Hu, Giacomo Nisini, Visakh Pillai, Lutger Rutten, Clementina Vitali, Tianyi Yan. You have been an integral part of my journey. Your camaraderie, insightful discussions, and support have created an inspiring and collaborative environment that I will always cherish. And of course, you guys had most of my blah, I hope you all enjoyed it.

Office 7035, the aquarium office facing north, the place sun never rise, it shines with your presence: Anouk Bosman, Julia Mestres Martinez, Stijn Paulusma, Clementina Vitali, Thijmen van Voorthuizen. Within those quiet walls, laughter echoed, ideas bloomed, and friendships flourished. You turned a shadowed corner into a radiant space of warmth, intellect, and camaraderie.

ORC and PCC "Chinese Gang", named by Chang or maybe Jasper, Chang Chen, Can Hu, Mengsha Hu, Yu Han, Si Huang, Mincong Liu, Qin Li, Yongfang Lu, Xuefeng Shen, Qimeng Wang, Yijie Wang, Zhen Yang, Chuanbao Zheng, Kaiyuan Zhou and Yifei Zhou. Special thanks to Chang Chen and Si Huang, when I just started my PhD, which I call the period crash landing, the accompany you offered is invaluable.

All techinicians and support staffs, namely: Hans Beijleveld, Leonie Breuers, Diane te Brake, Frank Claassen, Judith Firet, Raoul Fix, Remco Fokkink, Sidharam Pujari, Claudia Riemsdijk-Cornelisse, Lotte de Ruiter, Marjolein Stupers-Asselman and Eveline van Dijk. Thank you for all your help and support.

I would also like to thank, especially at my latter half of my PhD, my major mental support: FPCCE gaming group, consisting of Yi Liu (教练), Haomiao Wang (好色仙人), Yijie Wang (小火龙), Lingfeng Wu(梵高), Yuxian Wu(小代), Yitan Zhai (外号暂缺), Ziqi Zhuang (Meiko), Ruihao Zhu (Babybus). In the latter half of my PhD, this group is the most important stress-relief group.

Samuel Visser Bravo, my only student during the whole PhD journey. It is my great pleasure to supervise and work with you.

Qichi Hu, Andrea Cerreta, Igor Arkov, James Kerfoot, Cassandra Phillips, Achim Junginger, Vladimir Korolkov, Miriam Unger and Sergey Lemeshko, from Bruker, Park Systems and Photothermal, I have benefited and learnt a lot from your expertise, without your help, my research won't be so smooth.

BM

I don't know if you believe in "Everyone has their own forest: those who are lost remain lost; those who are meant to meet will meet again." I don't know how long it would take us to forget about each other. I learnt a lot from you and I grew a lot. *Quocumque ieris, sospes sis*.



About the Author



Xuecong Li was born on 12th February 1998, in Wuxi Maternal and Child Health Hospital, Wuxi city, Jiangsu Province, People's Republic of China. He grew up in Wuxi and spent four years in Wu Ai Kindergarten before he went to Wuxi Wu Ai Primary School. He was admitted to Gifted Youth Class in Jiangsu Tianyi High School when he finished his 5th grade and obtained his high school diploma in 2015 from the same high school.

In September 2015, he started his bachelor study in Material Science and Engineering at Beihang University (Beijing University of Aeronautics and Astronautics), Beijing, People's Republic of China. During the program, he did his summer internship at Denmark Technical University with Dr. Martin Nielsen in Copenhagen, Denmark, and his bachelor thesis at University of Montreal with Prof. Dr. Davit Zargarian, in Montreal, Canada. He obtained his BEng degree in 2019.

In September 2019, he started his specialized master program of Chemical and Molecular Science, focusing on Medicinal Chemistry at University of Zurich with Prof. Dr. Felix Zelder, in Zurich, Switzerland. He obtained his master degree in 2021.

In 2021, Xuecong was hired as promovendus to pursue his PhD degree at Wageningen University by Dr. Francesco Simone Ruggeri, Prof. Dr. Han Zuilhof and Prof. Dr. ir Jasper van der Gucht in Laboratory of Organic Chemistry (ORC) and Physical Chemistry and Soft Matter (PCC).

His PhD project focused on nanoscale chemical characterization of polymers and functional surfaces using AFM and AFM-IR, with particular emphasis on local heterogeneity, hierarchical structural organization, and intermolecular interactions. The results of his research are presented in this thesis.

List of Publications

This Thesis:

- Asadi, V., **Li, Xuecong**, Ruggeri, F. S.; Zuilhof, H.; Gucht, J. V.; Kodger. T. E. Synthesis of well-defined linear–bottlebrush–linear triblock copolymer towards architecturally-tunable soft materials. *Polymer Chemistry* **13**, 4666 (2022). DOI: 10.1039/D2PY00841F

- **Li, Xuecong**; Pujari, S. P.; Gucht, J. V.; Zuilhof, H.; Ruggeri, F. S. AFM-Based Estimation of Single Polymer Chains Molecular Weight and Dispersity. *in preparation*

- **Li, Xuecong**; Pujari, S. P.; Gucht, J. V.; Zuilhof, H.; Ruggeri, F. S. Unravelling emergence of chirality in click-chemistry polymers down to the single-chain level. *Nature Communications* **16**, 6761 (2025). DOI: 10.1038/s41467-025-62041-0

- **Li, Xuecong**; Bravo, S. V.; Pujari, S. P.; Gucht, J. V.; Zuilhof, H.; Ruggeri, F. S. Nano-Chemical Analysis of Intermolecular Interactions in Self-assembled Monolayers. under review in *Communications Chemistry*.

Other Work:

- Resnick, S. J.; Qamar, S.; Krishna, P.; Korobeynikov, V.; Ausserwoger, H.; Miller, A.; Esposito, P.; Varela, J. A.; Sheng, J.; Huang, L. H.; Nixon-Abell, J.; Melore, S.; Chung, C.W.; Läubli, N.F.; Kapsiani, S.; **Li, Xuecong** et al. Multiplex neurodegeneration proteotoxicity platform reveals DNAJB6 promotes non-toxic FUS condensate gelation and inhibits neurotoxicity. *Nature Communications* **16**, 10285 (2025). DOI: 10.1038/s41467-025-65178-0.

- Emin, D.; Zhang, Y. P.; Lobanova, E.; Miller, A.; **Li, Xuecong** et al. Small soluble α-synuclein aggregates are the toxic species in Parkinson's disease. *Nature Communications* **13**, 5512 (2022). DOI: 10.1038/s41467-022-33252-6

Overview of Completed Training Activities

Discipline specific activities

Rheology: The Do's and Don'ts & Symposium		2021
NanoScientific Forum Europe		2021
5th Europe Forum on Nanoscale IR Spectroscopy	Poster	2022
Chemometrics		2022
Bruker Benelux AFM User Meeting		2023
Dutch Polymer Days 2023	Plenary Speaker	2023
1st European Meeting on InfraRed Nanospectro Imaging	Oral Presentation	2024
Brightland Polymer Days	Oral Presentation	2024
2nd International Workshop on Near-field Optical Imaging and Spectroscopy	Invited Speaker	2024
Advanced Organic Chemistry		2021-2024

General Courses

Applied Statistics	2022
PhD Competence Assessment	2022
Introduction to R	2023
Mindful Productivity for Scientists	2023
Efficient Writing Strategies	2024
Project and Time Management	2024

Assisting in teaching and supervision activities

ORC-31806 Bio-organic Chemistry at Surfaces	2021
ORC-11806 Analytical Methods in Organic Chemistry	2022
ORC-12803 Organic Chemistry I	2022
ORC-31806 Bio-organic Chemistry at Surfaces	2022
ORC-11806 Analytical Methods in Organic Chemistry	2023
ORC-12803 Organic Chemistry I	2023
ORC-31806 Bio-organic Chemistry at Surfaces	2024
ORC-11806 Analytical Methods in Organic Chemistry	2024
ORC-12803 Organic Chemistry I	2024
Supervision of BSc Student Samuel Visser Bravo	2024
ORC-31806 Bio-organic Chemistry at Surfaces	2025

Other Activities

Preparation of research proposal	2021
PhD study tour	2023
Organising ORC PhD Trip 2023	2023
Weekly Seminar meeting ORC/PCC	2021-2025

Authorship Statement

Chapter 1 General introduction. I wrote the original draft. Promotor Prof. dr. Han Zuilhof (HZ), Prof. dr. ir. Jasper van der Gucht (JVG) and co-promotor Francesco Simone Ruggeri (FSR) commented on the draft. I revised the draft once according to the comments.

Chapter 2 I and FSR. conceived the project. I performed the AFM experiments and analyzed the relative data. Sidharam Pujari (SP) synthetised and characterized the polymers, and analyzed the relative data. I and FSR wrote the original draft of the manuscript. All the authors revised and commented the manuscript. I have used ChatGPT to enhance the clarity of text.

Chapter 3 I and FSR conceived the project. I performed the CD, IR, AFM experiments and analyzed the relative data. I and FSR performed the AFM-IR experiments and analyzed the relative data. SP synthetised and characterized the molecules and the polymers, and analyzed the relative data. The scientific manuscript of this chapter, in which I am listed as the first author, has been published as *Nat. Commun.* 16, 6761 (2025). I and FSR wrote the original draft of the manuscript. All the authors revised and commented the manuscript.

Chapter 4 I and FSR conceived the project. I and my student Samuel Visser Bravo (SVB) performed the IR, AFM experiments and analyzed the resulting data. I performed the AFM-IR and contact angle experiments and analyzed the resulting data. SP synthetized and characterized the monomers and polymers and analyzed the resulting data. The scientific manuscript of this chapter, in which I am listed as the first author, has been submitted and is under review in *Commun. Chem.* I and FSR wrote the original draft of the manuscript. All the authors revised and commented on the manuscript.

Chapter 5 General Discussion and Perspective. I proposed the outline of this chapter and wrote the original draft. I revised the text once according to comments of FSR, HZ and JVG. I have used ChatGPT to enhance the clarity of text.

Summary. I wrote the original draft in English. I revised it once according to comments of FSR, HZ and JVG. I translated the text into a Chinese version.

The research described in this thesis was financially supported by the Dutch Sector Plan (Sectorplan Natuur- en Techniekgebieden) in the Laboratories of Organic Chemistry and Physical Chemistry and Soft Matter, at Wageningen University.

Financial support from Wageningen University for printing this thesis is gratefully acknowledged.

Cover design: Xuecong Li

Printed by ProefschriftMaken || www.proefschriftmaken.nl

